


Ref. Ares(2026)2156290 - 26/02/2026

| Project information | |
|---|---|
| Full title: | **REmanufacturing, repurposing and recycling energy goods through advanced Mechatronic and Digital technologies** |
| Acronym: | R3-Mydas |
| Grant Agreement number: | 101138738 (HORIZON-CL4-2023-TWIN-TRANSITION-01-04 – Innovation Action) |

**Deliverable**

# D2.2 – Digital-based development for remanufacturing of Oil&Gas crankshaft components

| | |
|---|---|
| Dissemination level: | PU - Public, fully open |
| Type of deliverable: | R - Document, report |
| Contractual date of delivery: | 31 October 2025 |
| Deliverable leader: | NCI |
| Status - version, date: | Final – v1.0, 2026-02-26 |
| Keywords: | Remanufactured crankshaft, laser cladding, processing conditions |

Funded by the European Union

*This document is part of a project that is funded by the European Union. Views and opinions expressed are however those of the author(s) only and do not necessarily reflect those of the European Union or the European Health and Digital Executive Agency. Neither the European Union nor the granting authority can be held responsible for them.*
*The document is the property of the R3-Mydas project and should not be distributed or reproduced without prior approval.*
*Find us at [www.r3-mydas.eu](http://www.r3-mydas.eu).*

# Executive Summary

This executive summary provides a comprehensive overview of the deliverable focused on the automated remanufacturing of crankshafts through laser cladding, covering the technical milestones achieved in Tasks 2.1 and 2.2. The primary objective of this work is to define an integrated methodology that minimizes material waste and process defects while ensuring high-quality surface integrity for repaired components.

**Digital protocol and CAD generation**

The first phase of the workflow, detailed under the Digital Protocol, addresses the challenge of discontinued or legacy components where original CAD data is unavailable. Using a 3D snapshot camera, the projects successfully automated the generation of point clouds to digitalize the crankshaft geometry. This data served as the foundation for CAD Model Generation, which is essential for defining the precise repair volumes.

Following digitalization, the project implemented an offline programming strategy within a virtual robotic cell. This approach allows for the definitions and validations of robot trajectories (path-planning) before physical execution, significantly reducing setup times and preventing potential collisions during the cladding process.

**Process optimization and DOE**

The core of the research focused on process optimization through a structured Design of Experiments (DOE). This systematic approach enabled the identification of critical relationships between laser process parameters and various response variables, such as bead geometry and dilution. The DOE was executed successfully, allowing the team to establish a robust operational window. Notably, the analysis revealed specific anomalies in the initial hypothesis, providing deeper insights into the complex interactions of the laser-material system when applied to large-scale industrial parts.

**Simulation and thermal analysis**

A significant portion of the deliverable is dedicated to Simulation Analysis. Thermomechanical simulations were conducted to evaluate the impact of different deposition strategies on the component´s distortion and thermal history. The findings indicate that different scanning patterns do not have a transcendent impact on residual stresses or final deformations. This phenomenon is explained by the massive scale of the crankshaft, which effectively functions as a heat sink, absorbing and dissipating thermal energy so efficiently that local scanning variations become secondary to the overall thermal mass.

Furthermore, the integration of thermal analysis with experimental DOE data has proven to be a valuable tool for the qualitative prediction of the hardness and the integrity in the Heated Affected Zone (HAZ). The results open new possibilities for future research regarding real-time process monitoring and metallurgical control.

**Material substitution and Sustainability**

Finally, the deliverable addresses a material substitution analysis. In line with European manufacturing goals, the project explored replacing traditional cladding materials with more efficient and environmentally friendly alternatives. The results confirm that using materials with a lower environmental impact is technically feasible for this application, maintaining required performance standards while enhancing the sustainability of the remanufacturing cycle.

In conclusion, the methodology, presented bridges the gap between digital path-planning and physical metallurgical optimizations, providing a scalable solution for the high-value repair of heavy industrial components.

| | |
|---|---|
| **Deliverable leader:** | Marcos Díez García (AIMEN), Mónica Salgueiro González (AIMEN), David Castro Boga (AIMEN) |
| **Contributors:** | Diego Cabañas (ZIKNES) |
| **Reviewers:** | Jari Toikkanen (FLE-FI), Chrysa Alexia (ITML) |
| **Approved by:** | Athanasios Poulakidas, Irene Diamantopoulou (NCI) |

| **Document History** | | | |
|---|---|---|---|
| **Version** | **Date** | **Contributor(s)** | **Description** |
| 0.1 | 2026-02-26 | AIMEN, TMCOMAS, ZIKNES | 1st draft for review |
| 0.2 | 2026-02-13 | FLE-FI, ITML | Review |
| 0.3 | 2026-02-18 | AIMEN, TMCOMAS, ZIKNES | Pre-final version |
| 1.0 | 2026-02-26 | NCI | Version to be submitted after final QA |
| | | | |
| | | | |

# Table of Contents

Executive Summary ..... 2
Table of Contents ..... 5
Table of Figures ..... 6
List of Tables ..... 8
Definitions, Acronyms and Abbreviations ..... 10
1 Introduction ..... 11
1.1 Project Information ..... 11
1.2 Document Scope ..... 12
1.3 Document Structure ..... 12
2 Digital Protocol ..... 14
2.1 CAD Model Generation ..... 14
2.1.1 3D Scanner Evaluation and Selection ..... 15
2.1.2 Extrinsic Calibration, Robot Integration and Scanning routine ..... 18
2.1.3 Acquisition and Alignment of Point Clouds ..... 21
2.1.4 Mesh Generation and Surface Reconstruction ..... 24
2.2 Path-planning ..... 28
2.2.1 Cell virtualization ..... 28
2.2.2 Virtualization of the AIMEN Robotic Cell ..... 28
2.2.3 Software for Path-planning ..... 29
2.2.4 Step 1 – Parametric Abstraction of the Crankshaft and Scanning Path Generation ..... 30
2.2.5 Step 2 – Scan-Based Geometry Analysis and Repair Path-Planning ..... 32
2.2.6 Software Overview ..... 35
2.2.7 Mock-up trials ..... 37
3 Process Optimization ..... 40
3.1 Design of Experiments ..... 41
3.1.1 Dilution ..... 42
3.1.2 Width ..... 44
3.1.3 Height ..... 46
3.1.4 Ratio Width/Height ..... 48
3.1.5 Bead Hardness ..... 49

3.1.6 HAZ Hardness ..... 52
3.2 Simulation analysis ..... 56
3.3 Manufacturability tests ..... 73
3.4 Material substitution analysis ..... 79
3.4.1 Wear properties ..... 80
3.4.2 Mock-up tests with Ferro 55 ..... 86
4 Conclusions ..... 89
4.1 Relevance to Made in Europe ..... 89
4.2 Concluding Remarks ..... 90
5 References ..... 92

# Table of Figures

Figure 1: Scanner selection trials. ..... 16
Figure 2: Both CADs, HandyScan has holes in the marker's positions. ..... 16
Figure 3: Comparing both CAD. ..... 17
Figure 4: Symmetry problem. ..... 18
Figure 5: Physical reference part on the robot table. ..... 19
Figure 6: Calibrating routine process. ..... 20
Figure 7: Crankshaft scanning routine. ..... 21
Figure 8: PointCloud unaligned. ..... 22
Figure 9: (Left) Frame-to-frame ICP aligned PointCloud. (Right) Frame-to-model aligned PointCloud. ..... 23
Figure 10: PointCloud aligned. ..... 24
Figure 11: Poisson surface reconstruction. ..... 25
Figure 12: Greedy triangulation. ..... 25
Figure 13: Ball pivoting reconstruction. ..... 26
Figure 14: Implicit triangulation. ..... 26
Figure 15: Final mesh without postprocessing and with processing. ..... 27
Figure 16: Virtualized AIMEN robotic cell shown in a scanning configuration, including KUKA robotic arm and turntable. The same cell supports alternative end-effector configurations for repair operations. ..... 29
Figure 17: Parameters defining the simplified parametric crankshaft model, including journal radio, crankpin radio, axial length and eccentricity. ..... 31
Figure 18: Example of simplified, parametric crankshaft geometry generated automatically by the path-planning software. ..... 32
Figure 19: Identification of functional working surfaces on the scanned crankshaft geometry requiring material deposition. ..... 33

Figure 20: (Left)Spiral laser-cladding toolpath with interruptions and circular border paths around detected holes. (Right) Laser-cladding toolpath simulation with AIMEN's robot cell..... 34
Figure 21: Beam shape distribution. (Left) Gauss distribution- intensity 1.98 kw/cm2. (Right) Top-Hat - Intensity 12.53 kw/cm2. ..... 41
Figure 22: Pareto chart for Dilution area. ..... 43
Figure 23: Main effects on Dilution area. ..... 43
Figure 24: Interaction plot for Dilution area. ..... 44
Figure 25: Pareto chart for Width. ..... 45
Figure 26: Main effects for Track Width. ..... 45
Figure 27: Contour plots for track width. ..... 46
Figure 28: Pareto chart for Height. ..... 47
Figure 29: Main effects plot for Track Height. ..... 47
Figure 30: Interaction plot for Track Height. ..... 48
Figure 31: Pareto chart for Ratio Width/Height. ..... 49
Figure 32: Main effects plot for Ratio Width/Height. ..... 49
Figure 33: Pareto chart for Bead Hardness. ..... 50
Figure 34: Main effects for Bead Hardness. ..... 50
Figure 35: Interaction plot for Bead Hardness. ..... 51
Figure 36: Box diagram of Bead Hardness for various power and powder flow. ..... 51
Figure 37: Hardness footprint for (Left) 20 g/min (Right) 10 g/min. Fixed parameters: Power 3500W, Speed 15 mm/s. ..... 52
Figure 38: Micrography's at 100x of (Left) 20 g/min (Right) 10 g/min. ..... 52
Figure 39: Pareto chart of HAZ Hardness. ..... 53
Figure 40: Main effects on HAZ Hardness. ..... 53
Figure 41: Interaction plot for HAZ Hardness and powder flow. ..... 54
Figure 42: Box plot for HAZ Hardness. ..... 54
Figure 43: (Left) Hardness footprint HV1. Indentation 1 to 3 from left to right. (Right) macrography of single track. ..... 55
Figure 44: Pareto chart for HAZ Hardness without preheating. ..... 56
Figure 45: Simplified representation of thermal stress and strains formation during heating and cooling. ..... 57
Figure 46: Scanning paths (Left) Raster, (Center) Alternate raster, (Right) Concentric. 59
Figure 47: FEM model with uniform mesh on layers and nonuniform mesh on the substrate. ..... 61
Figure 48: Temperature evolution from different simulation iteration against experimental register plot. ..... 62
Figure 49: Temperature evolution from simulation versus experimental register plot and total distortion field. ..... 62
Figure 50: (Top) Different strategies. (Bottom) Path planning distortion effects. ..... 63
Figure 51: Path planning distortion effects. ..... 64

Figure 52: Path planning distortion effects. ..... 64
Figure 53: Large crankshaft mock-up works as a significant heat sink. ..... 66
Figure 54:Thermal evolution using different path planning. ..... 67
Figure 55:Thermal evolution using different path planning..... 68
Figure 56: Experimental Set up..... 70
Figure 57: Tracks hardness. ..... 70
Figure 58: HAZ Simulation vs experimental. ..... 71
Figure 59: Macrographic vs simulation HAZ. ..... 71
Figure 60: Cooling rates extracted from macro approach simulation. ..... 72
Figure 61: Detailed drawing of the Mock-up geometry. ..... 74
Figure 62: Macrograpy´s for A1 condition. Start from right to left. ..... 75
Figure 63: Macrography for A2 condition. Start from right to left. ..... 75
Figure 64: Macrography´s for B1 condition. Start from top left. ..... 76
Figure 65: Macrography´s B2 condition. Start from right to left. ..... 77
Figure 66: Mock-up with the reference scheme indicating the position of each drill hole and the fillet allocation. ..... 77
Figure 67: Macrography´s of cylinders cross section. (Top) Left to right A, B and C. (Bottom) Left to right D, E and F. ..... 78
Figure 68: Initial fillet macrography´s. (Left) Condition 2. (Right) Condition 1. ..... 79
Figure 69: Final fillet macrography´s (Left) Condition 2 (Right) Condition 1. ..... 79
Figure 70: Milipoints plot for repairing process sing Stellite 21 (As is repair ST) and Ferro55 (As is repair CS). ..... 80
Figure 71: Low load conditions (Top Left) Wear surface analysis test for Stellite 21 and (Top Right) Friction coefficient versus distance plot. (Bottom Left) Wear surface analysis test for Ferro55 and Bottom Right) Friction coefficient versus distance plot..... 81
Figure 72: High load conditions (Top Left) Wear surface analysis test for Stellite 21 and (Top Right) Friction coefficient versus distance plot. (Bottom Left) Wear surface analysis test for Ferro55 and (Bottom Right) Friction coefficient versus distance plot..... 82
Figure 73: SEM micrography´s Ferro55- 5N(Left)100x (Right) 1000x. ..... 83
Figure 74: SEM micrography´s Ferro55- 30N(Left)100x (Right) 1000x. ..... 84
Figure 75: SEM micrography´s Stellite 21- 5N(Left)100x (Right) 1000x..... 85
Figure 76: Stellite 21 (30N) 100x. ..... 86
Figure 77: Image of the Mock-up 2 cladded with Ferro 55 (Left) Sequence 1. (Right) Sequence 2. ..... 86
Figure 78: Sequence 1 macrographs (A2, C2 and A1 from left to right). ..... 87
Figure 79: Sequence 2 macrographs (A4, C5 and A3 from left to right). ..... 88

# List of Tables

Table 1: The R3-Mydas consortium..... 11
Table 2: Composition of the baseplate material used for the UC..... 40

Table 3: Laser cell main components. 40
Table 4: List of factors, levels and outcomes studied in the DoE. 41
Table 5: Model summary for dilution. 42
Table 6: Model summary for Width. 44
Table 7: Model summary for Height. 46
Table 8: Model summary for Ratio Width/Height. 48
Table 9: F- Values for different factors and outcomes. 48
Table 10: Model summary for Bead hardness. 49
Table 11: Model summary for HAZ hardness. 52
Table 12: Hardness measurements in HAZ. 54
Table 13: Model summary of HAZ Hardness without preheating factor. 55
Table 14: Process parameters for thermal material study. 69
Table 15: Process parameters tested on different mock-up´s, tiling angle 20°. 74
Table 16: Process parameters for holes. 77
Table 17: Tilting angle conditions. 78
Table 18: Hardness value HV10 for Stellite 21 and Ferro 55. 80
Table 19: Boundary conditions for pin on disk tests (Low load condition). 80
Table 20: Pin-on-disk results for Stellite 21 and Ferro 55. 83
Table 21: EDS analysis for high magnificence image. Atom/Mol%. 84
Table 22: EDS analysis for high magnificence image. Atom/Mol%. 85
Table 23: Process parameters for Mock-up 2. 87
Table 24. Hardness measurements. 88
Table 25: Contributions towards specific objectives of Made in Europe. 89
Table 26: Contributions towards key technologies and enablers of Made in Europe. 89

# Definitions, Acronyms and Abbreviations

| Acronym/ Abbreviation | Title |
|---|---|
| **BPA** | Ball Pivoting Algorithm |
| **CAD** | Computer-Aided Design |
| **DOE** | Design of Experiments |
| **HAZ** | Heated Affected Zone |
| **ICP** | Iterative Closest Point |
| **MAG** | Metal Active Gas |
| **MIG** | Metal Inert Gas |
| **MLS** | Moving Least Squares |
| **TCP** | Tool Center Point |
| **UC** | Use Case |

| Term | Definition |
|---|---|
| | |
| | |

# 1 Introduction

## 1.1 Project Information

Despite the multiple advantages of products remanufacturing, being widely recognised as an effective means for transitioning to a more circular economy, there is still need for improved research and experimental observations, to improve traceability and reliability of the final products from end-users' perspectives, as well as enhanced impacts monitoring. The primary R3-Mydas objective is to develop a multi-actor framework, integrating innovative digital technologies (ML for process and quality control, marketplace, graph models for defects detection, digital twins), advanced mechatronics (AM, laser-cladding, automated disassembly/reassembly) and newly developed approaches from SSH (extended TAM/UTAUT models, ethics and legal framework), for functionally, environmentally and economically sustainable circular value chains for remanufacturing of energy goods at the factory level (Oil&Gas crankshafts – demo 1, E-vehicles batteries – demo 2, Wind turbines gearboxes – demo 3).

R3-Mydas will deliver unprecedented impacts throughout the targeted value chains, as follows: up to 60% time reduction in programming for remanufacturing; up to 20% increased product quality; up to 30% rework reduction [Demo 1]; up to 30% improved detection of tiny deviations from normal behaviour; up to 50% faster anomaly localization; up to 30% increase the number of different modality data streams handled; up to 20% faster fusion process [Demo 2]; up to 99% reusage rate; -90% prevention rate; -75% lead time; up to 85% raw material savings potential [Demo 3]. R3-Mydas will deliver a marketplace associating to each remanufactured product or services/component for remanufacturing a Digital Passport-like set of information, ensuring full traceability. Finally, a dedicated training programme will be designed and delivered by EITM, targeting the P R3-Mydas project remanufacturing value chains (100+ training hours and 100+ diverse stakeholders engaged during the Project).

*Table 1: The R3-Mydas consortium.*

| Number[1] | Name | Country | Short name |
|---|---|---|---|
| 1(CO) | NETCOMPANY-INTRASOFT SA | Luxemburg | NCI |
| 2 | EUROPEAN FEDERATION FOR WELDING JOINING AND CUTTING | Belgium | EWF |
| 3 | EIT MANUFACTURING SOUTH SRL | Italy | EITM |
| 4 | FLENDER FINLAND OY | Finland | FLE-FI |
| 4.1(AE) | FLENDER GMBH | Germany | FLE |
| 5 | AVL LIST GMBH | Austria | AVL |

[1] CO: Coordinator. AE: Affiliated Entity. AP: Associated Partner.

| Number[1] | Name | Country | Short name |
|---|---|---|---|
| 6 | TALLERES MECANICOS COMAS SLU | Spain | TMCOMAS |
| 7 | SPIN ROBOTICS IVS | Denmark | SPIN |
| 8 | ASOCIATION DE INVESTIGACION METALURGICA DEL NOROESTE | Spain | AIMEN |
| 9 | LAPPEENRANNAN-LAHDEN TEKNILLINEN YLIOPISTO LUT | Finland | LUT |
| 10 | INFORMATION TECHNOLOGY FOR MARKET LEADERSHIP | Greece | ITML |
| 11 | DEEP BLUE SRL | Italy | DBL |
| 12 | CHAROKOPEIO PANEPISTIMIO | Greece | HUA |
| 13 | IKERLAN S. COOP | Spain | Ikerlan |
| 14 | ZIKNES TECHNOLOGY SL | Spain | Ziknes |
| 15 (AP) | CSEM CENTRE SUISSE D'ELECTRONIQUE ET DE MICROTECHNIQUE SA - RECHERCHE ET DEVELOPPEMENT | Switzerland | CSEM |

## 1.2 Document Scope

The scope of this document is to describe the methodology required to define and implement an adequate path-planning strategy for remanufacturing of crankshaft using laser cladding. The document covers the full workflow starting from component positioning and digitalization, through CAD model generation, up to definition and validation of robot trajectory planning.

In addition, this deliverable provides a detailed description of the processing conditions applied during the laser cladding remanufacturing process, with the objective of minimizing material waste, reducing process-induced defects, and ensuring adequate surface quality and material properties of the repaired crankshaft components.

The content of this document is focused on the results obtained within Task 2.1 and 2.2, addressing both the digital protocol for process automation and the optimization of the laser cladding parameters. Issues related to downstream machining operations, final component certification, or in-service validation are considered outside the scope of this deliverable.

## 1.3 Document Structure

This document is comprised of the following chapters:

**Chapter 1** presents an introduction to the project and the document.

**Chapter 2** presents the results obtained within the Task 2.1, which is focused on the digitalization and automation of the crankshaft repair process. It describes the

development and implementation of the digital workflow, including CAD model generation and path-planning strategies, aimed at enabling a more efficient repeatable, and automated laser cladding-based repair process.

**Chapter 3** reports the results associated with Task 2.2, addressing the optimization of the laser cladding process. The work presented focuses on reducing process-induced defects and enhancing material properties through design of experiments, simulation analysis, manufacturability tests, and material substitution studies.

**Chapter 4** summarizes the main findings of the document and presents the overall conclusions derived from the digital protocol development and the laser cladding process optimization activities.

# 2 Digital Protocol

## 2.1 CAD Model Generation

Cad Model Generation was developed in Subtask 2.1.1 and it is part of the work package focused on the digitization and automation of industrial processes within the framework of the R3-MYDAS project. Its main objective has been the development of an automated three-dimensional data acquisition system, capable of generating point clouds and CAD models with the necessary accuracy and consistency to be integrated into advanced processes such as robotic material deposition.

In the initial state of the project, material deposition routines were manually programmed as shown in D2.1, which represented a slow, inflexible process highly dependent on the operator's experience. This approach presented difficulties especially in cases with variable geometries or short runs, where manual programming became inefficient and difficult to maintain. In addition, the absence of scanned geometric data prevented automatic adjustments or adjustments based on actual measurements, limiting the possibilities for optimization and digital validation.

Subtask 2.1.1 was proposed as a comprehensive solution to this problem, developing a tool chain capable of scanning a part in a fully automated way using an industrial robot, registering the different captures in a common coordinate system and generating a dense and coherent three-dimensional model. This model can then be used in later stages of the workflow, such as automated planning of laser cladding head deposition or inspection routes.

The work has been led and executed by AIMEN Technology Centre, and has been structured into four main activities:

1. Selection of the most suitable 3D scanner for use in automation environments, considering factors such as accuracy, capture speed, integration with robots and georeferencing capability.
2. Extrinsic calibration of the system, by means of which the spatial transformation between the scanner and the robot base was established. This process allows automatic georeferencing of the 3D captures in the global coordinate system.
3. Acquisition of multiple captures from different positions of the robot, with subsequent alignment and merging of the point clouds into a single coherent model.
4. Generation of a surface mesh from the merged point cloud, using different reconstruction algorithms and post-processing techniques to obtain a clean, optimized model suitable for CAD environments.

The subtask was developed in a sequential and modular way, allowing each stage independently before integrating it in.

This section presents in detail each of the activities developed in this subtask, including the technical decisions taken, the tests performed, the tools used, and the results obtained, with the aim of documenting the complete development of the solution.

## 2.1.13D Scanner Evaluation and Selection

One of the first key steps in the development of the 3D acquisition system was the selection of the most suitable scanner to operate in a robotic environment. This decision was fundamental, as the device had to not only offer high capture quality, but also be compatible with automated workflows, integrate easily with the robotic system and allow direct georeferencing of the acquired data.

During this stage, two different commercial technologies were analysed: on the one hand, the Photoneo Structured Light Scanner (Photoneo, 2025), based on structured light projection, and on the other hand, the Creaform HandySCAN (Handyscan, 2025), a handheld portable laser scanner also available at TMCOMAS facilities. Both devices were evaluated through functional tests, assessing aspects such as accuracy, resolution, capture stability, ease of integration, and technology dependence.

The Photoneo scanner employs the structured light technique, which consists of projecting light patterns onto the surface of the object. The system's cameras capture the deformation of these patterns and reconstruct the three-dimensional geometry of the scanned object. This device is specifically designed for automated environments: it allows triggers synchronized with the robot's movement, provides real-time georeferenced data with respect to the robot's coordinate system, and is compatible with standard protocols such as GigE Vision. This compatibility allows the scanner to be replaced by other third-party models that comply with the same protocol, facilitating the scalability, flexibility and technological independence of the developed system.

In contrast, the Creaform HandySCAN uses a different approach: it projects multiple laser lines on the object while the operator manually or the robot moves the scanner around the part. Through markers placed on the object or in the environment, the system reconstructs the 3D shape. This approach is suitable for high-precision applications and is especially useful on highly symmetrical objects, where other technologies have difficulty recording orientation between captures. However, its integration into an automated flow presents multiple limitations. Although it can technically be mounted on a robot, it does not use standard communication protocols, and its operation relies exclusively on proprietary software. It does not allow trigger control or direct access to the data captured per frame.

In addition, georeferencing with the HandySCAN is not automatic. To align the 3D data with the robot's coordinate system, it is necessary to first precisely locate the position of the reference markers with respect to the robot, and then manually apply a geometric transformation to the obtained CAD. This process is error-prone, difficult to scale and totally incompatible with automatic and replicable flows.

To experimentally evaluate the accuracy of both systems, the same crankshaft (real part supplied by TMCOMAS) was scanned using both devices (Figure 1). The results were then aligned using a manual geometric adjustment, and the difference between the two resulting point clouds was analysed. The average difference observed was less than 1 mm, confirming that both scanners generate consistent results within acceptable margins for the target application. It should be noted that part of this discrepancy can be attributed to the error introduced during the alignment process, which was performed manually.




*Figure 1: Scanner selection trials.*

In particular, the most significant errors were observed on the vertical axis, as can be seen in the comparison image. This deviation is mainly due to small differences in the vertical alignment between the two captures, which is to be expected considering that no automated precision adjustment was applied.

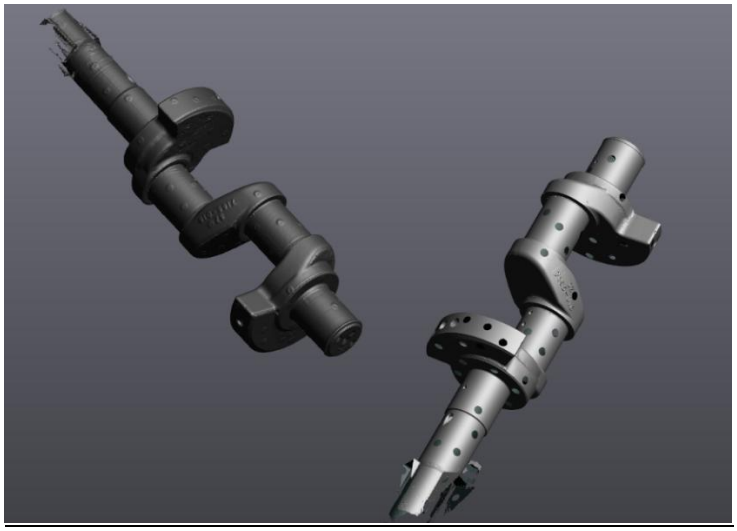


*Figure 2: Both CADs, HandyScan has holes in the marker's positions.*

Another relevant aspect is the difference in the treatment of the markers between the two systems. HandySCAN requires the use of adhesive markers distributed on the part or the environment to record their relative position during scanning. These markers are automatically removed during the reconstruction of the model, as they are part of the reference system and not part of the actual geometry of the object. In contrast, the Photoneo system does not require markers for its operation, and therefore captures everything in its field of view, including markers if present (Figure 2). This difference can generate small local discrepancies in the areas near the markers and helps to explain part of the errors observed during the comparison (Figure 3).

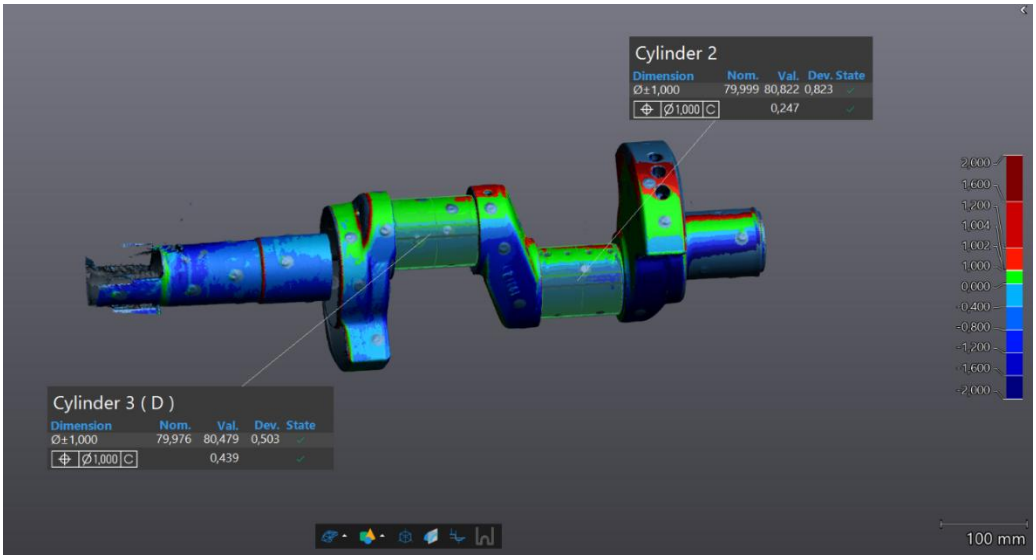



*Figure 3: Comparing both CAD.*

Despite these considerations, the overall agreement between the two scans was high, supporting the reliability of the selected automated system, and its suitability for accurate digitizing of complex industrial geometries. Based on all these aspects, the Photoneo Structured Light Scanner was selected as the main solution for the automated 3D acquisition system. Its direct integration with robotic environments, compatibility with open protocols and the ability to generate georeferenced data without manual intervention make it the optimal tool to achieve the objectives of this task. The HandySCAN is reserved as a support resource for occasional digitisations in manual mode or on difficult geometries for structured scanning, like symmetries (Figure 4).



*Figure 4: Symmetry problem.*

### 2.1.2 Extrinsic Calibration, Robot Integration and Scanning routine

Once the appropriate scanner was selected, the next fundamental step was to integrate the 3D acquisition system with the industrial robot, ensuring that all data captures were correctly referenced in the workspace. This process was approached on two main fronts: on the one hand, the extrinsic calibration between the scanner and the robot coordinate system, and on the other hand, the integration of real-time communication between both elements to enable an automated workflow.

#### Extrinsic calibration of the system

The objective of this phase was to determine the spatial transformation between the scanner and the robot coordinate system. Since the scanner is fixedly mounted relative to the robot, it is necessary to know precisely that geometric relationship in order to automatically georeferenced each captured point cloud in the overall cell system. This transformation (normally represented by a rotation matrix and a translation vector) allows all data captures to be automatically georeferenced in the robot's global system.

To guarantee the physical repeatability of the system and avoid frequent recalibrations, a specific mechanical tooling was designed and manufactured to fix the scanner in a constant and stable position. This ensures that the transformation between the scanner and the robot does not vary over time or between work sessions.

For this procedure, a physical reference part (3D AIMEN logo) whose nominal CAD geometry is known with high accuracy was used. This part was placed on the robot worktable (Figure 5) and scanned from different positions of the robot, obtaining several partial views from different angles.



*Figure 5: Physical reference part on the robot table.*

The process followed was as follows:

1. Capture multiple 3D views**:** Different robot positions were programmed from which the scanner captures the part. Each view produces a partial point cloud of the same geometry, but in the scanner's coordinate system.
2. Transformation based on known poses: For each capture, the robot pose (position and orientation of the TCP) is known. If the scanner is calibrated, all captures should match directly in the robot's global system.
3. Registration with nominal CAD model: The scanned point clouds are aligned with the known CAD model of the part, using rigid registration algorithms (e.g. ICP - Iterative Closest Point). This allows estimating the transformation to be applied to the clouds to match the virtual part.
4. Estimation of the extrinsic transformation (Park, 1994): From these correspondences between scanned points and the CAD model and knowing the position of the robot in each capture, the inverse problem of determining the position of the scanner with respect to the robot (hand-eye calibration) can be solved. This procedure can be interpreted as a resolution of the system AX = XB, where A represents the transformations of the robot, B the relative transformations between views, and X the unknown: the extrinsic transformation between the scanner and the robot.

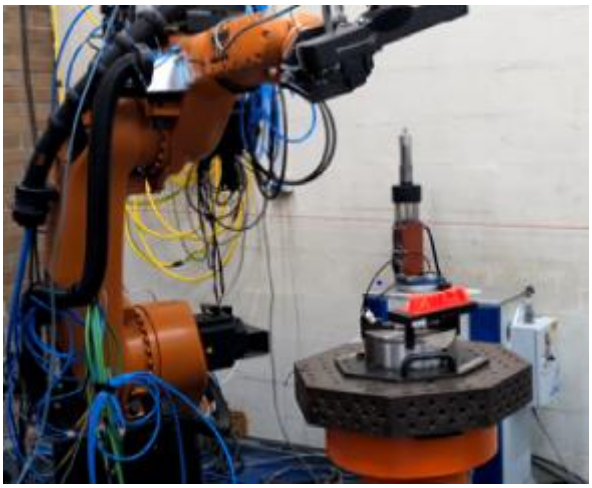


*Figure 6: Calibrating routine process.*

### Integration with robot communication

In parallel, a software module was developed to manage real-time communication with the industrial robots used in the project, specifically ABB and KUKA. This integration makes it possible to fully synchronize the robot's movement with 3D data capture. In both cases, a specific software module was developed capable of interacting with the robot controller to read the current TCP pose (position and orientation of the robot end at each instant) and manage the triggering of the scanner based on synchronized events.

Communication with the robot was done through standard channels in this case, via TCP/IP sockets. The implemented system allows to launch the scanning in an automated way from the controller itself or from a centralized control station, without operator intervention.

### Automatic generation of scan paths

To facilitate the adaptability of the system to different components, a parametric script was developed to generate scan paths based on the geometrical characteristics of the object. The script considers parameters such as diameter, overall length and number of counterweights, and based on them automatically defines the robot positions and scan angles required to obtain complete coverage of the component.

This script was implemented in the RoboDK (Robodk, 2025) simulation and programming environment, which allows not only to generate the trajectories automatically, but also to pre-validate them in a virtual environment before their actual execution (Figure 7). From RoboDK, the trajectories are exported in the format corresponding to the controller.

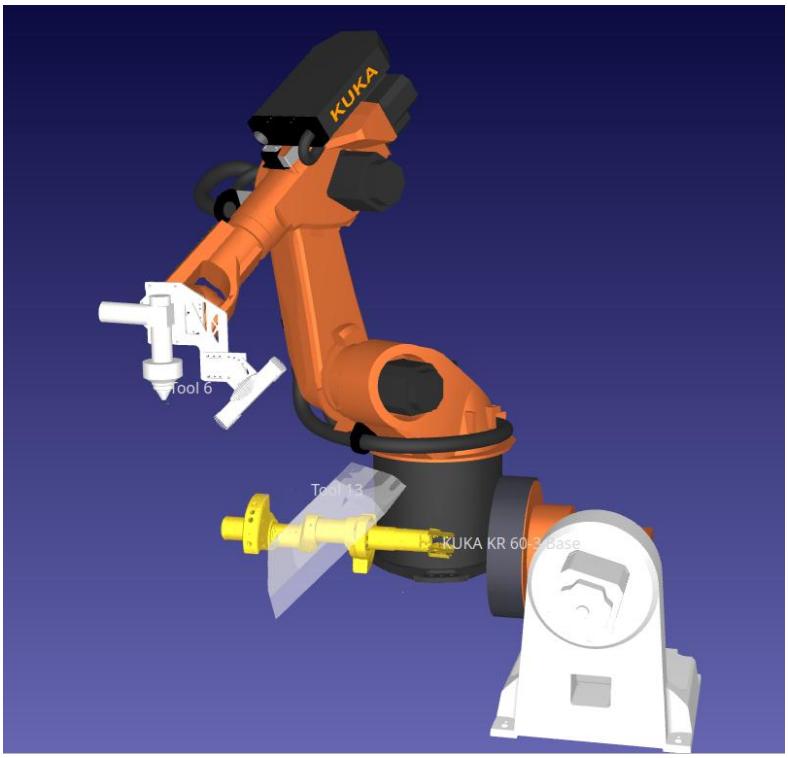



*Figure 7: Crankshaft scanning routine.*

## 2.1.3 Acquisition and Alignment of Point Clouds

Once the execution of scanning trajectories was automated and the communication between the robot and the scanner was established, the system was ready to perform the 3D data acquisition in a fully automatic way. This stage aims to obtain multiple partial captures of the part from different viewpoints and combine them into a single coherent and accurate point cloud, ready for further processing.

### Synchronized multi-view capture

During the scanning process, the robot automatically moves to the positions generated by the script in RoboDK, while the scanner performs a capture in each of them. Thanks to the previously obtained extrinsic calibration and the real-time reading of the robot pose, each generated point cloud is approximately located in the robot coordinate system. This allows a first data fusion to be performed with a reduced error, without the need for absolute alignment from scratch.

However, due to mechanical tolerances, residual errors in calibration and small deviations in the robot's accuracy, **this initial alignment is not sufficient to guarantee a millimetric match between all views** (Figure 8). For this reason, an additional point cloud registration or matching phase was included to refine the relative position between captures and obtain a unified global 3D model.

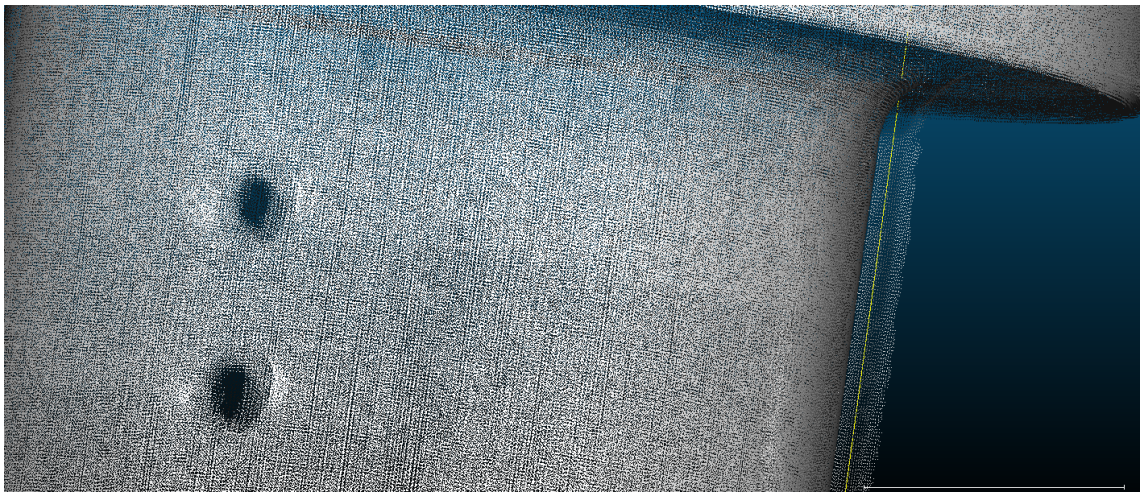


*Figure 8: PointCloud unaligned.*

### Alignment strategies and use of ICP

To carry out the alignment process between the different captured views, the Iterative Closest Point (ICP) algorithm, widely recognized for its efficiency in the fine registration of three-dimensional point clouds, was used.

The ICP algorithm operates iteratively to find the best rigid transformation (rotation and translation) that aligns two sets of points. The general procedure is as follows:

- Initialization**:** one starts from a "source" and a "target" point cloud (e.g., a new view and the one accumulated so far), already approximately aligned.
- Matching**:** for each point in the source cloud, the closest point in the target cloud is searched.
- Transformation estimation**:** the rigid transformation that minimizes the distance between the matched pairs of points is calculated.
- Application and repetition**:** the source cloud is transformed, and the process is repeated until the improvement in the fit falls below a threshold.

One of the key advantages of this system is that, thanks to the extrinsic pre-calibration, all views are captured already approximately positioned in the robot coordinate system. This initial condition provides a very close initial approximation, which significantly accelerates the convergence of the ICP algorithm and reduces the number of iterations required. In contexts where there is no initial estimate, ICP can be slower and less robust, as the risk of converging to incorrect solutions (local minima) increases. In R3-MYDAS, two alignment strategies were tested using ICP:

- Frame-to-frame ICP (Besl, 1992): each new point cloud is aligned only to the immediately previous frame. This approach is computationally efficient, but small registration errors accumulate over time, producing drift and degrading the global reconstruction (Figure 9 left).

- Frame-to-model ICP (Newcombe, 2011): each new view is aligned against a global model that integrates all clouds accumulated up to that point. Although more computationally expensive, this strategy reduces drift and provides higher robustness, stability, and overall accuracy over long sequences (Figure 9 right).

Applying the cumulative alignment strategy with the ICP algorithm, a complete and fused point cloud of the crankshaft was obtained, correctly referenced in the robot coordinate system. The integration of multiple views was consistent and without appreciable discontinuities, demonstrating both the effectiveness of the scanning process and the robustness of the implemented alignment pipeline.

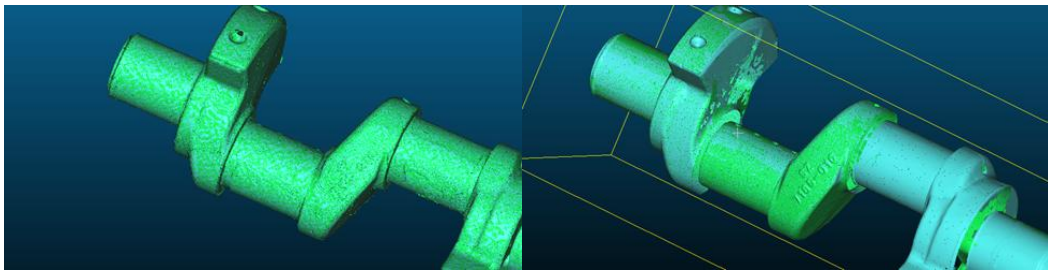


*Figure 9: (Left) Frame-to-frame ICP aligned PointCloud. (Right) Frame-to-model aligned PointCloud.*

However, due to the nature of the capture process-including possible areas with noise, density variation, or small inconsistencies in the overlap between views-certain local surface irregularities were observed in the merged cloud. To correct these defects without losing geometric accuracy, a smoothing process was applied using the Moving Least Squares (MLS) algorithm (Alexa, 2003).

The MLS algorithm works by fitting, for each point, a local surface based on its nearest neighbours, and projecting that point onto that surface. This approach reduces high-frequency noise and improves surface continuity while respecting the overall shape of the model. In this case, a neighbourhood radius adapted to the scale of the object was used, ensuring that the smoothing was effective without degrading relevant geometric details as we can see in Figure 10.

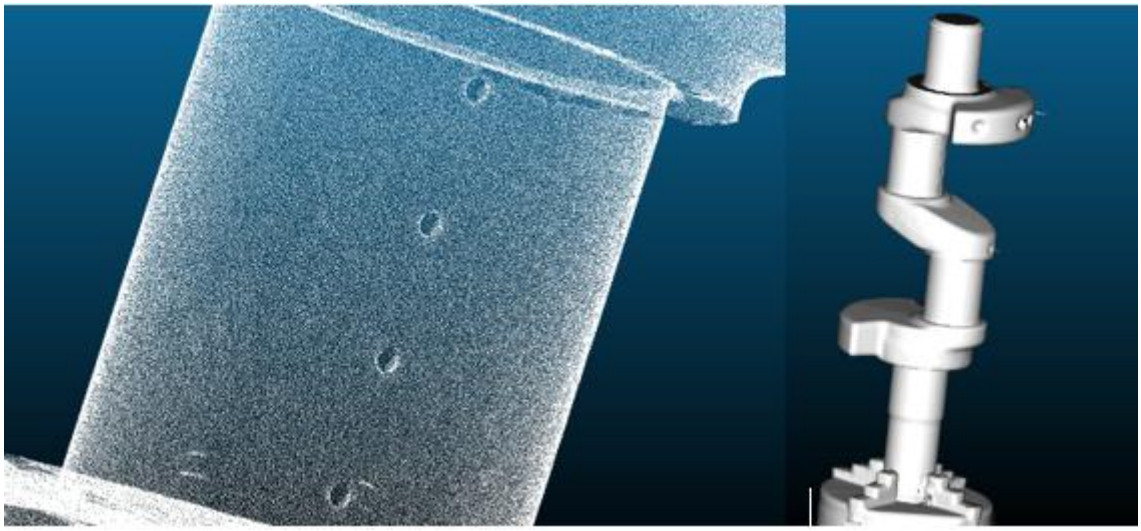


*Figure 10: PointCloud aligned.*

## 2.1.4 Mesh Generation and Surface Reconstruction

Once the merged, aligned and smoothed point cloud was obtained, the next step in the workflow was the generation of a three-dimensional surface mesh. This step is essential to transform the sparse point-based representation into a coherent geometric structure useful for additive manufacturing applications.

### Conversion from point cloud to triangular mesh

To perform the conversion of the point cloud into a continuous surface representation, several mesh reconstruction algorithms were evaluated. Each has specific advantages and limitations depending on the type of geometry, data density and quality of the original cloud. The following algorithms were tested:

- Poisson Surface Reconstruction (Kazhdan, 2006)**:** This method generates a closed mesh from the normal field of the point cloud. It can interpolate areas with moderate gaps and produces visually smooth and continuous results. However, it can introduce artificial geometry in regions where the cloud does not have sufficient information, requiring subsequent cleanup (Figure 11).

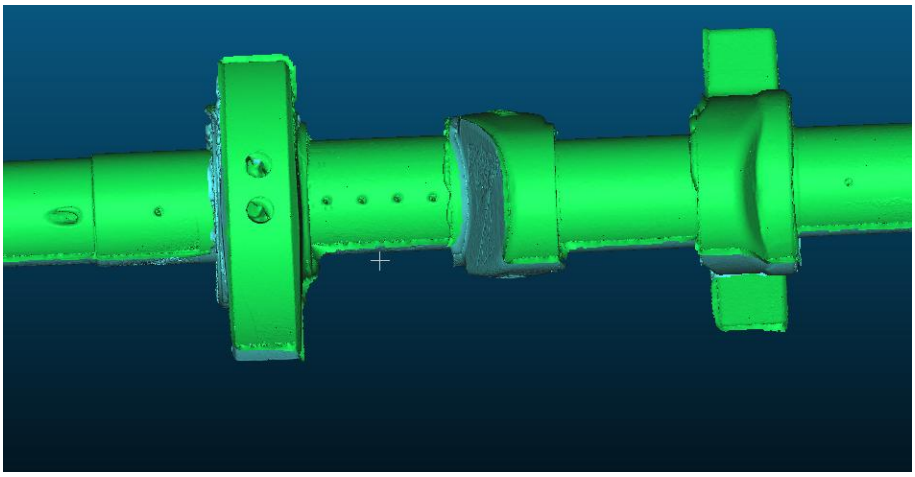


*Figure 11: Poisson surface reconstruction.*

- Greedy Projection Triangulation (Zoltan Csaba Marton, 2009)**:** A local method that connects nearby points according to their neighbourhood, without assuming global continuity. It was useful to faithfully preserve original shapes in areas with good data density. Its main disadvantage is that it can leave gaps in regions with less coverage or complicated geometry.

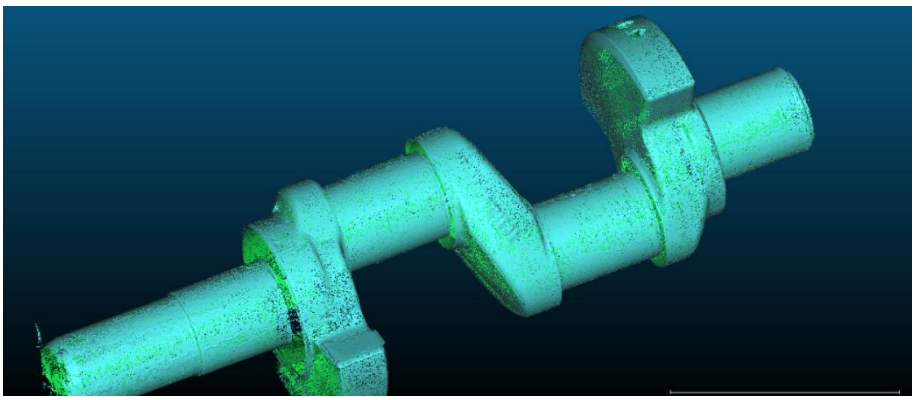


*Figure 12: Greedy triangulation.*

- Ball Pivoting Algorithm (Bernardini, 1999)**:** Based on simulating a sphere that "rolls" between points in the cloud, forming triangles as it encounters neighbouring points. In tests, BPA generated meshes with many gaps, especially in regions where the density of points varied, or the edges were narrow. An attempt was made to improve the result by using several pivot radii, but this solution increased the computational load excessively, being impossible to handle on conventional workstations.

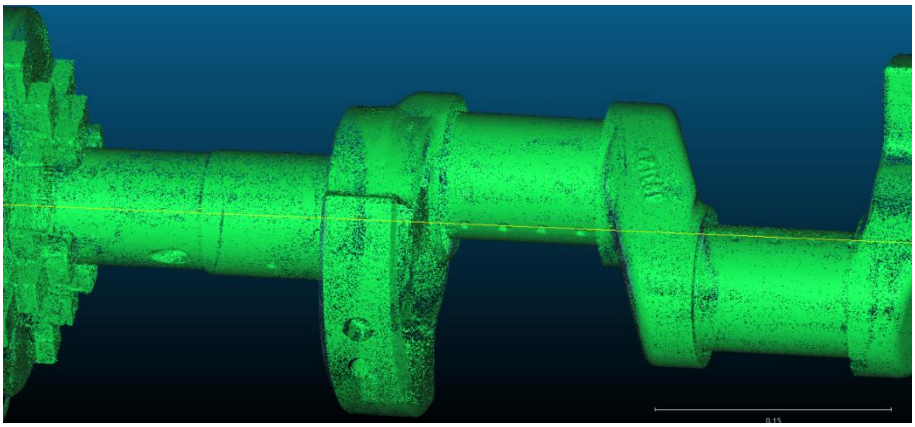


*Figure 13: Ball pivoting reconstruction.*

- Implicit function-based reconstruction (Carr, 2001)**:** Algorithms based on implicit surface reconstruction, which interpolate a surface from functions defined in space (e.g., volumetric methods or by radial support functions), were tested. Although they generated smooth and closed models, in practice they introduced a large amount of invented geometry, filling data-free areas with incorrect shapes, which rendered them unsuitable for reliable industrial use.

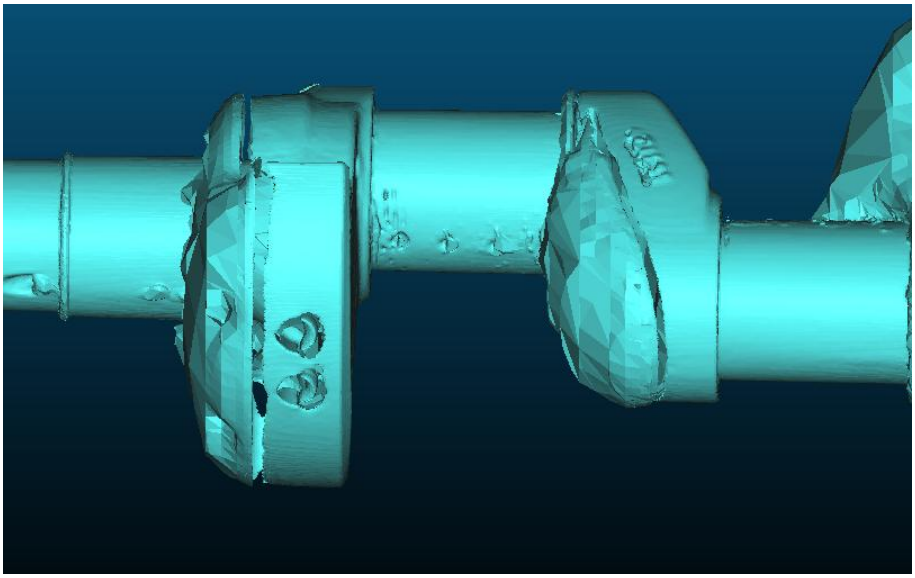


*Figure 14: Implicit triangulation.*

After this comparative evaluation, the Poisson algorithm was selected as the most suitable. Specifically, because it returns continuity and smoothness, while Greedy or Ball pivoting offers better results in areas where geometric details need to be preserved and artificial interpolation avoided.

### Post-processing of the mesh

Once the initial triangular mesh was generated from the merged point cloud, it was necessary to apply a post-processing process to optimize the surface quality and

manageability of the model. This cleaning and refinement pipeline allowed preparing the data for use in CAD environments or subsequent processes, such as deposition or simulation. Post-processing included the following steps:

- Topological error removal: Common artifacts such as degenerate triangles, inverted normals, unwanted open edges or poorly connected regions were corrected.
- Complexity reduction: Simplification algorithms were applied to reduce the number of triangles while maintaining the overall shape of the model. This reduction improves performance in applications that do not require dense representation.
- Laplacian smoothing (Taubin, 1995): This technique that redistributes the mesh vertices to smooth their curvature. Laplacian smoothing works by shifting each vertex towards the mean of its connected neighbours, which suppresses spikes, local noise and hard edges. Mathematically, it involves solving a system based on the discrete Laplacian operator of the mesh, which represents how the local geometry varies at each point. This operator is applied iteratively, controlling the intensity of the smoothing and its global effect.
- Normal reorientation: Finally, surface normals were ensured to be correctly oriented and consistent throughout the mesh, which is essential for rendering and simulation or layered deposition processes.

The final result (Figure 15) was a clean, light and smoothed STL mesh, faithful to the global geometry of the crankshaft and suitable to be used directly in subsequent processes, maintaining its georeferencing with respect to the robot table without the need for additional adjustments.

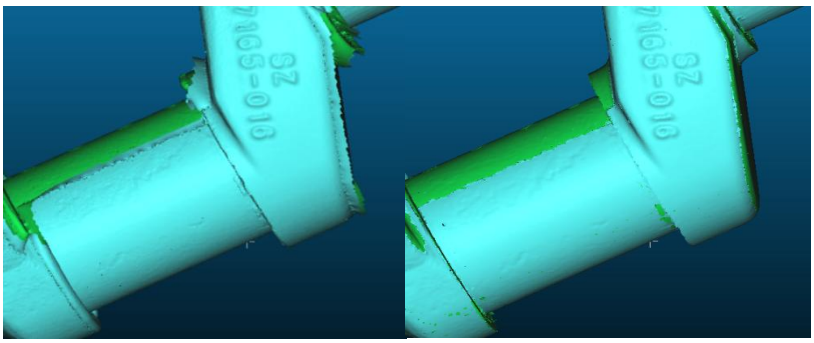


*Figure 15: Final mesh without postprocessing and with processing.*

# 2.2 Path-planning

## 2.2.1 Cell virtualization

### Purpose and Scope

Cell virtualization constitutes a core element of the digital framework developed within WP2. The objective of this activity is to create **accurate digital twins of the robotic cells** used by the project partners, enabling simulation, validation, and execution of both **scanning and repair operations** within a unified software environment.

Although the robotic cells are presented in different configurations in the following figures, **both virtualized cells are designed to support the full remanufacturing workflow**, including geometric acquisition and laser cladding. The illustrated configurations reflect the **specific setups used during the documented validation phases**, rather than permanent or exclusive functional roles.

## 2.2.2 Virtualization of the AIMEN Robotic Cell

### Cell Configuration and Components

The AIMEN robotic cell was virtualized to reflect its physical installation, including all major kinematic and auxiliary components required for crankshaft remanufacturing. The digital model supports both scanning and repair operations through interchangeable end-effector configurations.

The virtualized AIMEN cell includes:

- KUKA industrial robotic arm
- KUKA turntable for controlled rotation of the crankshaft
- Interchangeable end-effector tooling, including:
  - 3D scanning device
  - Laser cladding head (alternative configuration)
- Cell base and reference coordinate systems, aligned with the physical setup

While the configuration shown in the figure depicts the scanning setup, the digital model supports tool exchange and path validation for repair operations as well.

### Role of Virtualization in the AIMEN Workflow

The virtual AIMEN cell enables:

- Simulation of automated scanning routines
- Validation of laser cladding paths prior to execution
- Verification of reachability, standoff distances, and robot orientations
- Early detection of kinematic constraints and potential collisions

By supporting both operational modes, the virtual cell ensures that **software-generated paths are portable across different task configurations** without reprogramming.

The scanning-oriented configuration of the AIMEN cell is illustrated in Figure 16.

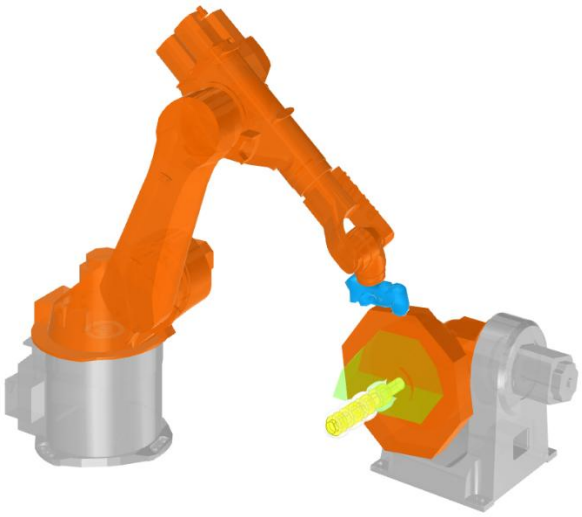


*Figure 16: Virtualized AIMEN robotic cell shown in a scanning configuration, including KUKA robotic arm and turntable. The same cell supports alternative end-effector configurations for repair operations.*

## 2.2.3 Software for Path-planning

### Overview and Objectives

As part of the digital protocol developed within WP2, a dedicated software module for automated path-planning was designed to support both geometric acquisition and robotic repair operations for crankshaft remanufacturing. The software addresses a key industrial challenge: the need to generate reliable, adaptable, and repeatable robot trajectories in situations where nominal CAD data is incomplete, outdated, or entirely unavailable.

The path-planning software operates as a core component within the overall digital workflow, linking scanned data, parametric abstraction, and robotic execution. Its primary objectives are:

- To eliminate manual, operator-dependent robot programming
- To enable rapid adaptation to varying crankshaft geometries and wear conditions
- To ensure consistent surface coverage during scanning
- To generate optimized deposition paths for laser cladding while preserving optimal process parameters such as distance, tilt angle and cladding speed.

The software is structured around two principal stages:

- Parametric abstraction and scanning path generation
- Scan-based analysis and repair path-planning

Each stage is described in detail in the following sections.

### 2.2.4 Step 1 – Parametric Abstraction of the Crankshaft and Scanning Path Generation

#### Motivation and Design Philosophy

In remanufacturing contexts, crankshafts are often handled as individual, non-standardized components, especially when originating from end-of-life machinery. While their precise dimensions may vary, their functional structure remains highly regular.

The software leverages this observation by introducing a simplified parametric representation of the crankshaft. This representation is not intended to replicate the exact surface condition, but rather to capture the essential geometric logic required to plan robust scanning trajectories.

#### Definition of Generalized Crankshaft Parameters

The simplified crankshaft geometry is defined using a limited and intuitive set of parameters that describe its functional anatomy. These parameters include:

- Crankpin radius
- Main journal radius
- Axial length of crankpins and journals
- Eccentricity between crankpins and the main rotational axis
- Number of crankpins
- Axial spacing between successive sections
- Transition and fillet lengths

These parameters form the minimal dataset required to reconstruct a generalized crankshaft topology suitable for path-planning.

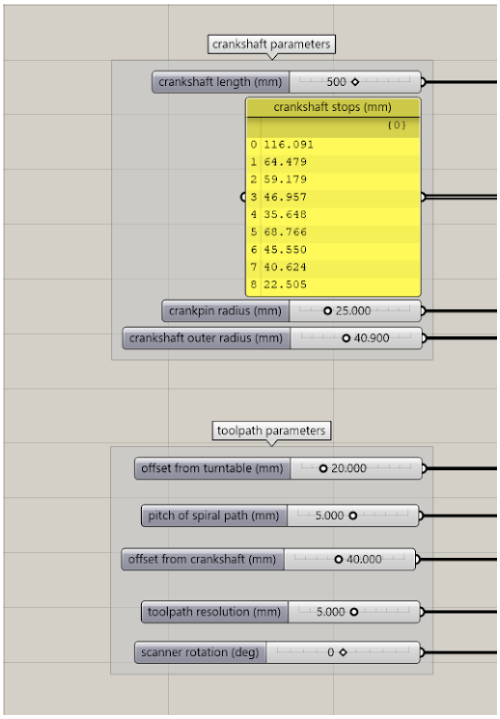



*Figure 17: Parameters defining the simplified parametric crankshaft model, including journal radio, crankpin radio, axial length and eccentricity.*

Based on the defined parameters, the software procedurally generates a synthetic crankshaft geometry composed of analytically defined cylindrical and transitional surfaces. The geometry is constructed around a central reference axis and ensures:

- Topological continuity between all sections
- Correct spatial relationships between crankpins and journals
- Absence of unnecessary surface detail

This simplified geometry acts as a proxy model, sufficient for defining scanner motion while remaining computationally lightweight.

A representative example of such a generated geometry is shown in Figure 18.

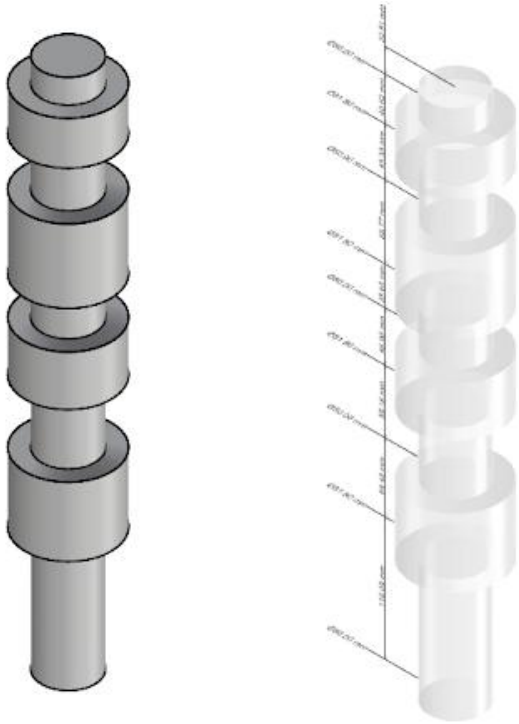


*Figure 18: Example of simplified, parametric crankshaft geometry generated automatically by the path-planning software.*

### 2.2.5 Step 2 – Scan-Based Geometry Analysis and Repair Path-Planning

#### Import of Scanned Geometry

Following the scanning operation, the acquired geometry is imported into the software environment as a mesh representation, typically in STL format. This mesh is generated by the proprietary software of the scanning system and reflects the actual, as-measured condition of the crankshaft, including wear, surface irregularities, and manufacturing deviations.

The mesh is treated as the authoritative geometric reference for all subsequent repair operations.

#### Identification of Functional and Repair-Relevant Surfaces

The software analyses the scanned mesh to identify and classify key functional regions of the crankshaft. This includes:

- Detection of cylindrical regions corresponding to journals and crankpins
- Identification of holes, oil channels, and discontinuities
- Segmentation of surfaces requiring material deposition

Geometric fitting and surface analysis techniques are employed to estimate local axes, radio, and extents. Based on this analysis, working surfaces—i.e. regions where material must be added through laser cladding—are automatically identified.

These identified work surfaces are illustrated in Figure 19.

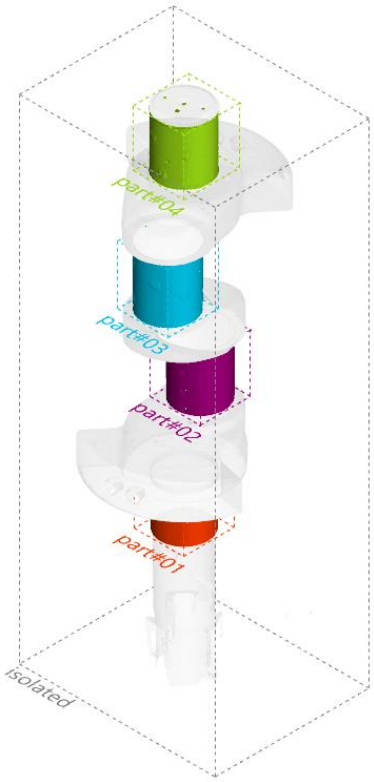



*Figure 19: Identification of functional working surfaces on the scanned crankshaft geometry requiring material deposition.*

### Editable Repair Regions and User Control

Although the identification of repair regions is automated, the software allows controlled user intervention to refine the repair strategy. Operators can:

- Extend or limit the axial length of deposition zones
- Adjust radial offsets to account for variable wear depth
- Exclude sensitive areas from deposition

This hybrid approach ensures both automation and flexibility, allowing expert knowledge to be incorporated without reverting to manual path programming.

### Spiral Toolpath Generation for Laser Cladding

For material deposition, the software generates continuous spiral toolpaths over the selected repair regions. The spiral strategy is particularly suitable for cylindrical surfaces due to its:

- Uniform heat distribution
- Continuous material flow
- Reduced number of start-stop events

The spiral is parameterized using:

- Axial pitch (spacing between successive turns)
- Radial standoff between the welding head and the surface
- Tool orientation derived from local surface normals

The resulting path ensures consistent deposition conditions across the entire repair surface.

### Handling of Holes and Local Discontinuities

Crankshaft geometries often contain holes and oil channels that must remain uncladded. The software automatically detects these features and modifies the spiral toolpath accordingly.

Specifically:

- The spiral path is interrupted before intersecting a hole
- Controlled travel moves are inserted to bypass the discontinuity
- Deposition resumes after the excluded region
- At the termination of the spiral, a circular border path is generated around each hole to define a clean deposition boundary

An example of this spiral toolpath with hole handling is shown in Figure 20.

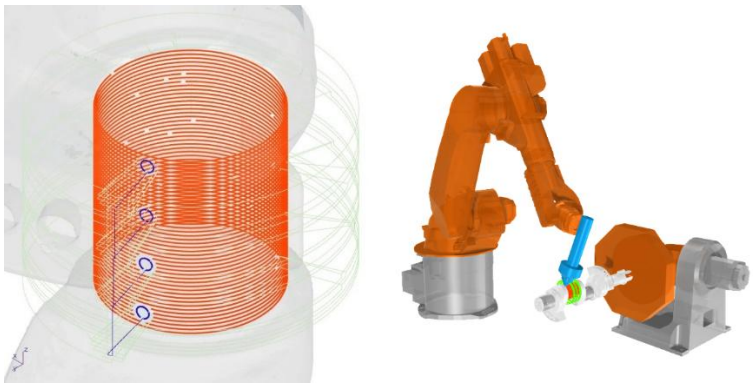


*Figure 20: (Left)Spiral laser-cladding toolpath with interruptions and circular border paths around detected holes. (Right) Laser-cladding toolpath simulation with AIMEN's robot cell.*

### Output Data and Downstream Integration

The final output of the path-planning software includes:

- Robot motion paths for scanning and deposition

- Associated process parameters (cladding speed, overlapping, cladding distance)
- Structured metadata describing repair regions and path segments

These outputs are used for simulation, validation, and execution within the robotic cell, ensuring a seamless transition from digital planning to physical remanufacturing.

A simulation example of this robot program with AIMEN's robot cell is shown in Figure 20 (left).

#### Contribution to Digital and Automated Remanufacturing

The developed path-planning software represents a key technological contribution to the R3-MYDAS digital framework. By combining parametric abstraction with scan-based adaptability, it enables robust automation while accommodating the variability inherent in remanufacturing scenarios.

This approach significantly reduces programming effort, improves consistency, and supports scalable deployment of robotic repair strategies for complex components such as crankshafts.

### 2.2.6 Software Overview

#### Overview

In addition to the underlying geometric and path-planning logic described in the previous sections, a dedicated software application has been developed to provide **structured user interaction**, configuration management, and execution control for the remanufacturing workflow.

The software is conceived as an **operator-oriented digital tool**, enabling non-expert users to configure robotic setups, generate scanning and repair routines, and export executable robot programs without manual coding.

#### User-Configurable Machine Setup

At the initial stage, the software allows the user to **select the target robotic cell configuration**. Predefined machine profiles correspond to the virtualized setups described earlier (e.g. AIMEN, TMCOMAS), and the architecture supports the addition of further configurations in the future.

Each machine profile encapsulates:

- Robot kinematics and motion limits
- Auxiliary axes (turntables, linear tracks)
- Tooling configurations (scanner, welding head)
- Cell-specific reference frames

This approach ensures that all generated paths are automatically adapted to the selected hardware configuration.

### Parametric Definition and Scanning Routine Generation

Once the machine setup is selected, the user can define the **generalized crankshaft parameters** required to generate the preliminary geometric model. These parameters are used to automatically generate the scanning routine, as described in the path-planning section.

This stage requires only high-level inputs and does not rely on detailed CAD models, enabling rapid setup and repeatable scanning operations.

### Scan Import and Repair Routine Definition

After the physical scanning process, the user can **import the scanned geometry** (typically as an STL file) generated by the proprietary scanner software.

Within the same environment, the user can then:

- Review the scanned geometry
- Define or refine repair regions
- Set process parameters required for laser cladding
- Generate the final repair toolpath based on the imported mesh

This step bridges the transition from geometric acquisition to repair planning in a single, continuous workflow.

### Simulation and Program Export

Before deployment, the software allows the generated routines to be **simulated within the virtualized robotic cell**. This enables verification of:

- Reachability and motion feasibility
- Coordination of robot and auxiliary axes
- Absence of collisions or singularities

Once validated, the software exports a **robot-ready program** compatible with the selected robot controller. The exported program can be directly transferred to the physical robot and executed without further modification.

### Frontend Development Status and Future Work

While the **geometric core and path-planning logic** of the software have been largely completed and validated, the **frontend and user interface layer** is currently under active development.

The ongoing frontend work focuses on:

- Improving usability and workflow clarity
- Providing intuitive parameter input and visualization
- Integrating simulation and export controls into a unified interface

The completion and final validation of the frontend is planned as part of **Deliverable D2.3**, ensuring a fully operational and user-friendly software tool by the end of WP2.

## 2.2.7 Mock-up trials

### Objectives and Context

As part of the validation activities within WP2, a series of **mock-up trials** were conducted to evaluate the practical applicability of the software-generated robot programs under real industrial conditions. These trials were carried out during a technical visit by **Ziknes to AIMEN in June 2025**, where the software prototype was installed and tested directly on the robotic cell.

The primary objective of the trials was to **bridge the gap between digital planning and physical execution**, and to assess how assumptions made at the software and simulation level translate to real robotic behaviour.

### Trial Setup

During the visit, robot programs generated using the developed path-planning software were deployed on the AIMEN robotic cell. The tests focused on:

- Execution of automatically generated toolpaths
- Evaluation of motion continuity and process stability
- Observation of system-level behaviour not captured in purely digital simulations

The trials were performed on representative mock-up geometries, allowing controlled observation of the interaction between robot motion, tooling, and the physical setup.

### Observations and Key Learnings

The mock-up trials proved to be highly insightful and highlighted several important aspects of real-world robotic remanufacturing that are difficult to fully capture in simulation environments.

### Digital–Physical Timing and Signal Behaviour

One of the key observations concerned the behaviour of **digital control signals and their associated delays**. While the digital model assumes ideal synchronization between motion commands and process activation, the physical system revealed measurable delays in signal execution.

These observations prompted refinements in how process-related parameters are sequenced and timed within the generated robot programs.

### Toolpath Strategy Evaluation

At the time of the trials, the repair routines relied on **discontinuous circular toolpaths**. Physical execution revealed a systematic issue: material under-deposition at the start

and end points of each circular segment. This effect, while not evident in digital simulation, became clearly visible during the mock-up trials.

This observation was a decisive factor in re-evaluating the deposition strategy and ultimately motivated the transition toward **continuous spiral toolpaths**, which offer:

- Improved material continuity
- Reduced thermal transients
- Elimination of repetitive start–stop artifacts

The adoption of spiral paths represents a direct outcome of the physical validation process.

### Geometric Deviation Between Digital Model and Physical Setup

Another important observation was the presence of a **geometric deviation between the digital model and the physical setup**. A deviation of approximately **10–15 mm** was observed at the far end of the crankshaft, away from the turntable.

This deviation was directional and cumulative, indicating a likely combination of:

- Calibration inaccuracies
- Mechanical tolerances
- Accumulated alignment errors along the crankshaft length

While this deviation did not prevent execution of the mock-up trials, it highlighted the importance of calibration and reference consistency when transferring digitally generated paths to physical systems.

### Impact on Software Development

The mock-up trials played a critical role in **refining the software and path-planning logic**, leading to tangible improvements in:

- Toolpath continuity and deposition quality
- Parameter handling and sequencing
- Awareness of digital-to-physical discrepancies

Rather than being treated as anomalies, the observed deviations were incorporated into the development roadmap and informed subsequent design decisions.

### Outlook and Future Validation

The geometric deviation observed during the AIMEN trials is currently under investigation and is expected to be addressed in upcoming validation phases through:

- Improved calibration procedures
- Enhanced reference alignment strategies
- Additional physical trials under varied configurations

Future mock-up trials will further consolidate the link between digital planning and physical execution, contributing to increased robustness and reliability of the overall remanufacturing workflow.

### Contribution to the R3-MYDAS Validation Framework

These mock-up trials demonstrate the importance of **early physical validation** in the development of digital remanufacturing tools. The insights gained during the June 2025 visit to AIMEN directly influenced the evolution of the software and strengthened its readiness for industrial deployment.

The trials represent a key step toward ensuring that the developed digital tools are not only theoretically sound, but also practically viable in real industrial environments.

# 3 Process Optimization

The process of laser cladding is a well know method of repairing components and structures, which have been widely used in the last years due to their optimal properties compared to traditional methods such as thermal spraying or MIG/MAG welding, where the quality is not always the best. Nevertheless, this process also need from optimization when some conditions meet. The present Use Case involves high carbon content (Table 2) as base plate with hard materials against wear properties, cobalt based alloy. In this situation control and understanding the materials properties under process conditions is a key factor to ensure quality and lack of defects like pores or cracks.

*Table 2: Composition of the baseplate material used for the UC.*

| **Chemical composition %** | | | | | | | |
|---|---|---|---|---|---|---|---|
| C | Mn | Si | P | S | Cr | Ni | Mo |
| 0.4-0.5 | 0.5-0.8 | 0.4 | 0.045 | 0.045 | 0.4 | 0.4 | 0.10 |

As a result of these inherent properties, exist some critical points to consider while manufacturing and in previous stages such as parametrization of the process in order to avoid formation of brittle structures in the Heated Affected Zone (HAZ). Currently this is solved by using preheating temperature to reduce the cooling rate and therefore the formation of these brittle phases. This process of preheating the component requires a high amount of energy and it is time consuming, and it is not aligned with the goals of Made Europe specifically the S01: Efficient, responsive and smart factories and supply chains.

The experiments were conducted using a KUKA industrial robot with a fibre laser up to 8 Kw from Coherent (FL800).

*Table 3: Laser cell main components.*

| | |
|---|---|
| **Spot diameter (at focus) (mm)** | 3 |
| **Wavelength (nm)** | 1070 |
| **Fibre (um)** | 1000 |
| **Nozzle** | 6 jets coaxial |
| **Robot** | KUKA KR60-3 |

In addition, the laser beam configuration was modified, enabling the capacity of the process to fuse material with the same energy due to the increase in the intensity (Figure 21).

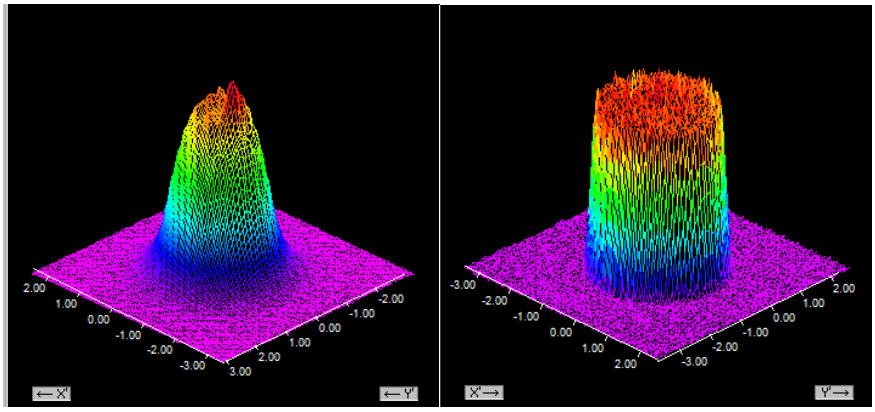


*Figure 21: Beam shape distribution. (Left) Gauss distribution- intensity 1.98 kw/cm2. (Right) Top-Hat - Intensity 12.53 kw/cm2.*

## 3.1 Design of Experiments

A response surface design was established to assess the parameters influencing the process and to quantify both their individual effects and their interactions. This approach facilitates the identification of optimal operating conditions and provides critical information to reduce the environmental impact of the process.

The main goal of this DOE is study and understand:

- Non-linear interactions between parameters and outcomes.
- Interaction between multiple parameters.
- Relationship between factors and outcomes

The factors analysed in Table 4 have been defined according to their relevance to the process and their expected impact on the target responses. The outcomes are related to the main issues associated with the brittle phases formed in the Heated Affected Zone (HAZ Hardness) and with basic information for process optimization (Dilution, Bead Hardness and Ratio). As a result of these levels and factors a DOE of 81 tracks was done without repetitions.

*Table 4: List of factors, levels and outcomes studied in the DoE.*

| Factors | Levels | Outcome |
|---|---|---|
| Tª Preheating (ºC) | 23-150-300 | HAZ Hardness |
| Power (W) | 1500- 2500-3500 | Bead Hardness |
| Speed (mm/s) | 10-15-20 | Ratio Width/Height |
| Powder flow (g/min) | 10-15-20 | Dilution |

The results of each factor solved through a Response Surface Analysis are shown below. The models are evaluated considering the next variables:

- S: Standard deviation of the residuals. Quantifies the average deviation between the observed experimental values and the values predicted by the model. Lowers value of S, indicates better model fit.
- Coefficient of determination ($R^2$): Represents de percentage of the total variability of the response that is explained by the model.
- Adjusted coefficient of determination ($R^2$ Adjusted): The adjusted coefficient of determination corrects $R^2$ value by accounting for both the number of terms included in the model and the sample size.
- Predicted coefficient of determination ($R^2$ Predicted): The predicted $R^2$ evaluates the ability of the model to predict new data points that were not used during model fitting.

### 3.1.1 Dilution

The results shown in Table 5 show that the model is solid and represents in an accurate way the experimental data. Which indicates the goodness of the fit and predictive capability of the model.

*Table 5: Model summary for dilution.*

| S | R square | Adjusted R square | Predicted R square |
|---|---|---|---|
| 0.0666667 | 99.74% | 99.57% | 99.27% |

The Pareto chart show the most important factor/parameter that affects the dilution is laser power, followed by speed and powder flow. The model also shows that there is no notorious effect of a parameter's combination in the dilution.

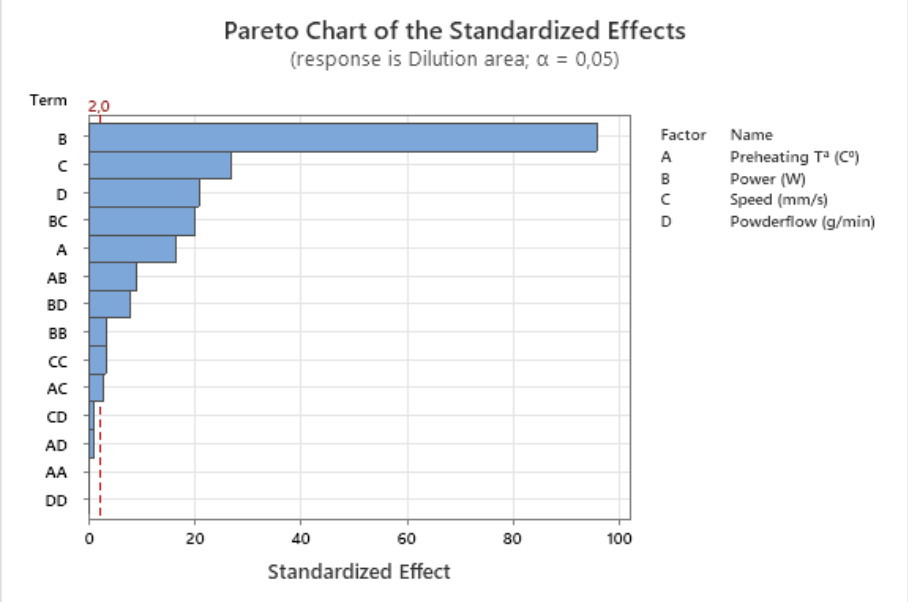



*Figure 22: Pareto chart for Dilution area.*

Figure 23 shows the direction of the variation for the factors, as indicated the power has a positive effect on the dilution. By contrast, an increase of speed or powder slightly flow reduces the dilution area.

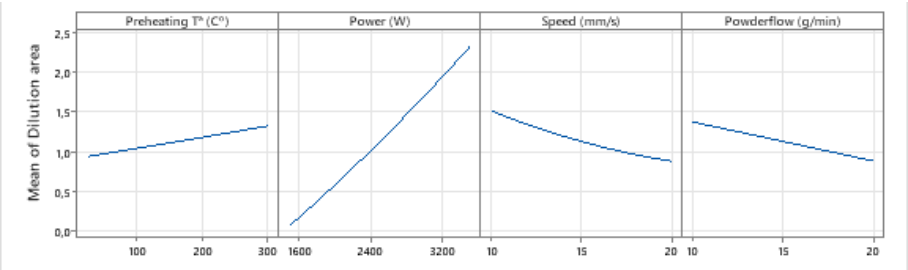



*Figure 23: Main effects on Dilution area.*

Figure 24 shows the interaction effect between all the factors and as it was indicated previously the most important variations are made by power modifications. Meanwhile other interactions as powder flow-speed, speed-preheating Tª and preheating Tª – powder flow have low effect on the dilution area.

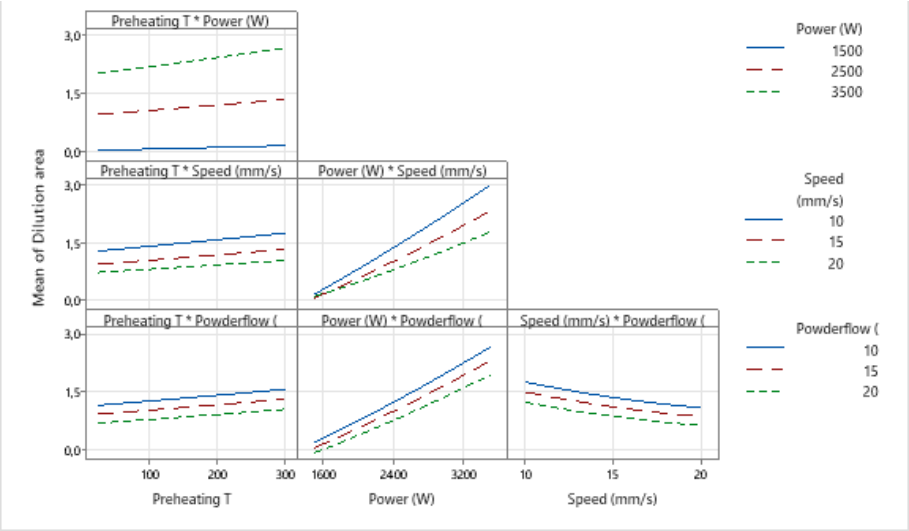



*Figure 24: Interaction plot for Dilution area.*

## 3.1.2Width

The results showed in Table 6 confirm that the model is solid and represents in an accurate way the experimental data. Which indicates the goodness of the fit and predictive capability of the model.

*Table 6: Model summary for Width.*

| S | R square | Adjusted R square | Predicted R square |
|---|---|---|---|
| 0.0393446 | 94.60% | 91% | 84.62 |

The Pareto diagram (Figure 25) shows the main factor affecting the track width is laser power followed by speed and preheating Tª. As in the previous case, for the width there is no combination of parameters that affect the track width.

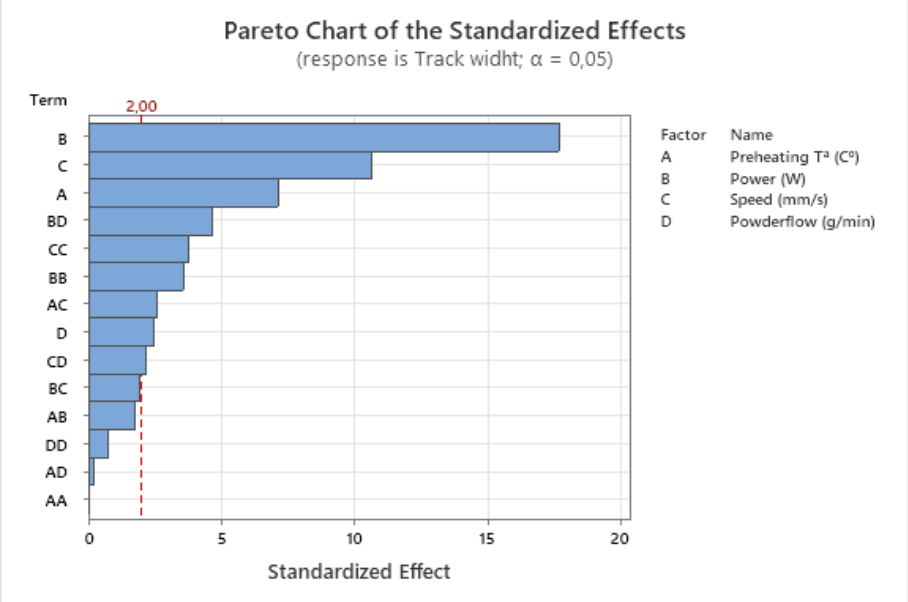



*Figure 25: Pareto chart for Width.*

The direction of variation is shown in Figure 26, the main influencing factors are laser power and speed, both of which exhibit a tendency towards stabilization at high power and high-speed values. The increase of power leads to an increase in width that progressively tends to stabilize. By contrast, an increase in speed reduces the width drastically at lowers speed then tends to stabilize.

The preheating Tª and powder flow has no relevance in the track width.

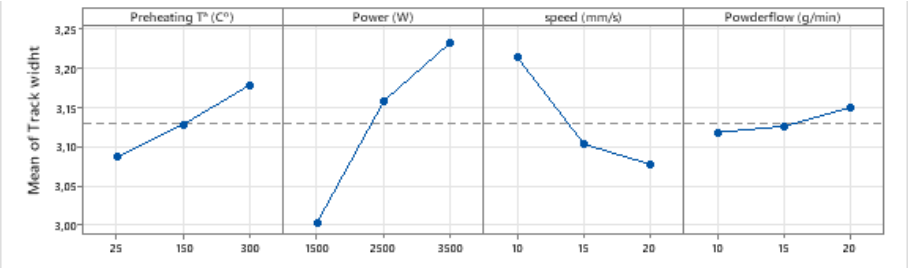



*Figure 26: Main effects for Track Width.*

Considering these effects on track width one of the results is a contour plot for defining a process window for different track width options. Figure 27 indicates for different boundary conditions the window parameters to obtain a wanted value of track width. In this unique sense, the main interest is to maximize the track width to reduce the time of manufacturing, by contrasts this affect to the energy usage of the process.

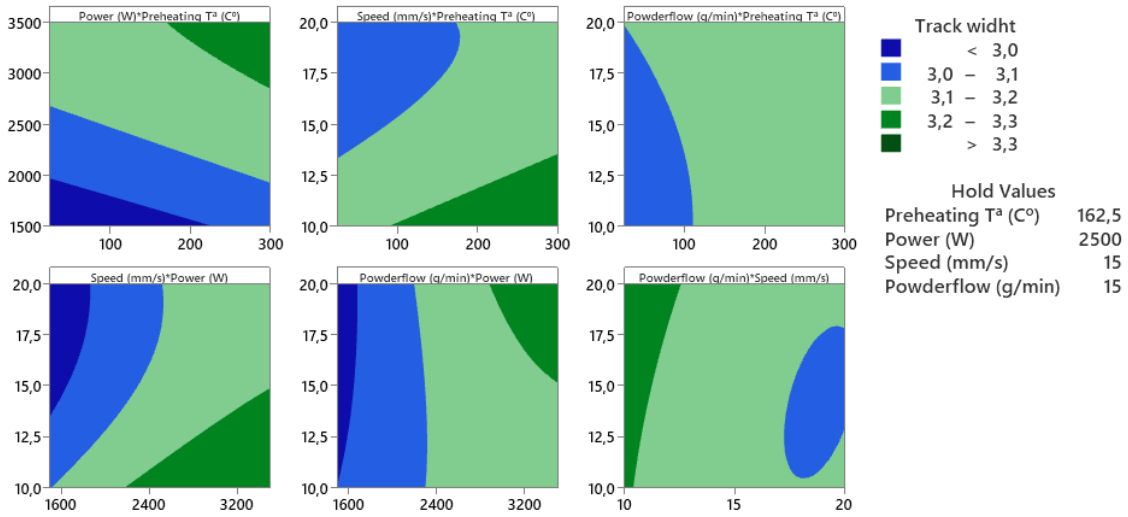



*Figure 27: Contour plots for track width.*

## 3.1.3 Height

The results showed in Table 7 confirm that the model is solid and represents in an accurate way the experimental data. Which indicates the goodness of the fit and predictive capability of the model.

*Table 7: Model summary for Height.*

| S | R square | Adjusted R square | Predicted R square |
|---|---|---|---|
| 0.0290354 | 99.40% | 98.99% | 98.28% |

The Pareto diagram shows in Figure 28 the main factor affecting the track height. In this case the predominant parameters are the powder flow and speed. Also indicates that there is an interaction between powder flow and speed that has a notorious effect. By contrast, the laser power plays a secondary role.

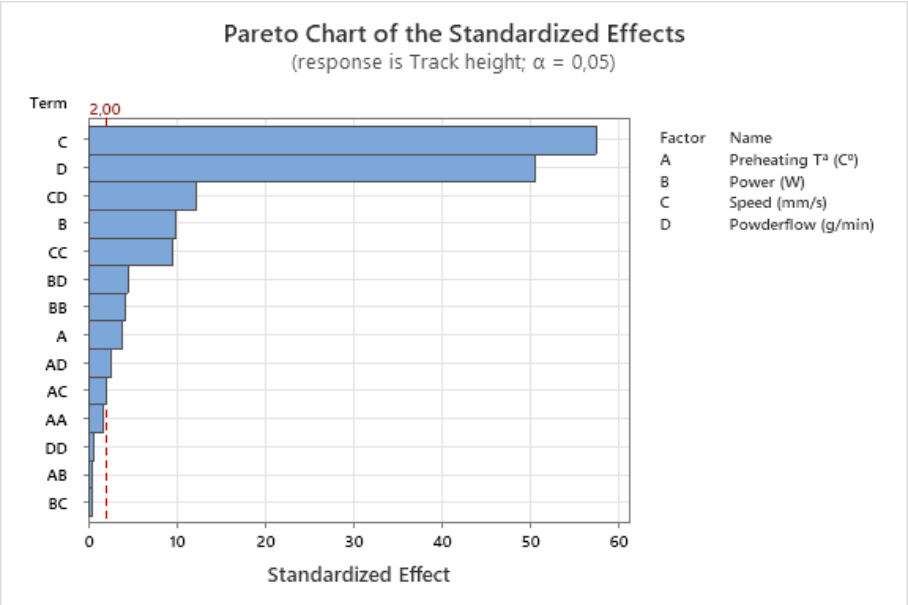



*Figure 28: Pareto chart for Height.*

As mentioned before, the main factors are speed and powder flow. Figure 29 shows the direction of the variation for different factors. At studied levels there is a linear relationship between powder flow and the track height. In the case of speed the relationship is quasi-linearly inverse: as speed increases, the track height decreases.

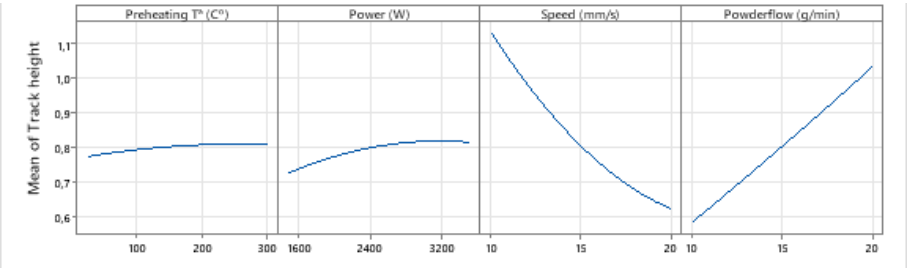



*Figure 29: Main effects plot for Track Height.*

The interaction plot (Figure 30) shows soft interactions between parameters as expected. Uniquely for the interaction between powder flow and speed as we showed in the Pareto diagram (Figure 28). At higher powder flow rates when the speed is reduced the tracks height is drastically reduces compared to when it happens at low powder flow, where a change in the speed does not affect drastically to the track height.

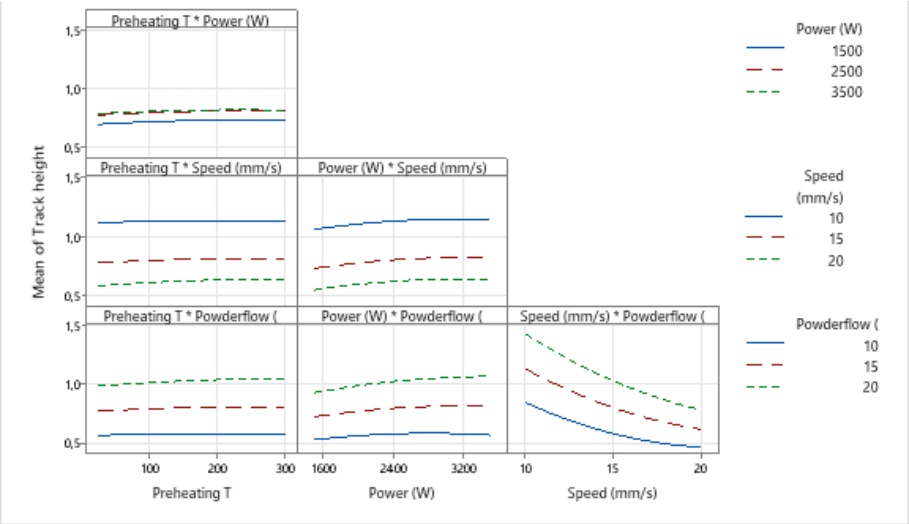



*Figure 30: Interaction plot for Track Height.*

## 3.1.4 Ratio Width/Height

The results showed in Table 8 confirm that the model is solid and represents in an accurate way the experimental data. Which indicates the goodness of the fit and predictive capability of the model.

*Table 8: Model summary for Ratio Width/Height.*

| S | R square | Adjusted R square | Predicted R square |
|---|---|---|---|
| 0.353381 | 95.27% | 94.27% | 91.92% |

The Pareto diagram (Figure 31) shows the main factors affecting the Ratio Width/Height. This is mainly influenced by the factors that affect the track height, letting the laser power in a secondary plane. This means that ratio is governed by track height only and the laser power has no significant relevance. Also, as in the case for track height the combination of powder flow and speed has more important effect than laser power (Table 9). The results indicate that speed and powder flow have a significant effect on the height-to-width ratio, as reflected by the F-values in Table 9. This is mainly because these factors influence the track height much more strongly than the track width.

*Table 9: F- Values for different factors and outcomes.*

| | F-Value (Track Height) | F-Value (Track Width) | F-Value (Ratio) |
|---|---|---|---|
| Power | 97.88 | **312.79** | 4.99 |
| Speed | **3302.93** | 112.86 | 645.89 |
| Powder flow | **2557.91** | 6.18 | 598.56 |

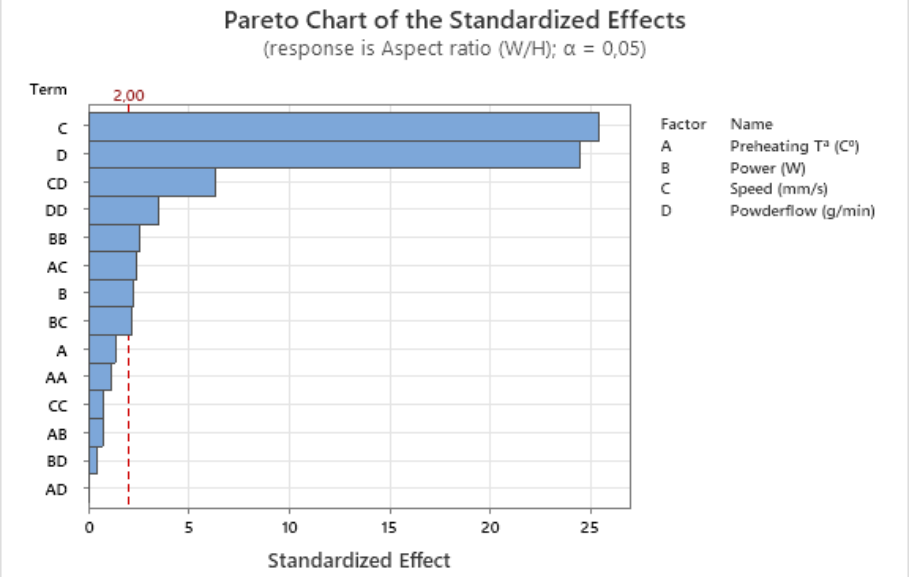



*Figure 31: Pareto chart for Ratio Width/Height.*

The main effects plot (Figure 32) indicates the strong effect of speed and powder flow in comparison to laser power or preheating. The speed is directly proportional to the ratio, by contrast an increase in the powder flow decreases the ratio Width/Height).

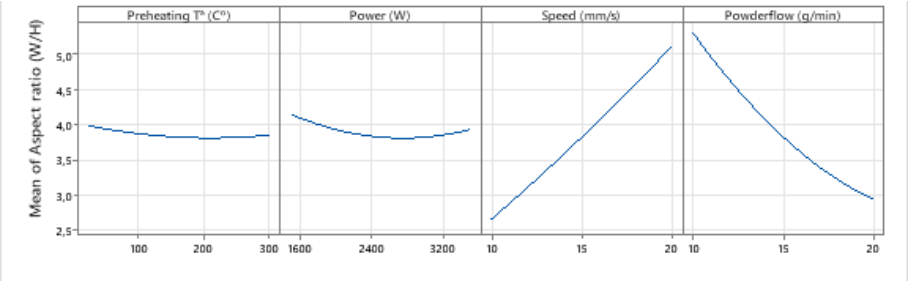



*Figure 32: Main effects plot for Ratio Width/Height.*

## 3.1.5 Bead Hardness

The results showed in Table 10 confirms that the model is solid and represents in an accurate way the experimental data. This model has low prediction accuracy compared to previous models, also de the standard error is higher, but it keeps a low level.

*Table 10: Model summary for Bead hardness.*

| S | R square | Adjusted R square | Predicted R square |
|---|---|---|---|
| 29.0448 | 95.94% | 93.24% | 88.45% |

The Pareto diagram shows the most relevant factors affecting the Bead Hardness. The main factor is the combined effect of laser power and powder flow followed by laser power and powder flow.

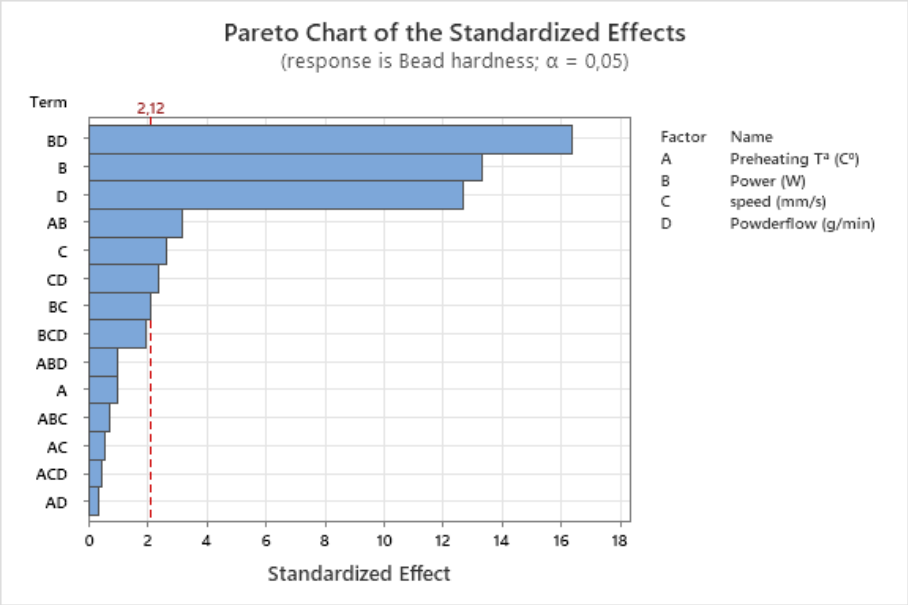



*Figure 33: Pareto chart for Bead Hardness.*

The main effect plot indicates non lineal behaviour between power and powder flow with hardness. In the case of power there is a minimum at 2500W, this contrasts with the theoretical expectation of a linear decrease in hardness with increasing laser power, rather than the presence of a minimum. In the other hand, the speed and preheating temperature has no significant effect on the bead hardness.

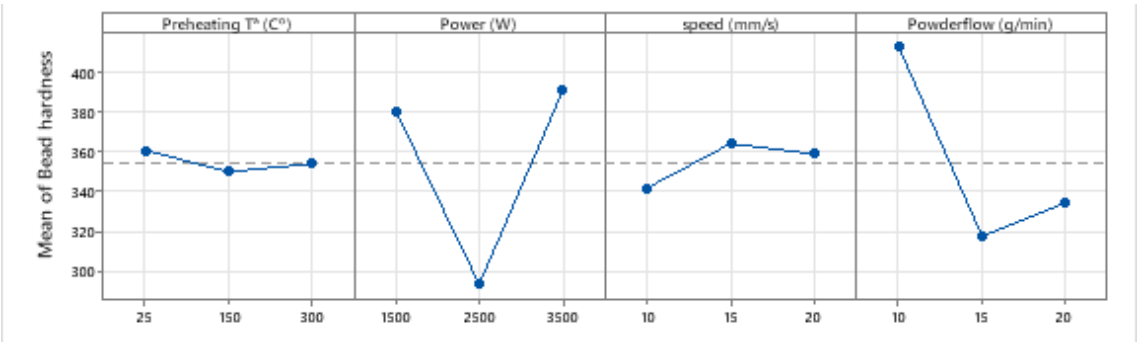



*Figure 34: Main effects for Bead Hardness.*

The interaction plot Figure 35 indicates normal results as expected. However, the interaction between laser power and powder flow is generating an anomaly in the material properties of the cladded material. As is shown in Figure 35, for 10 g/min and 3500W condition there is an unexpected increase in the bead hardness. This achievement indicates that not only the parameters can affect the material hardness also can exist a combination of them that affect drastically the material properties.

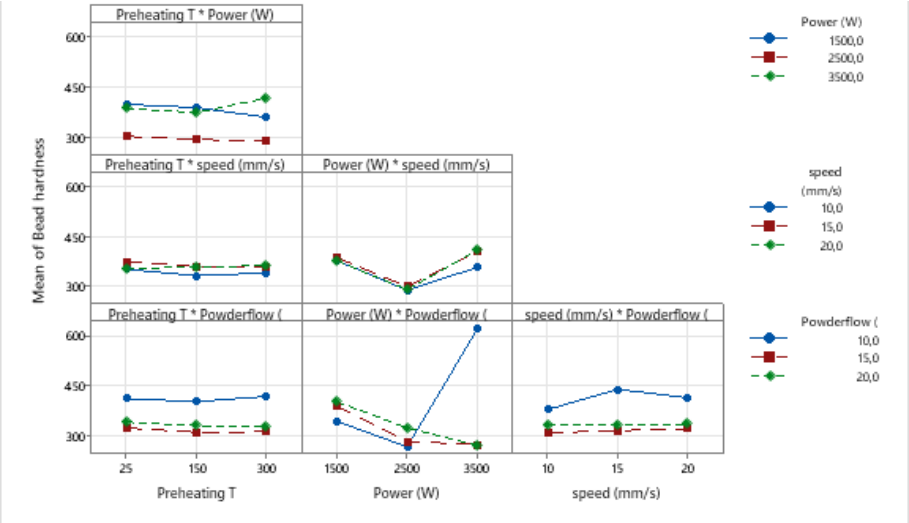



*Figure 35: Interaction plot for Bead Hardness.*

To verify the results a box diagram Figure 35 was done to evaluate the possibility of experimental error during measuring. However, the boxplot shows that, despite the variation of the hardness in that condition, the results are still bigger than the other conditions.

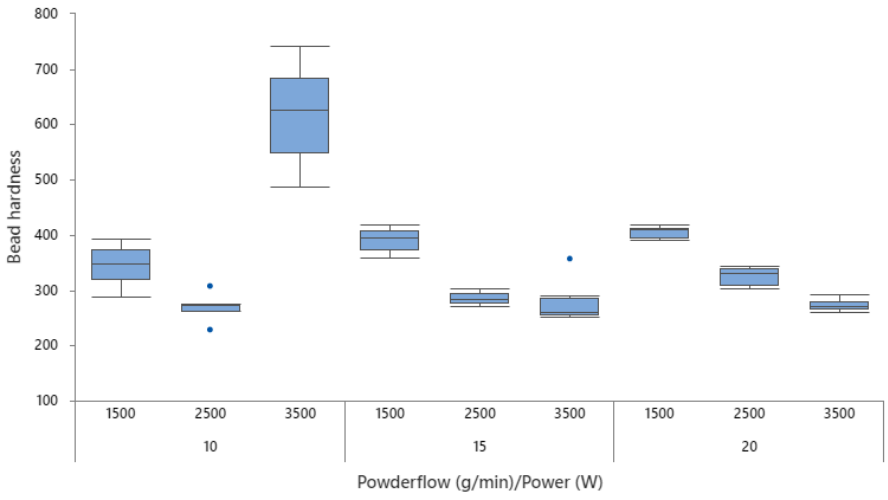



*Figure 36: Box diagram of Bead Hardness for various power and powder flow.*

The footprints (Figure 37) shows the real difference in the bead hardness for a track with a variation in the powder flow.

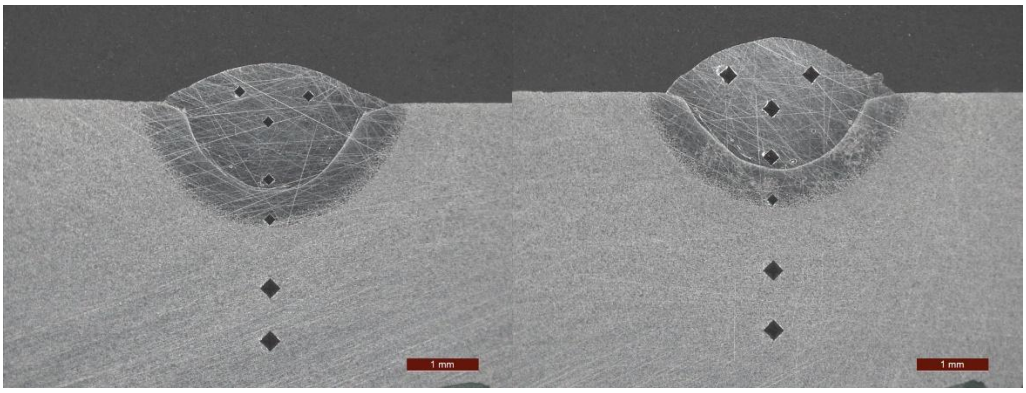



*Figure 37: Hardness footprint for (Left) 20 g/min (Right) 10 g/min. Fixed parameters: Power 3500W, Speed 15 mm/s.*

A detailed characterization of the microstructure (Figure 38) shows a cellular/ dendritic microstructure very similar in both examples, not explaining the huge variation of hardness.

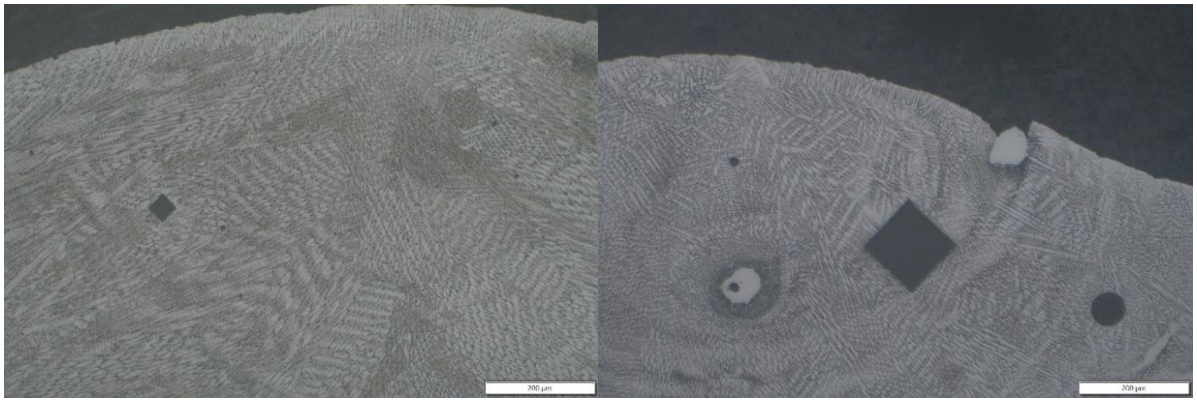


*Figure 38: Micrography's at 100x of (Left) 20 g/min (Right) 10 g/min.*

### 3.1.6 HAZ Hardness

The results showed in Table 11 confirm a low standard error, the model is solid and represents in an accurate way the experimental data. In addition, the model has a good ability to predict new data points.

*Table 11: Model summary for HAZ hardness.*

| S | R square | Adjusted R square | Predicted R square |
|---|---|---|---|
| 22.7667 | 96.90% | 96.65% | 96.31% |

The Pareto diagram show in Figure 39 shows the most relevant factors affecting the HAZ hardness. In this case the preheating temperature is the main factor being four times stronger than the previous one, the speed.

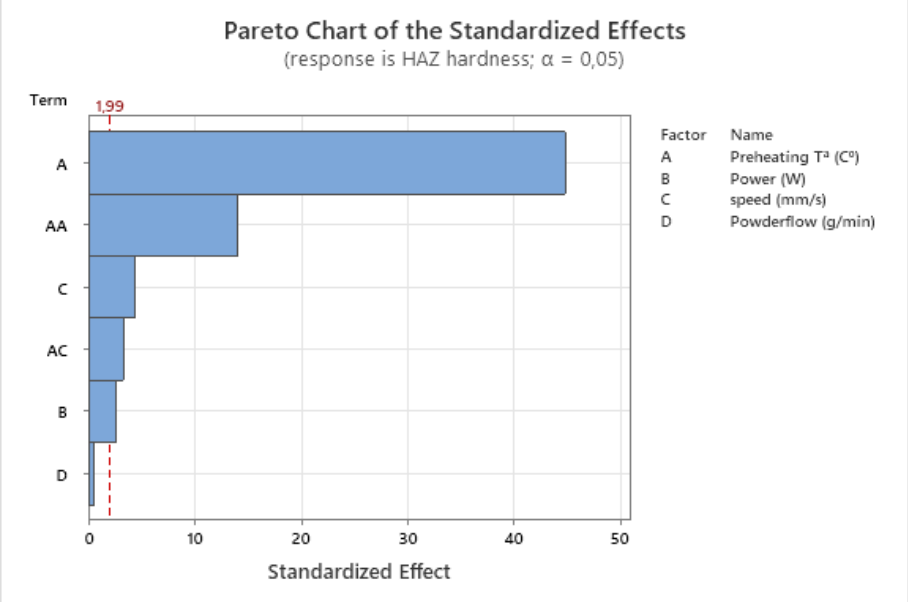



*Figure 39: Pareto chart of HAZ Hardness.*

The main effects plot indicates, as expected, the high impact that the preheating temperature makes in the Hardness HAZ. By contrast, the laser power, speed and powder flow has an insignificant effect.

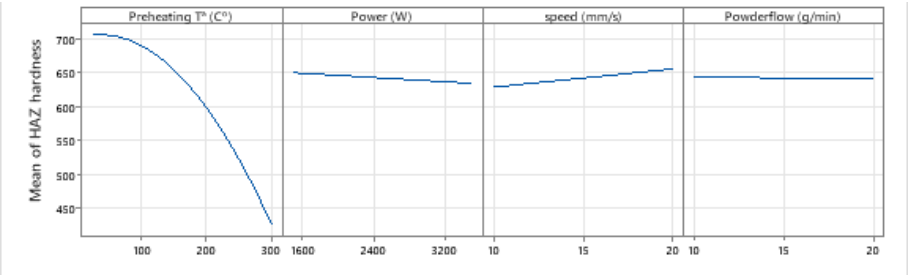



*Figure 40: Main effects on HAZ Hardness.*

A more detailed analysis of this behaviour is presented below in Figure 41. The graph shows the relationship between hardness and preheating temperature for different cases of powder flow.

The results indicate that for that combination of parameters there is no interaction between them that makes an unexpected outcome.

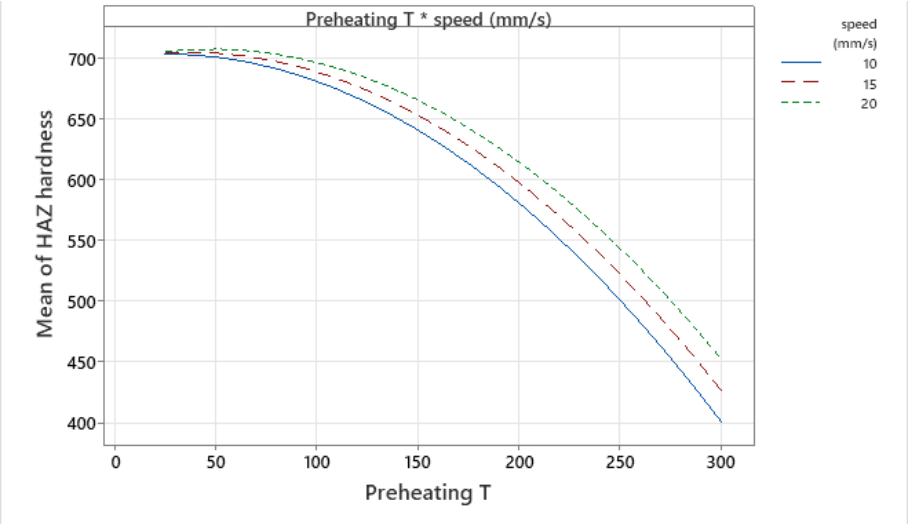



*Figure 41: Interaction plot for HAZ Hardness and powder flow.*

The box plot shows a moderate level of dispersion for the tracks manufactured at 300ºC. In contrast, the dispersion for the remaining data is very low, which support the results predicted by the model.

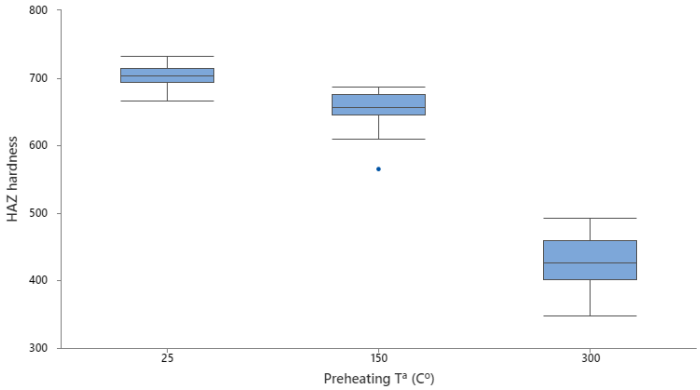



*Figure 42: Box plot for HAZ Hardness.*

In addition, a hardness detailed characterization of the HAZ was performed to analyse possible variations along it. For that reason, an array of indentations was performed (Figure 43). The results show a variation of 25% approximately, this should be taken into consideration for the conclusions due to possible changes in the model accuracy because of the heterogeneity of the measurements.

*Table 12: Hardness measurements in HAZ.*

| Indentation | Hardness HV1 |
|---|---|
| 1 | 741 |
| 2 | 728 |

| | |
|---|---|
| 3 | **575** |

These small variations that depends on the zone where the indentation was made can conduct to a loss of information, in the sense that the error is in the same scale that the possible variations due to modifications in the parameters such laser power, speed or powder flow.

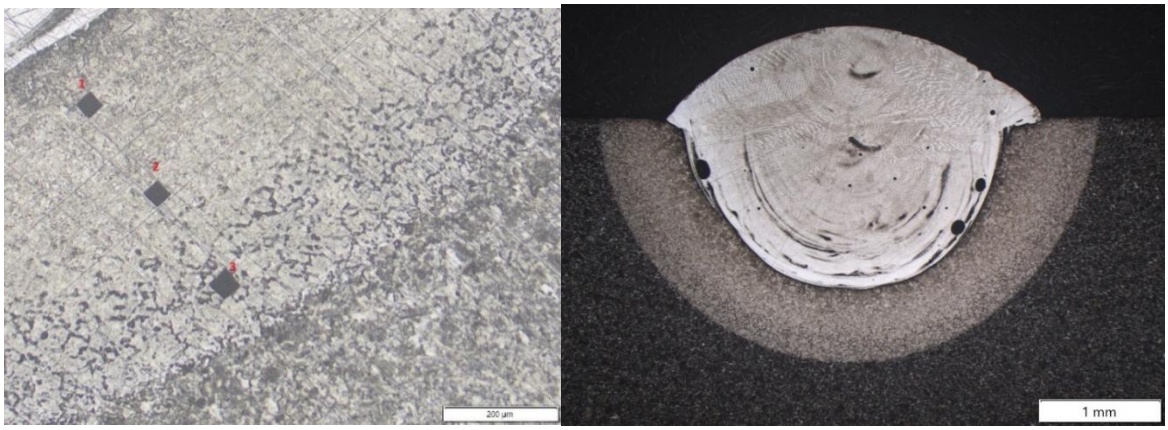



*Figure 43: (Left) Hardness footprint HV1. Indentation 1 to 3 from left to right. (Right) macrography of single track.*

### HAZ Hardness DOE without preheating

In order to further analyse the previous behaviour related to the hardness in the HAZ we solve the DOE without including the preheating temperature factor. This aims to discover if there is any other parameter involved in the hardness. The results show a high error rate without any capability of predicting data outside the values studied.

*Table 13: Model summary of HAZ Hardness without preheating factor.*

| S | R square | Adjusted R square | Predicted R square |
|---|---|---|---|
| 131.207 | 1.24% | 0% | 0% |

In addition, the Pareto chart (Figure 44) indicated none of the factors reach the minimum level to consider themselves as a factor that affect the outcomes, in this case the HAZ hardness.

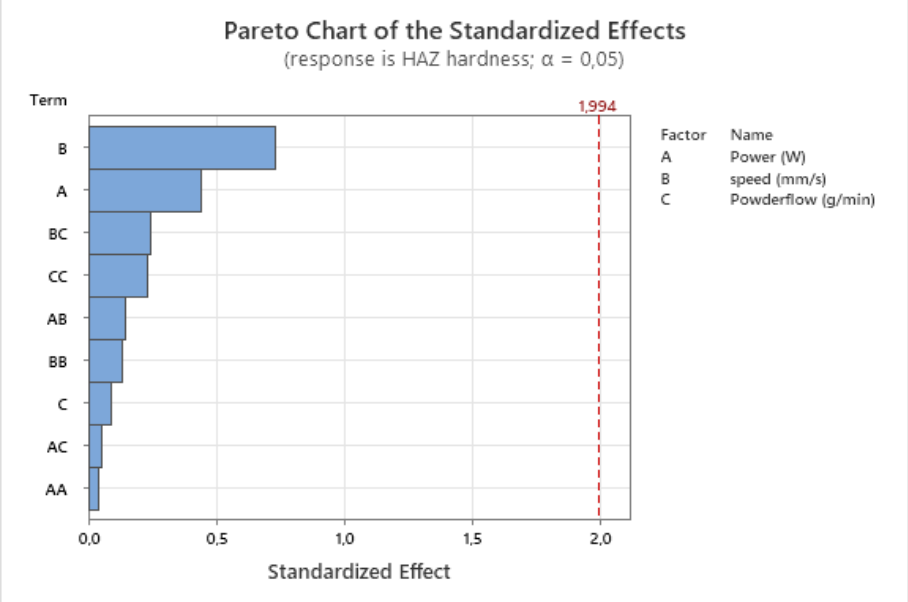



*Figure 44: Pareto chart for HAZ Hardness without preheating.*

This concludes that the main parameter affecting the hardness in the HAZ is the preheating temperature. Nevertheless, due to the high number of trials, it was not possible to guarantee indentations in the same area of the HAZ, which could be the reason for the low accurate model when we do not consider the preheating temperature.

## 3.2 Simulation analysis

In this study, ad hoc numerical simulations were performed in conjunction with infrared monitoring of surface temperatures before and after metal additive manufacturing. The objective was to evaluate the response of the deposited material and the overall component in terms of distortions and residual stresses. The results of these analyses aim to establish the foundation for defining an effective manufacturing strategy that minimizes defects caused by distortion and residual stress inherent to the process

To properly understand the role of simulation in this task, it is necessary to introduce the challenges associated with metal additive manufacturing (AM). The thermal cycle in AM is characterized by extremely rapid heating and cooling rates, as well as melt-back phenomena in which the newly deposited layer partially remelts the previously solidified material. These effects generate residual stress that, on the macroscopic scale, can lead to distortions during processing and compromise the functionality of the final component.

Residual stress formation in AM shares many similarities with welding. During heating, the feedstock material expands under the influence of a high-energy heat source, but this expansion is constrained by the surrounding cooler material, producing compressive stresses. As cooling occurs, shrinkage in the heated zone is partially restrained by plastic deformation induced during heating, resulting in tensile residual

stresses in the deposited layers, balanced by compressive stresses in adjacent regions. In the layer-by-layer build-up process, repeated remelting and solidification cycles further amplify these stress gradients.

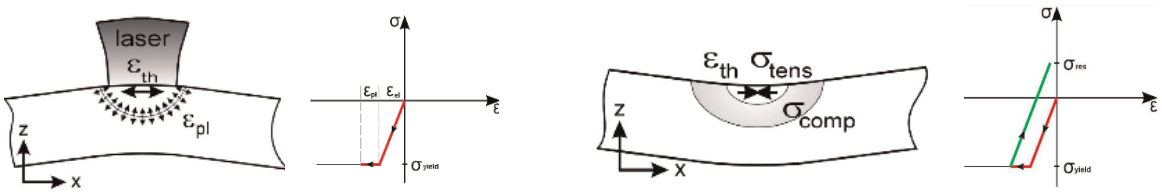



*Figure 45: Simplified representation of thermal stress and strains formation during heating and cooling.*

In a practical AM process, the residual stress field is much more complicated since the number and pattern of heat source path and heat transfer are extremely complex. Residual stresses can be categorized based on different length scales: Type I, Type II, and Type III Type I residual stresses occur at the macro level. Type II stresses, or microscale stresses, are typically present due to anisotropic material properties at the grain scale. Type III stresses are at the nanoscale and arise from coherency and dislocation effects. Type II and Type III residual stresses have a minimal impact on the material's mechanical properties and generally fall outside the scope of most current measurement techniques. The residual stresses discussed in this work refer to Type I stresses, as these macroscopic stresses have a more pronounced effect on the surface integrity of AM metal parts.

Finite Element Method (FEM) software is valuable for predicting the evolution of residual stress in the early stages of manufacturing. By allowing for the modification and simulation of design parameters during the manufacturing process, these tools can help ensure the quality of 3D printed components. Residual stresses are permanent internal strains that result from thermal loads applied during the printing process, and these stresses can be modelled on a macroscopic scale. Other types of residual stresses, such as those induced by phase transformations, also develop during manufacturing and processing. Phase changes in the material affect its thermo-mechanical properties, and these can be modelled at a microscopic level, not included on this work.

The finite element approach adopted in this work is a part-scale (macro-scale) model aimed at predicting the global behaviour of additively manufactured components, particularly residual stresses and deformations as a function of process parameters. Micro-scale phenomena such as grain structure formation, melt pool geometry, and microstructural evolution are not considered, as they have a negligible influence on part-level behaviour and would significantly increase computational cost. Due to the high computational resources required, it is impractical to employ a single model that captures all physical aspects of the additive manufacturing process. Therefore, appropriate simplifications are introduced to enable efficient simulations while

preserving sufficient physical accuracy. These include the use of an equivalent heat source model to represent transient thermal effects instead of explicitly modelling laser–material interaction.

Although thermo-mechanical finite element simulations are widely used to estimate residual stresses in additive manufacturing, their high computational demand—arising from transient heat sources, nonlinear material behaviour, and reliance on accurate material data—limits their applicability to small or simple geometries. For components involving multiple laser tracks, fully coupled thermo-mechanical simulations become computationally prohibitive, justifying the use of simplified part-scale modelling strategies for reliable global behaviour prediction. This is the main reason the simulation will be carried out on test coupons of reduced dimensions, so that different strategies can be evaluated at this level and the achieved results can be extrapolated to the demo case. Even so, due to the size of build track, these coupon models involve a high computational cost, so simplifications like lumping type had been included.

### Initial FEM Development and Calibration Approach

Residual Stress Prediction: As explained previously, during the additive during the additive process, components may develop excessive residual stresses, leading to distortions and dimensional inaccuracies. Predicting these stresses before manufacturing is critical for process optimization. If simulations indicate high residual stress, corrective actions such as modifying the base plate, clamping conditions, or scanning strategy can be implemented.

The initial goal of this work is to evaluate the effects of different scanning strategies on residual stress and distortion during Directed Energy Deposition (DED) processes using macro scale models. To achieve this, we start with simple additive manufacturing trajectories, manufactured them experimentally, simulated their behaviour, and calibrate the model parameters based on experimental data. Once calculated, the model is validated against additional simple trajectories to ensure consistency and reliability.

Several basic scanning strategies were considered for initial simulations and experimental trials:

- Test 1: Unidirectional Strategy: Printing in a single direction throughout the entire process, either horizontally or vertically.
- Test 2: Zig-Zag Strategy: Alternating scanning directions within each layer, whit consecutive tracks reverse direction.
- Test 3: Concentric Strategy: Deposition follows concentric paths within the layer.

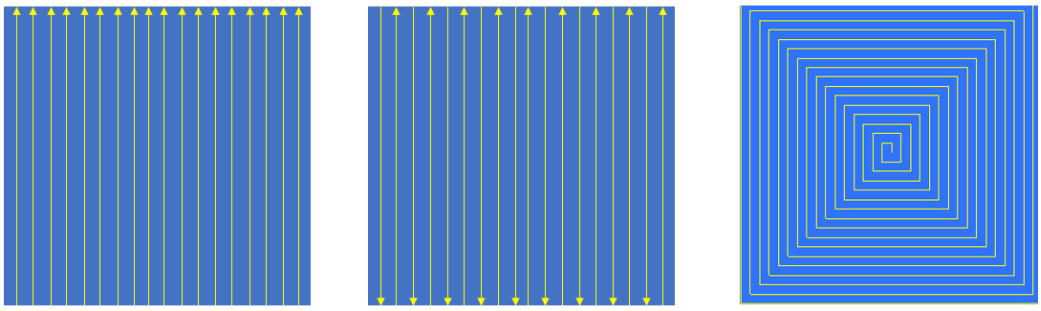


*Figure 46: Scanning paths (Left) Raster, (Center) Alternate raster, (Right) Concentric.*

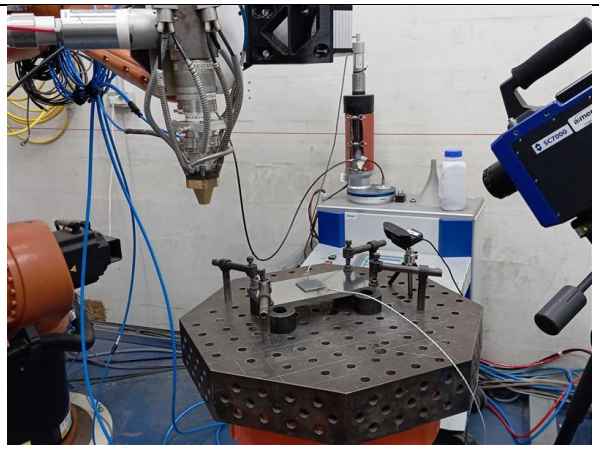
These strategies can be repeated across layers or combined by changing directions between layers to mitigate residual stress accumulation.

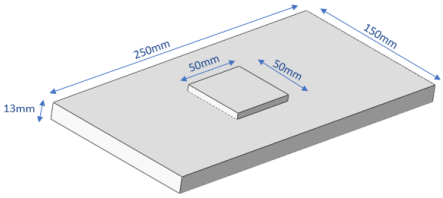
### Simulation Framework

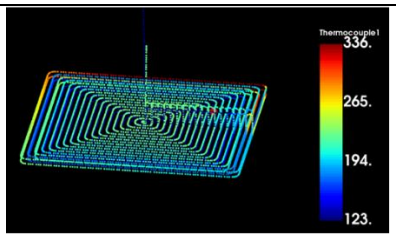
For the simulations, Simufact Welding was used as a finite element-based framework capable of transient, nonlinear, coupled thermo-mechanical analysis, suitable for modelling Directed Energy Deposition (DED). This approach allows accurate prediction of thermal cycles, material fusion, and the resulting residual stresses and distortions under a moving heat source. While general-purpose FEM software can perform nonlinear thermo-mechanical analyses, DED simulations require specialized features to efficiently model sequential deposition and heat input.

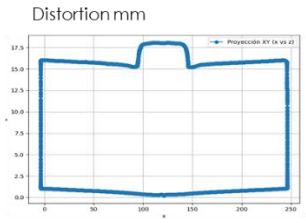
The simulations employed an implicit transient formulation, providing detailed results for temperatures, deformations, and displacements. To reduce computational cost for longer deposition paths, a meta-transient strategy was applied, discretizing deposition into simplified segments while maintaining essential thermo-mechanical behaviour.

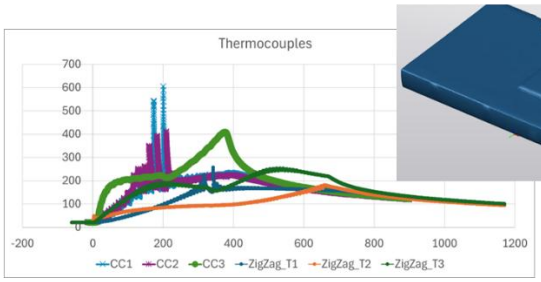
### Experimental Setup and register

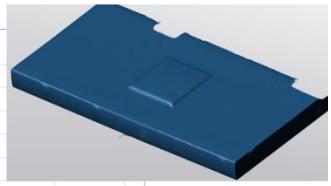
| | | |
|---|---|---|
| **SET UP** |  | Laser Source: RofinFL080<br>Coherent Laser Head 3mm spot<br>Monitoring devices<br>Thermocouples<br>Infrared camara |

<table>
<tr>
<td>MOCK UP</td>
<td>

<br>Base Plate: Dimensions 250 × 150 × 13 mm, material F114 clamped at four corners.<br>Additive Material: Stellite 21<br>Geometry: Square patch, 50 × 48.64 × 3.4 mm.</td>
<td>Layer Specifications:<br>Height: 0.68 mm<br>Pitch: 1.14 mm<br>Tracks per layer: 42<br>Layer width: 48.64 mm<br>Process Parameters:<br>Laser Power: 1000 W<br>Deposition Speed: 10 mm/s<br>Translation Speed: 50 mm/s<br>Waiting Time per Layer: 15 s</td>
</tr>
<tr>
<td>Register</td>
<td colspan="2">





</td>
</tr>
</table>

## Finite Element Model

The development of a 3D FEM model is an essential step in accurately simulating complex structures. In this study, a hexahedral element-based FE model was created with a total of 49355 elements and 60396 nodes, as shown in Figure 47. A coarser and irregular mesh scheme was employed for the substrate to reduce the number of elements without compromising accuracy. However, a uniform and fine mesh size of 1.14 mm × 1.14 mm × 0.68 mm was generated for layers and areas of interest on the substrate after conducting a mesh sensitivity analysis.

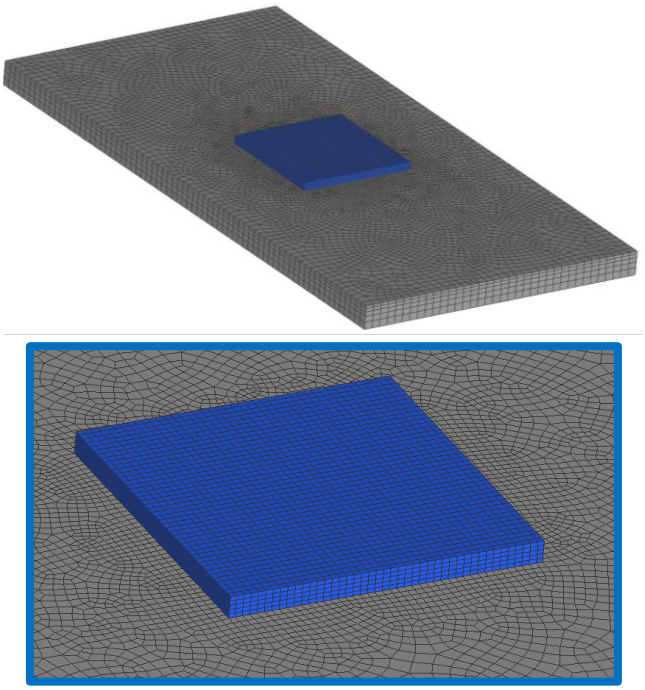


*Figure 47: FEM model with uniform mesh on layers and nonuniform mesh on the substrate.*

Directed Energy Deposition (DED) involves multi-layer welding with numerous individual robot movements, each of which must be represented as a trajectory in the simulation. To facilitate this, robot paths are imported from G-Code files, which provide movement coordinates, deposition speed, and laser alignment. Movements that do not contribute to material deposition are filtered out, while actual deposition trajectories are assigned a pre-defined heat source reflecting the corresponding welding speed.

The heat source models the energy distribution in the melt pool and is calibrated to experimental conditions through sensitivity analysis, ensuring that simulated temperature evolution, residual stresses, and distortions accurately reflect reality. This framework allows efficient and reliable simulation of complex DED processes, capturing both the sequential deposition and its thermo-mechanical effects.

### Calibration

The calibration of the heat source parameters was performed after a sensitivity analysis, correlating simulation results with experimental measurements. Key aspects considered during calibration included:

- Temperature Evolution**:** Comparison of simulated and experimental temperatures at the midpoint of the substrate.
- Distortion Analysis**:** Evaluation of total base plate distortion against experimental coupons.
- Computation Time**:** Assessment of full thermo-mechanical simulations versus the simplified ATC approach.

This process ensures that the heat source accurately reproduces thermal cycles, and deformations observed experimentally. The following figure illustrates the temperature evolution at the substrate midpoint obtained with different simulation approaches during parameter calibration.

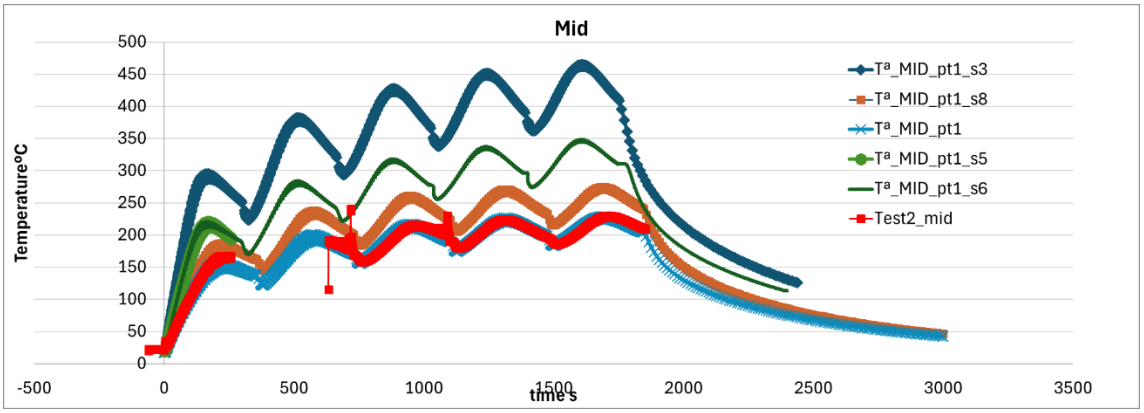



*Figure 48: Temperature evolution from different simulation iteration against experimental register plot.*

After calibration studies, the model parameters are correctly defined to obtain an accurate simulation response. As shown in the following graph. The mechanical behaviour was evaluated to the experimental coupon using the total distortion of the base plate

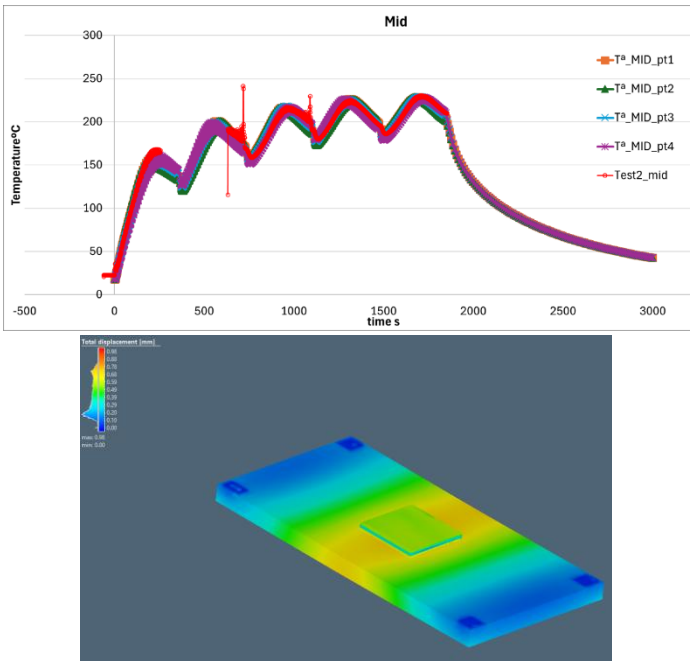



*Figure 49: Temperature evolution from simulation versus experimental register plot and total distortion field.*

The full thermomechanical simulation required approximately 34 hours of computation. To reduce calculation time, a simplification known as the Advanced Thermal Cycle (ATC)

method was evaluated. This approach allows multiple heat input increments to be applied simultaneously, significantly reducing computational cost while preserving the accuracy of thermal and mechanical results. The application time of the simplified load must be properly calibrated to ensure consistency. Using a more aggressive lumping simplification could reduce computation time to around 5 hours, but at the expense of resolution and accuracy.

Once the finite element model was adjusted and calibrated, studies were conducted to evaluate the effects of alternative manufacturing strategies on the deposition process. The resulting distortion fields on the base plate were compared, showing minor quantitative differences between strategies. Although these variations are limited, they indicate that at the demonstrator stage, path planning alone may not be sufficient to establish a decisive criterion for process optimization.

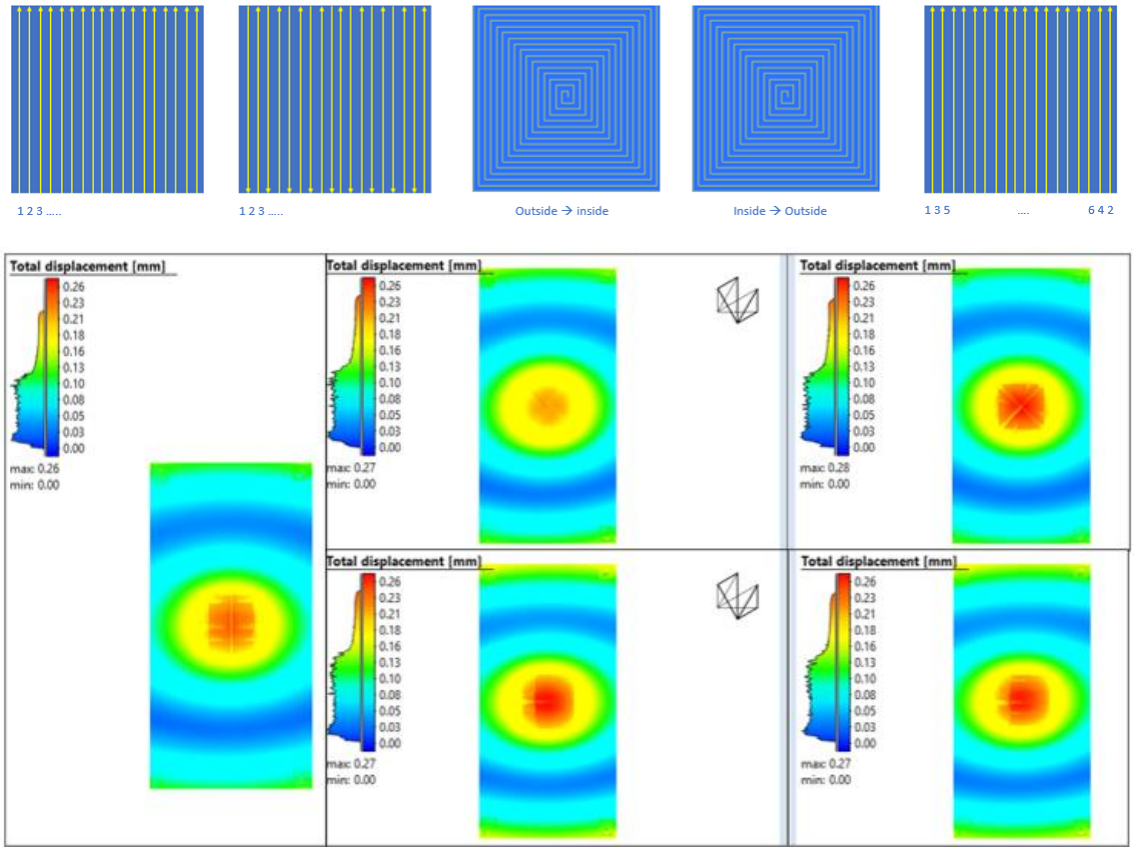



*Figure 50: (Top) Different strategies. (Bottom) Path planning distortion effects.*

The displacement evolution at the substrate midpoint further illustrates differences between deposition strategies. The maximum displacement does not occur at the same instant for all cases due to the varying waiting times between strands, which differ depending on whether a parallel or concentric deposition path is used.

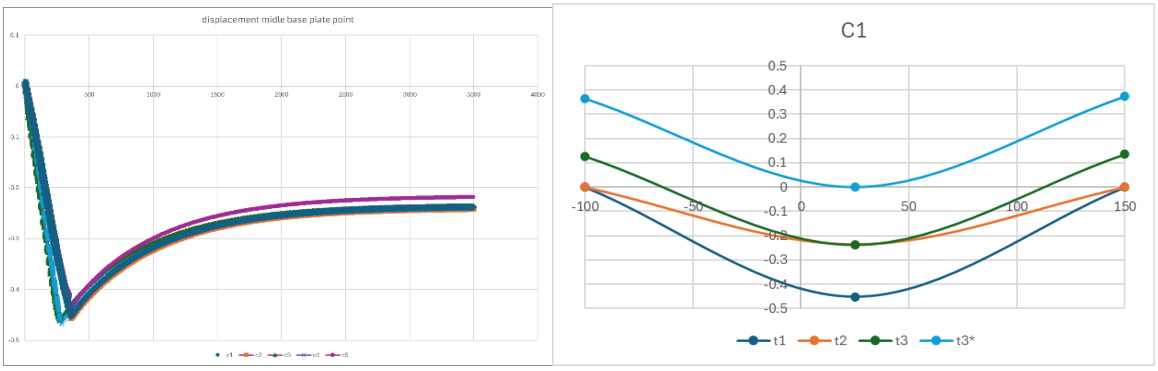



*Figure 51: Path planning distortion effects.*

To streamline post-processing, displacement values were extracted at three key points during the simulation of the manufacturing process: $t_1$, corresponding to the point of maximum displacement; $t_2$, after cooling; and $t_3$, after cooling and release of the fixation (unclamping). The unclamping was defined as the deactivation of the fixation boundary condition following cooling, with a small central area of the base plate maintained constrained to prevent unrestricted movement of the solid.

For direct comparison between cases, the displacement at $t_3$* is reported relative to the midpoint of the base plate. The plot below illustrates the displacement recorded after cooling and unclamping. The first set of values represents the total displacement, while the second set is relative to the midpoint. Differences between the plotted lines reflect the number of intermediate nodes used in the model to extract displacement data. The "z" line shows displacement values from individual intermediate points, whereas the $t_3$ line represents the displacement obtained by averaging the values from the three nodes.

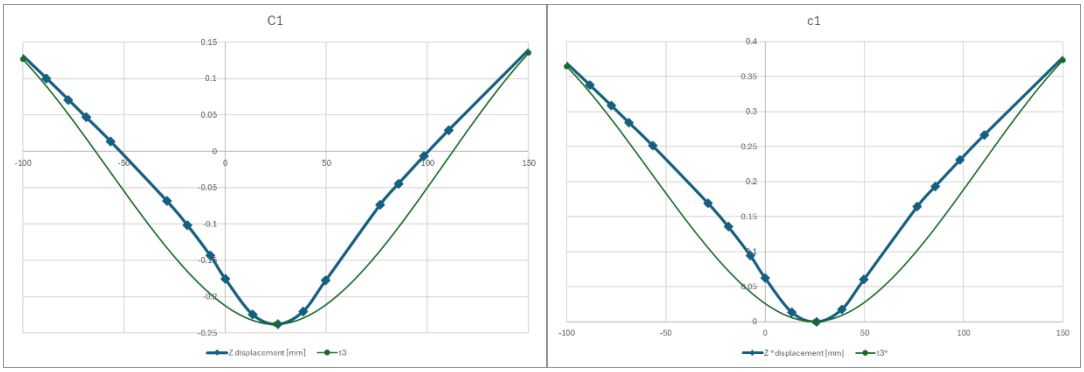



*Figure 52: Path planning distortion effects.*

## Conclusion and Next Research Direction

The analyses performed on the initial macro-scale models indicate that, although some distortion effects are observed, their magnitude is very limited. More importantly, these models do not provide sufficient resolution to capture localized phenomena such as stress concentration. This suggests that the critical issues in DED processes are not

related to macro-scale residual stresses, but rather to material behaviour during cooling, including potential embrittlement. Consequently, the current macro-scale models are not suitable for fully assessing these effects.

Based on these observations, a new research direction has been defined: to investigate whether macro-scale FEM models can detect variations in heat evacuation at the demonstrator level and assess the feasibility of linking thermal evolution to material behaviour. The simplifications applied in the initial models, including coarse mesh discretization and approximate heat source representation, do not account for metallurgical transformations or fine temperature gradients near the melt pool. Nevertheless, exploring the limits of these models may allow establishing correlations between thermal history and material hardening. This will involve calibrating the heat source and conducting comparative studies on experimental cases exhibiting varying hardness levels, indicative of local embrittlement.

First Step: Pure Thermal Model Demonstrator

As an initial approach within this new research line, a pure thermal model was developed to evaluate different scanning strategies at the demonstrator scale. Despite the large dimensions of the substrate, which acts as a substantial heat sink, noticeable differences in thermal evolution were observed depending on the deposition strategy. These differences highlight the influence of toolpath planning on local heat distribution and cooling rates, even under conditions of rapid heat dissipation.

### Thermal Analysis at Demonstrator Level

Thermal simulations were performed on two different massive substrate geometries, representing crankshaft mock-ups. Due to the high thermal mass of the substrate, heat generated during deposition is dissipated rapidly, strongly attenuating temperature gradients at the component scale. As a result, macro-scale thermal effects extracted from these models are minimal. Minor variations in thermal evolution are observable throughout the manufacturing sequence, but they are insufficient to produce a significant or clearly distinguishable effect at the global scale.

However, the temperature maps for different manufacturing strategies show consistent, repeatable differences in local thermal histories, despite the dominance of rapid heat evacuation by the substrate. These results indicate that, while the overall thermal response is strongly influenced by the substrate, local temperature evolution is still affected by process parameters and toolpath definition. Such observations provide a strong basis for further investigation, particularly to explore whether these local thermal variations can be linked to material hardening and embrittlement through a refined modelling approach.



*Figure 53: Large crankshaft mock-up works as a significant heat sink.*

The initial objective of this work was to evaluate, at a macro scale, the thermal effects induced by a Directed Energy Deposition (DED) process applied to crankshaft mock-ups. For this purpose, a finite element (FEM) simulation framework was performed whit the full component geometry and realistic boundary conditions. The first notable observation from these simulations is the highly massive nature of the substrates. Due to their large thermal mass, heat generated during deposition is dissipated very rapidly, strongly attenuating temperature gradients at the component scale. As a result, macro-scale thermal effects extracted from these models are minimal. Although minor variations in thermal evolution can be observed throughout the manufacturing sequence, they are insufficient to produce a significant or clearly distinguishable effect at the global scale.

Temperature maps generated for different scanning strategies, and for two massive substrate geometries, show that despite the dominant role of the substrate as a heat sink, local thermal histories vary consistently depending on the deposition path. These results highlight the influence of process parameters and toolpath definition on local temperature evolution, even under conditions of rapid heat evacuation.

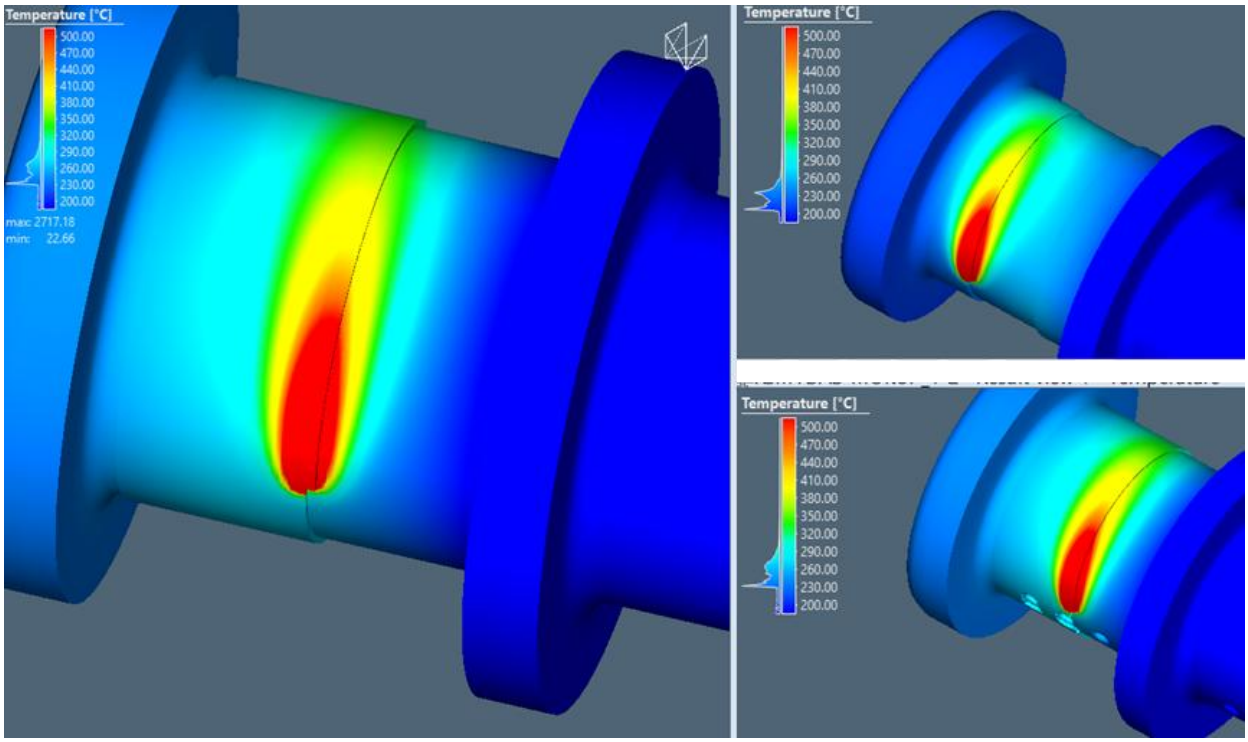



*Figure 54: Thermal evolution using different path planning.*

However, it should be noted that the current macro-scale FEM models are limited to thermal analysis and do not capture metallurgical transformations, phase changes, or the initiation and propagation of cracks. Consequently, these models cannot directly predict material hardening, embrittlement, or cracking phenomena, preventing a straightforward correlation between the simulated macro-scale thermal fields and the experimentally observed material response.

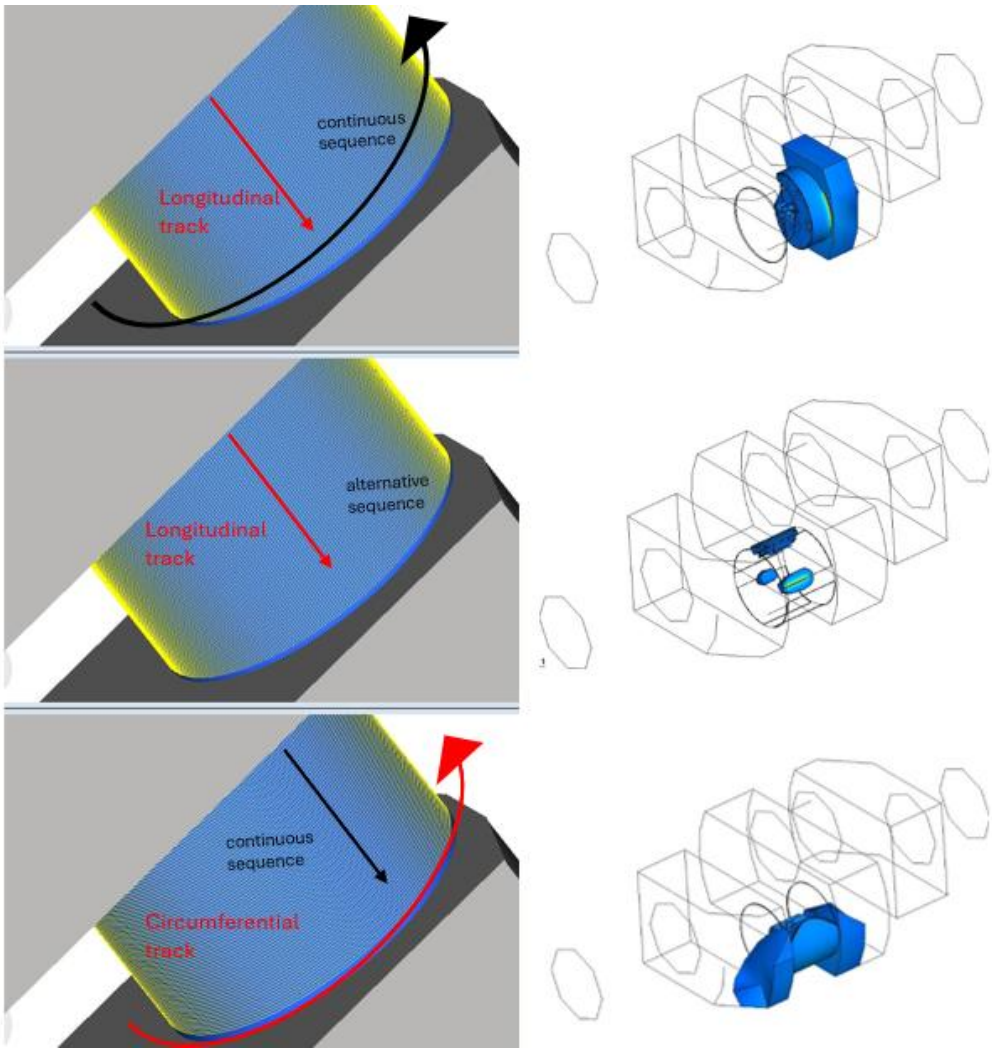



*Figure 55: Thermal evolution using different path planning.*

Based on these observations, the next step of this work is to establish a criterion for evaluating the thermal evolution maps obtained from the macro-scale simulations and to explore whether these thermal indicators can be correlated with material behaviour using experimental evidence. Although this approach extends beyond the conventional scope of macro-scale thermal modelling, the objective is to determine the limits of this methodology before transitioning to a finer modelling scale.

To achieve this and building on the results of Design of Experiments section a subset of manufacturing parameter combinations will be selected, along with their corresponding hardness measurements, both with and without substrate preheating. These cases will then be simulated using a refined single-track modelling approach. By reducing the simulation scale, the goal is to capture local thermal cycles with higher fidelity and assess whether the observed thermal effects can be meaningfully linked to material embrittlement and variations in hardness.

This multi-scale strategy is therefore proposed as an alternative modelling pathway, allowing the limitations of the macro-scale approach to be addressed while maintaining consistency with the experimental observations.

### Limitations and Next Steps

The current macro-scale FEM models do not account for metallurgical transformations or predict cracking phenomena. Consequently, the next step focuses on establishing a criterion to evaluate the thermal evolution maps generated by these models and exploring whether they can be correlated with material response using experimental data. Although this extends beyond the conventional scope of macro-scale modelling, the objective is to assess the limits of this methodology before transitioning to a finer modelling scale.

### Thermal–material response correlation study

Based on the results of the Design of Experiments (DoE) a subset of manufacturing parameter combinations will be selected along with their corresponding hardness measurements, both with and without substrate preheating. These cases will then be simulated using a refined single-track modelling approach, allowing local thermal cycles to be captured with higher fidelity. The aim is to investigate whether the observed thermal effects can be meaningfully related to material embrittlement and variations in hardness, thereby establishing a link between process parameters, thermal history, and material response at a more local scale.

*Table 14: Process parameters for thermal material study.*

| Condition | Pre-Heating °C | Laser Power W | Powder feed rate g/min | Process speed mm/s | ID |
|---|---|---|---|---|---|
| **1** | None | 1500 | 10 | 10 | 1 |
| **2** | None | 1500 | 20 | 20 | 9 |
| **3** | None | 3500 | 10 | 10 | 19 |
| **4** | None | 3500 | 20 | 20 | 27 |
| **1** | 300 | 1500 | 10 | 10 | 55 |
| **2** | 300 | 1500 | 20 | 20 | 63 |
| **3** | 300 | 3500 | 10 | 10 | 73 |
| **4** | 300 | 3500 | 20 | 20 | 81 |

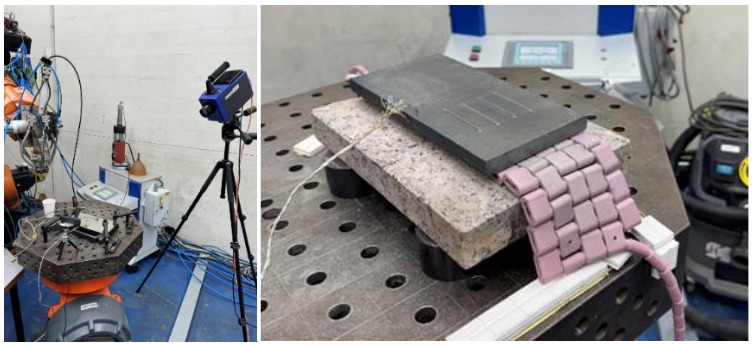


*Figure 56: Experimental Set up.*

### Hardness Study and Correlation with Thermal Behaviour

The hardness measurements (Figure 57) clearly indicate that, in the absence of substrate preheating, strengthening occurs within the Heat-Affected Zone (HAZ). Among all the tested conditions, the most favourable results were obtained for the track manufactured under Preheat Condition 3 (ID 73), targeting a hardness of 421 HV. This condition exhibited the lowest hardness values and corresponded with the sample with high energy density.

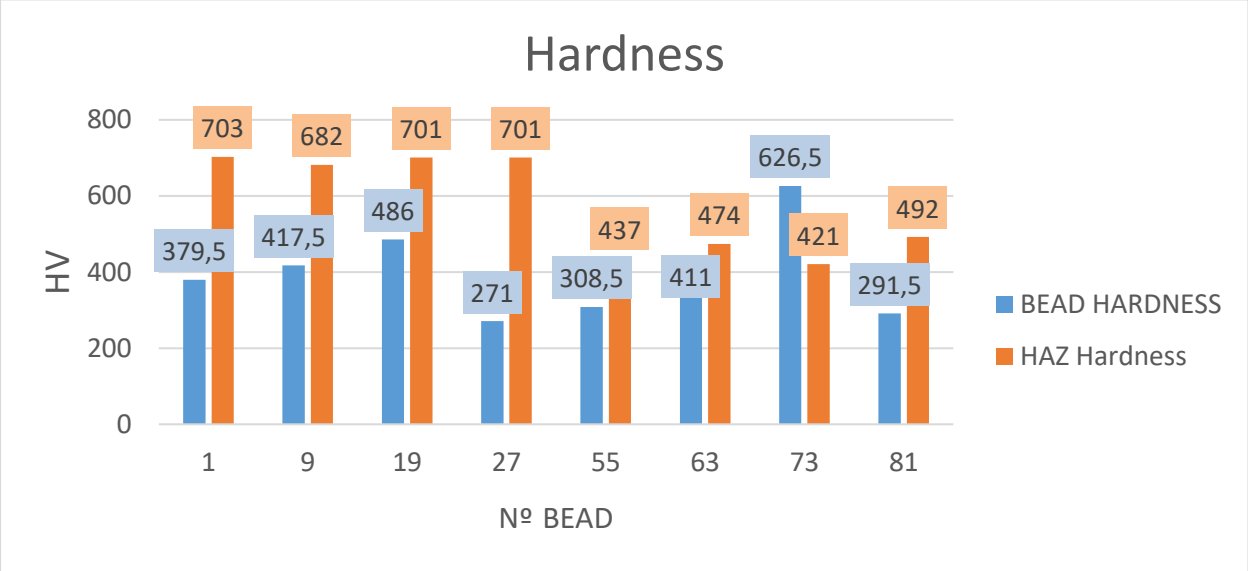



*Figure 57: Tracks hardness.*

The aim of this analysis is to evaluate the cooling rate for the lowest value of hardness with preheating. This allows us to analyse the cooling rate needed to have a low value of hardness in the HAZ. To do that a correlation process is needed.

### Simulation and Experimental Correlation

Finite element simulations were performed to correlate thermal evolution with experimental hardness results.

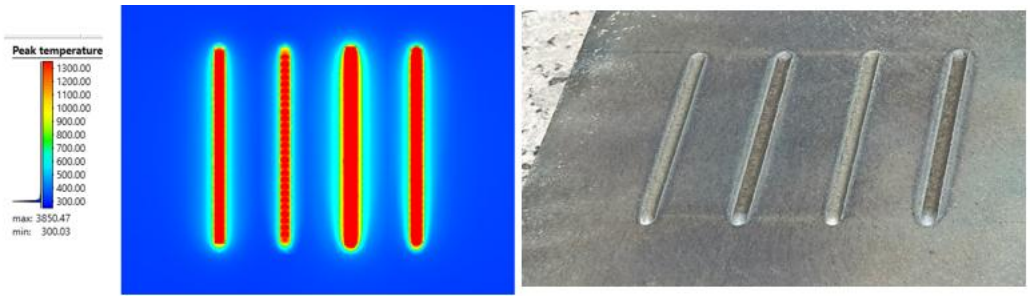



*Figure 58: HAZ Simulation vs experimental.*

Comparisons between macrographs of the experimental tracks and simulated peak temperature distributions show promising qualitative agreement. Although the macro-scale FEM model does not compute metallurgical transformations or crack formation, it provides valuable insights into thermal behaviour. The track manufactured under Preheat Condition 4 (ID 73, hardness target 421 HV) was selected as a reference case due to its optimal and uniform hardness profile and the absence of cracks.

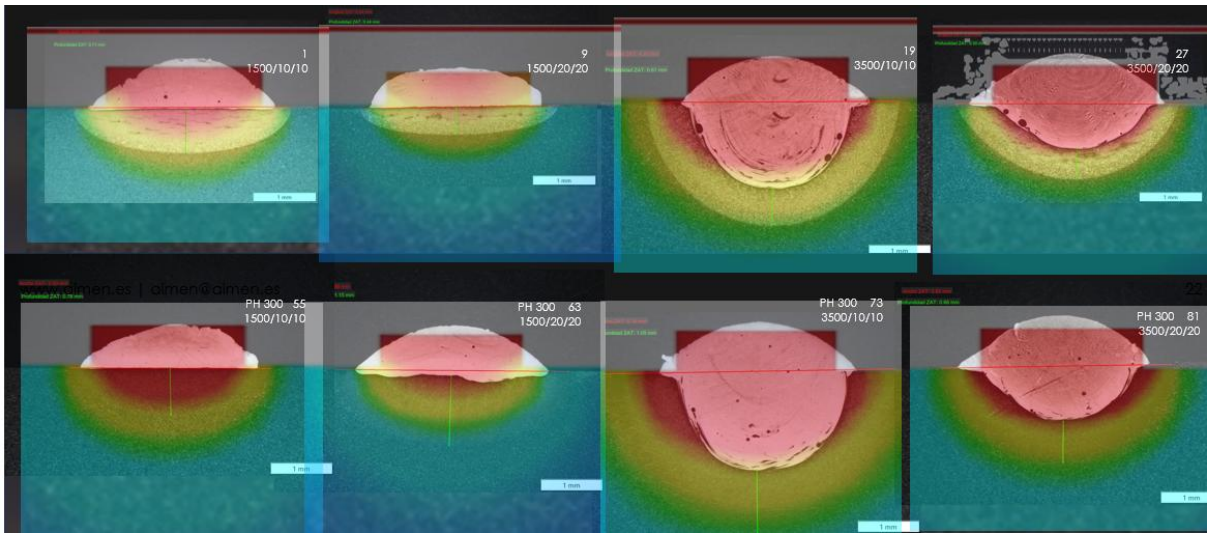



*Figure 59: Macrographic vs simulation HAZ.*

## Cooling Rate Analysis

As a first approach, nodal temperature values were extracted from the HAZ region to estimate cooling rates. Using the reference track (Condition 4) as a baseline, similar evaluations were conducted for other tracks. In Figure 60 the plot shows the lowest cooling rate for ID 73 (grey colour), that is related with lowest value of hardness and the absence of cracks.

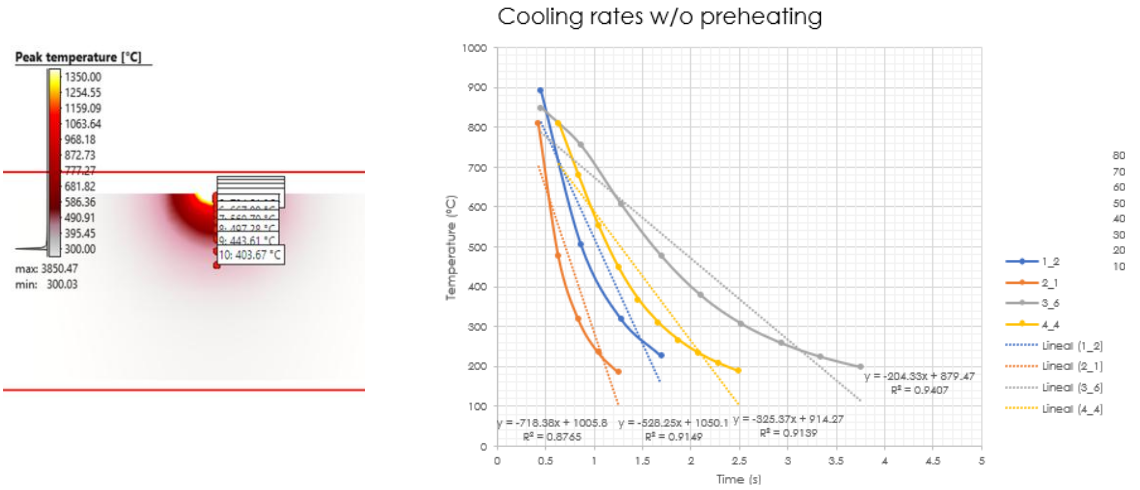



*Figure 60: Cooling rates extracted from macro approach simulation.*

### The results reveal a clear trend:

Hardness measurements do not show a significant decrease according to the experimental data. However, the absence of cracking may indicate a reduction in brittleness, which is commonly associated with a decrease in hardness or residual stresses

The correlation between cooling rate and hardness is consistent across cases, with the best non-preheated option showing a cooling rate (Figure 60) close to the reference (170°C/s), albeit slightly higher.

This preliminary correlation suggests that cooling rate could serve as an indirect indicator of hardness and embrittlement risk at the macro scale, even though the model does not capture microstructural changes.

### Observations and Limitations

The standard macro simulation approach is not sufficient in this case, while providing valuable insights into global thermal behaviour, lacks the resolution to predict metallurgical transformations or crack formation. However, the macro simulation approach does provide information about the cooling rate, which is a key factor for predicting material behaviour.

Cooling rate is strongly linked to hardness and embrittlement risk, making it a useful indicator at the macro scale.

Hardness study results suggest that a well-controlled DED-LB/M process can reduce thermal gradients and ensure more consistent material properties.

This reinforces the importance of thermal management strategies such as preheating.

The cooling rate between 800 °C and 400 °C was evaluated in the “ideal” case (Preheat Condition 4) and taken as a reference for comparison with other conditions.

Between all the tested conditions, as previously explained in DOE section, the hardness is only affected in the HAZ by the preheating temperature. Nevertheless, the condition 3 (ID19), despite the fact keep a high hardness, do not present cracks in the HAZ (see Figure 43). This indicated that the other factors such as power, speed and powder flow can affect the microstructural integrity in the HAZ.

### Perspectives

The next stage of the research will use cooling rate data from the macro-scale thermal model to predict material properties. Although microstructural changes are not directly modelled, this approach may allow establishing a correlation between thermal evolution and experimentally observed hardness trends. The planned activities include:

- Extending the analysis to additional tracks with and without preheating.
- Comparing cooling rates extracted from simulations with experimental hardness measurements.
- Defining a preliminary criterion for property prediction based on thermal indicators, using cooling rate as a macro-scale proxy for embrittlement risk.

## 3.3 Manufacturability tests

Within the Manufacturability test, a dedicated mock-up with a geometry representative of the final crankshaft (Figure 61) was designed and manufactured. This model was also used for other trials (See simulation and path-planning section).

In a first stage, different process parameters were tested in order to assess their influence on the mechanical properties and the overall integrity of the deposited coating. Subsequently, several tilting angles and process parameters for drill holes, were evaluated to identify potential adverse effects of the process kinematics on the quality and consistency of the coating.

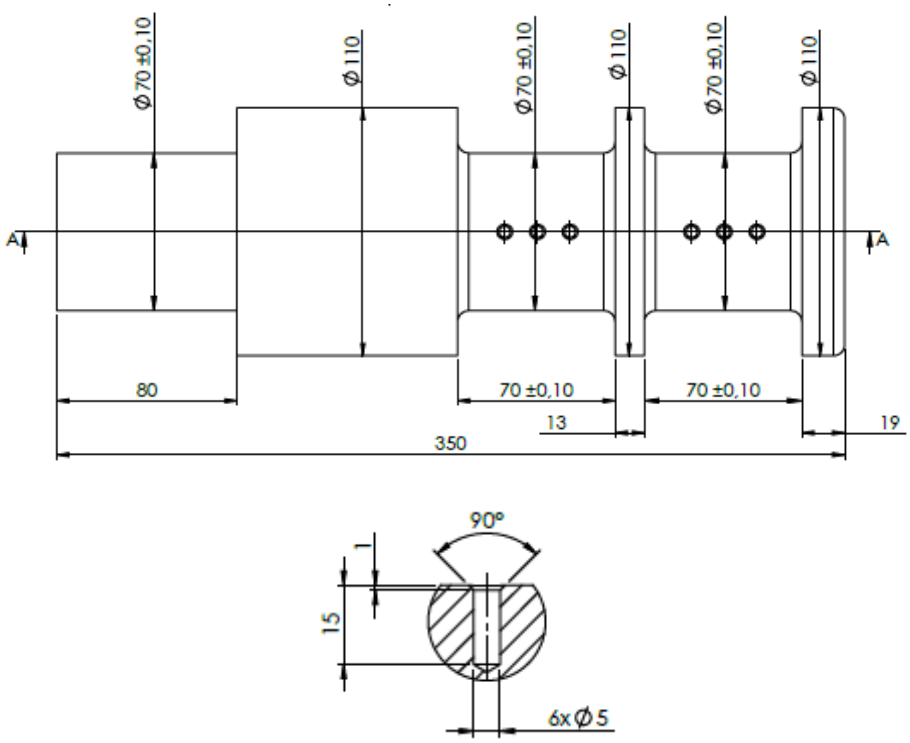



*Figure 61: Detailed drawing of the Mock-up geometry.*

### Process parameters

For the process parameters assessment, different combinations of laser power, scanning speed and track overlap were systematically tested to identify significant variations attributable both to the selected parameters themselves and to the remelting phenomena occurring during the deposition process.

The objective is to evaluate whether the heat accumulation induced by prolonged cladding operations had a measurable impact on the integrity of the deposited material, as well as on the hardness of both the coating and the HAZ.

*Table 15: Process parameters tested on different mock-up´s, tiling angle 20°.*

| | **Power (W)** | **Speed (mm/s)** | **Stepover 55% (mm)** |
|---|---|---|---|
| **A1** | 1500 | 20 | 1.43 |
| **A2** | 2500 | 15 | 1.54 |
| **B1 (PREHEAT 150ºC)** | 1500 | 10 | 1.43 |
| **B2** | 3500 | 10 | 1.59 |

### Section-A1

This section aims to analyse the results for **low density energy** parameters on the mock up. Show low dilution on the base material and a small HAZ. The homogeneity of the cladded material is good enough except in the fillet where exist variations in the cladding height. Near the drill hole there is a discontinuity in the cladded surface due to the lack of alignment. See Figure 62.

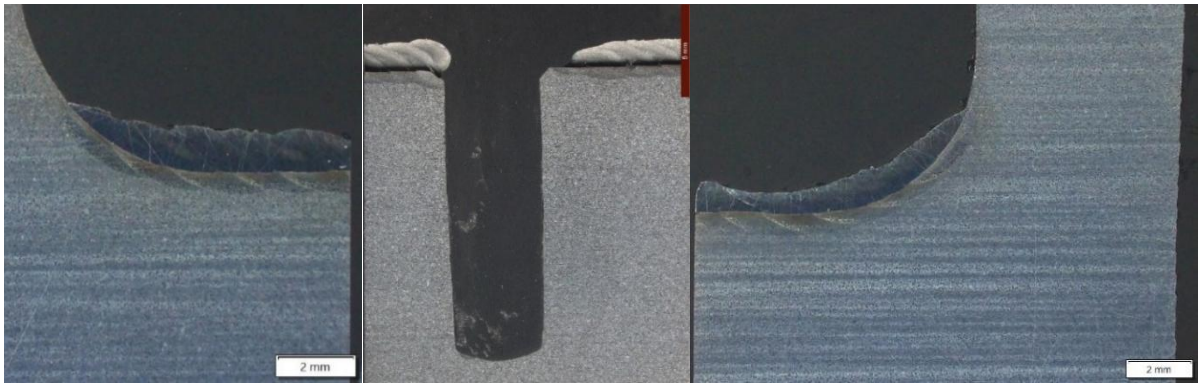



*Figure 62: Macrograpy´s for A1 condition. Start from right to left.*

### Section-A2

The section A2 was manufactured using **high density energy** parameters. The main difference compared to the previous one is the higher dilution rate and the presence of cracks in the last fillet. Also, there is solid particle inside the hole probably caused by the high power that fuse the powder even at higher distances.

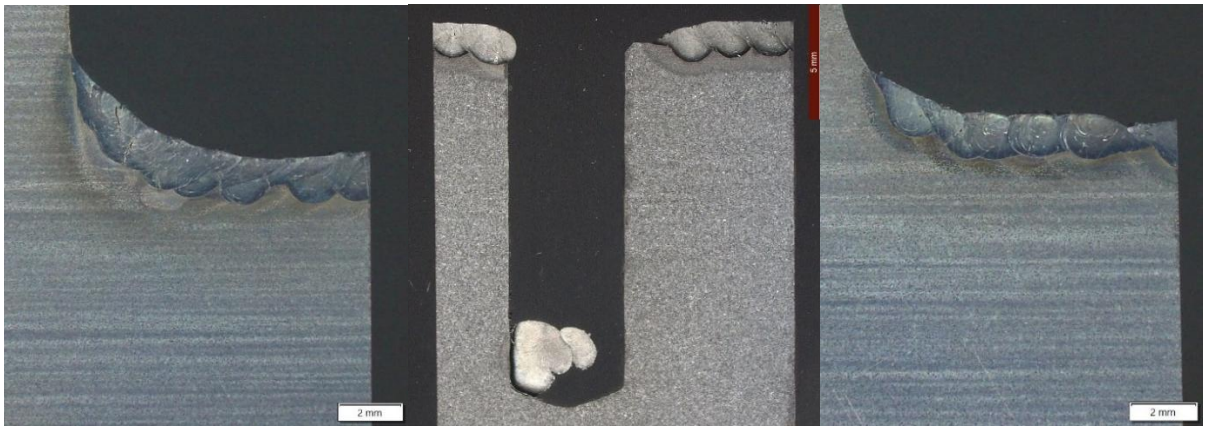



*Figure 63: Macrography for A2 condition. Start from right to left.*

### Section-B1

The section B1 show the results for a cladding with **low energy density assisted with preheating temperature**. The initial fillet shows good homogeneity compared to the last fillet which present an irregular aspect due to the high overlap between tracks induced by the shielding of the previously deposited track by the following pass. Remark the absence of cracks in the fillets and the cladding.

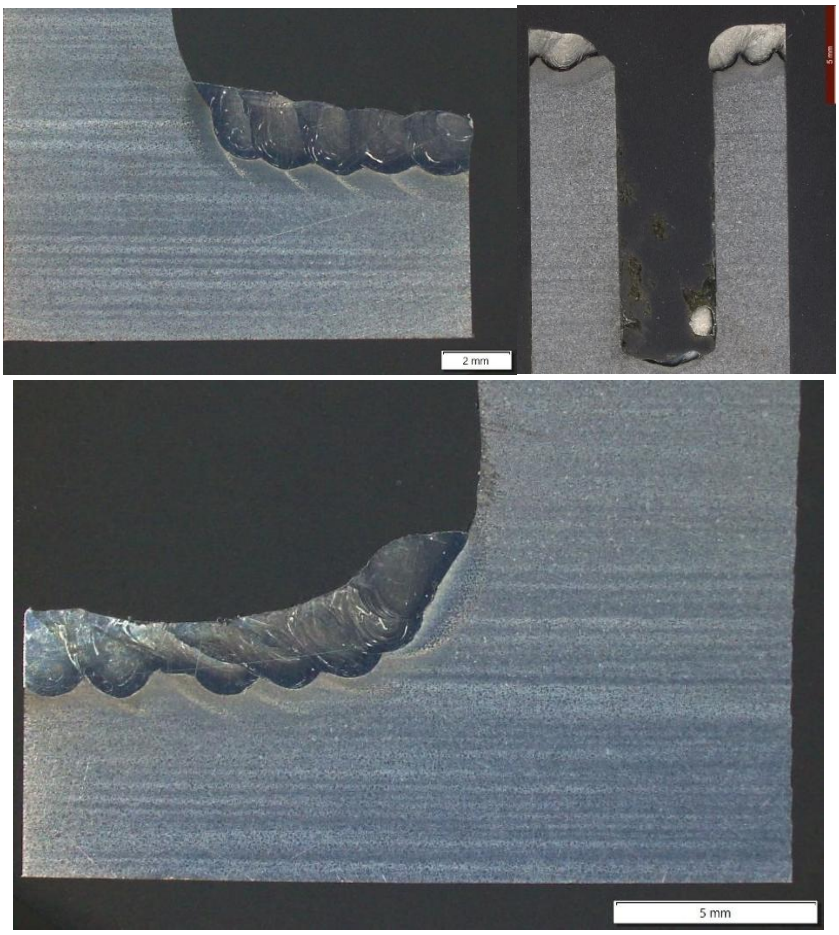



*Figure 64: Macrography´s for B1 condition. Start from top left.*

### Section-B2

The section B2 was made with the highest value of power (3500W) and with the lowest speed. This is translated into high height. The integrity of the cladded material around the holes is good. This can be explained by the difference in the stepover that provoke an alignment with the holes. In the first fillet a solidification crack occurs. Nevertheless. The last fillet presents some irregularities caused by the change in the tilting angle to avoid collision.

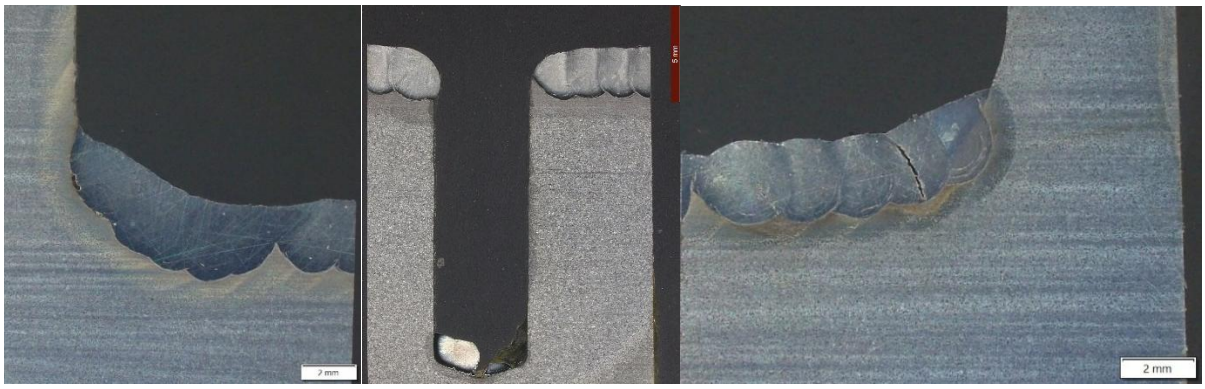


*Figure 65: Macrography´s B2 condition. Start from right to left.*

### Tilting angle and parameters for drill holes

After evaluating the process parameters on the mock-up geometry. We have performed different trials considering, different tilting angles for the fillets and process parameters for the holes.

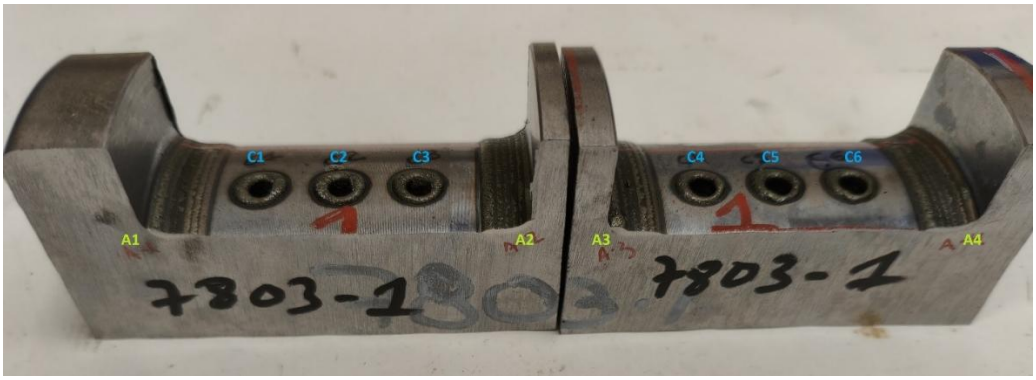



*Figure 66: Mock-up with the reference scheme indicating the position of each drill hole and the fillet allocation.*

The reference scheme is show in Figure 66 where it is shown the allocation of each hole and the fillets.

The process conditions (Table 16) selected pretend to avoid heat accumulation in the small area around the hole, which can produce over deposition and fuse the edge.

*Table 16: Process parameters for holes.*

| | C1 | C2 | C3 | C4 | C5 | C6 |
|---|---|---|---|---|---|---|
| **Power** | 1500 | 1500 | 1200 | 1000 | 1200 | 1000 |
| **Speed** | 15 | 15 | 15 | 15 | 20 | 20 |

The macro analysis (Figure 67) reveals good edge cladding, maintaining it without fuse. Although the width/height ratio seems adequate on one side, the cross-section on the

opposite side is unsatisfactory. Probably it can be due to the poor wettability of the melt pool at low power, when the process starts. Being solving at the end due to the heat accumulation. All the conditions present low dilution rates and smalls HAZ´s. This is necessary to avoid modifications in the edge.

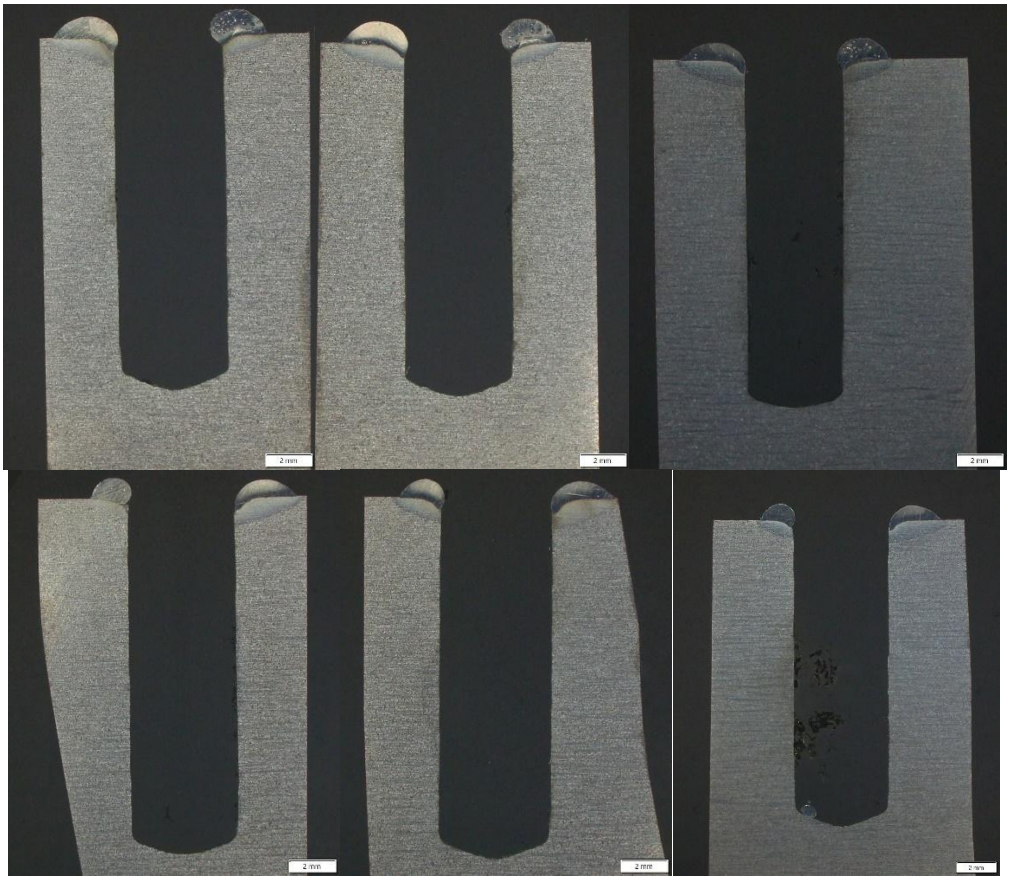


*Figure 67: Macrography´s of cylinders cross section. (Top) Left to right A, B and C. (Bottom) Left to right D, E and F.*

After evaluating the process parameters, the analysis shifted to the effect of the tilting angle. Subsequently, a trial was conducted testing different orientations of the deposition head to determine whether a change in the tilting angle could induce discontinuities in the deposited material. The tilting angles evaluated are presented in Table 17, while the process parameters kept constant (1500W and 20 mm/s) throughout the test to isolate the effect of the inclination.

*Table 17: Tilting angle conditions.*

| | **Tilting angle (°)** |
|---|---|
| **Condition 1** | 18.5 |
| **Condition 2** | 22 |

Figure 68 shows the deposited material in the initial fillet, when the process starts. Macrography's indicates good integrity with low ratios of dilution due to the process parameters. Related to the angles there is no difference between both conditions.

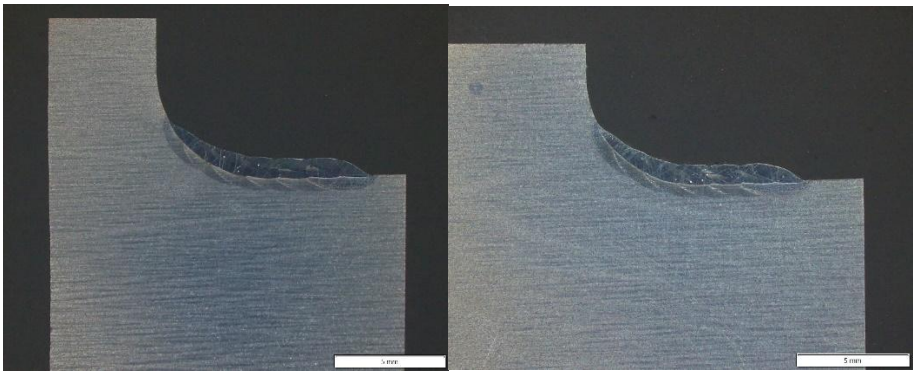


*Figure 68: Initial fillet macrography's. (Left) Condition 2. (Right) Condition 1.*

Figure 69 present similar results for the final fillet having the characteristic re-melting zone due to the shielding effect mention in previous section.

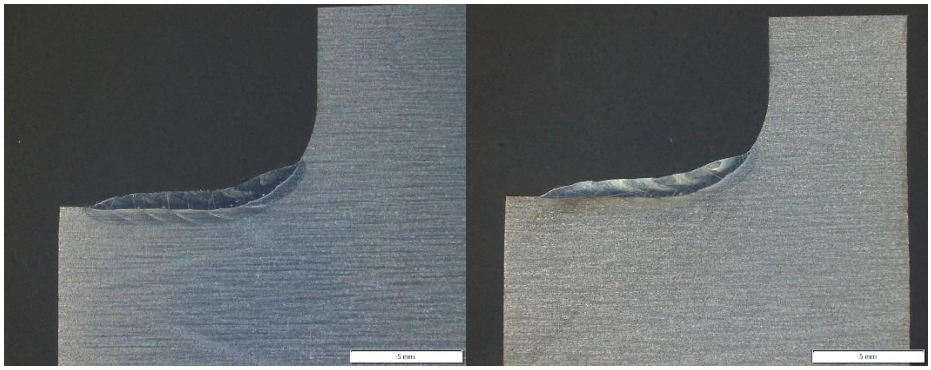


*Figure 69: Final fillet macrography's (Left) Condition 2 (Right) Condition 1.*

This analysis concludes that small variations in the tilting angle does not affect the continuity in the deposited material neither the microstructure.

## 3.4 Material substitution analysis

This section presents an analysis aimed at replacing the current cobalt-based cladding material with a more sustainable iron-based alternative. The motivation for this substitution is supported by from task T5.2 activities (Figure 70 and deliverable D5.2), which indicate a lower environmental impact for iron-based alloys compared to cobalt-based ones. At present, the cladding material used is Stellite 21, and the proposed replacement is a chromium-alloyed iron-based material called Ferro55.

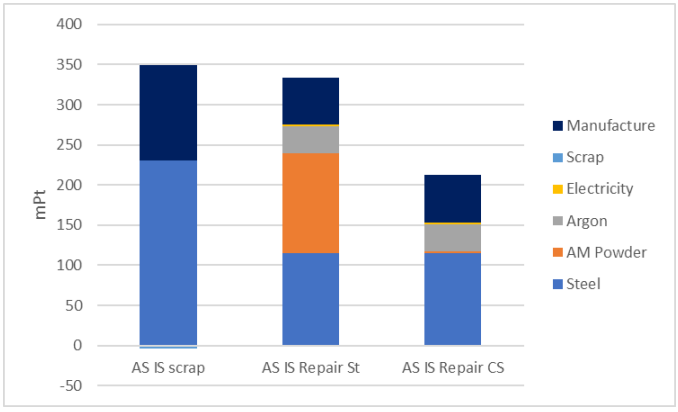



*Figure 70: Milipoints plot for repairing process sing Stellite 21 (As is repair ST) and Ferro55 (As is repair CS).*

To evaluate the feasibility of this change, pin-on-disk wear tests have been conducted to compare the wear resistance and tribological behaviour of both materials under equivalent testing conditions.

## 3.4.1 Wear properties

Prior to the tribological evaluation, a preliminary hardness characterization was carried out for both materials in order to establish a reference for their mechanical response and a first idea about the wear behaviour, considering Archard equation $w \propto 1/Hardness$ (Zhang et al., 2024).

*Table 18: Hardness value HV10 for Stellite 21 and Ferro 55.*

| Material | Hardness HV10 |
|---|---|
| **Stellite 21 (ID53)** | 380 |
| **Ferro55 (ID29)** | 572 |

Subsequently, a series of pin-on-disk wear test were performed under different boundary conditions. Two testing conditions were defined: one involving a lower load (5N) with a longer sliding distance (100M), and a second condition with a higher applied load (30N) and short distance (100m). this is considered because the friction coefficient is not an intrinsic material property, as it depends on the testing conditions.

*Table 19: Boundary conditions for pin on disk tests (Low load condition).*

| | | | |
|---|---|---|---|
| **Radious path (mm)** | 5 | **Material pin** | Al2O3 |
| **Load (N)** | **5** | **Pin diameter (mm)** | 4 |
| **Speed (RPM)** | 50 | **Distance (m)** | **1000** |

The first results analysed correspond to the optical images of the worn surfaces and the associated wear curves. In sample 53, a highly irregular steady-state region is observed, characterized by large oscillations during the steady-state regime. These fluctuations are not correlated with a particularly irregular surface morphology; on the contrary, the surface appears relatively homogeneous. According to the literature, such behaviour may be attributed to vibrations in the experimental setup or similar external instabilities, as debris formation or particle entrapment is not expected to induce oscillations of this magnitude under steady-state conditions.

This phenomenon is also presented in the literature as *Stick-slip* motion. The forces doesn´t remain constant along the experiment and can occur if the coefficient of static friction is greater than the coefficient of kinetic friction. (Nosonovsky et al., 2013)

In contrast, sample 29 exhibits surface features such as oxide-related mounds or valleys, which could potentially lead to irregularities in the wear curve. Nevertheless, the corresponding wear curve remains notably stable throughout the test.

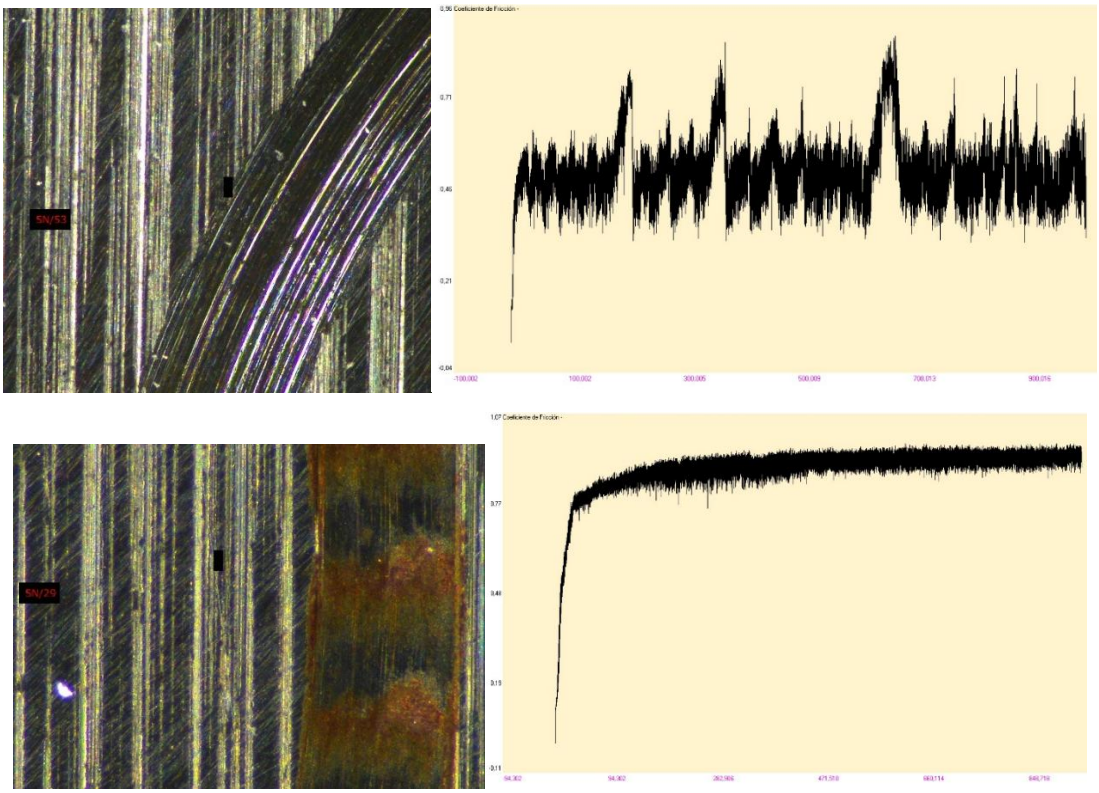



*Figure 71: Low load conditions (Top Left) Wear surface analysis test for Stellite 21 and (Top Right) Friction coefficient versus distance plot. (Bottom Left) Wear surface analysis test for Ferro55 and Bottom Right) Friction coefficient versus distance plot.*

Having presented the results for the low load conditions, the following section present the results for high load condition.

As in the case above the Stellite 21 presents an irregular variation of the friction coefficient. This indicates possible issues during the assay like vibrations due the dry

conditions. In addition, in any case the Stellite 21 does not presents oxide formation due to high temperatures during the experiment while Ferro55 presents.

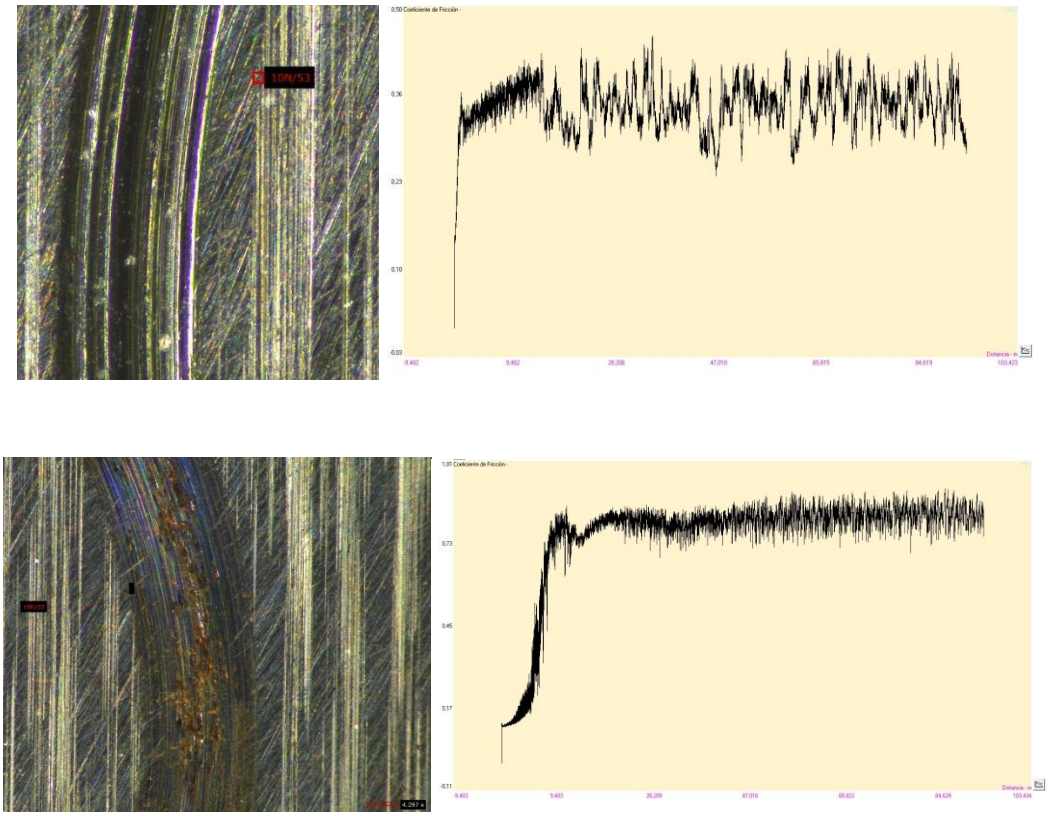


*Figure 72: High load conditions (Top Left) Wear surface analysis test for Stellite 21 and (Top Right) Friction coefficient versus distance plot. (Bottom Left) Wear surface analysis test for Ferro55 and (Bottom Right) Friction coefficient versus distance plot.*

Regarding the wear results, under low load conditions (5N) the highest wear was observed for Stellite21 material with a wear value of 1.31E-04, which also exhibits the highest coefficient of friction. In contrast, under high-load conditions the maximum wear correspond to Ferro55 with a wear value of 9.70E-05, associated with a coefficient of friction of 0.86. In both loading regimes a clear correlation is observed between higher wear and higher coefficients of friction. These differences in the coefficients of friction are unexpected, as both materials exhibit comparable surface roughness resulting from the same surface preparation and manufacturing procedure, as is well known that a high surface roughness increase the friction coefficient (Nosonovsky et al., 2013).

In addition, it is expected that the friction coefficient increases with the load (Nosonovsky et al., 2013). Nevertheless, the difference between both materials increases drastically at high loads.

*Table 20: Pin-on-disk results for Stellite 21 and Ferro 55.*

| | | **Stellite21 (ID53)** | **Ferro55 (ID29)** |
|---|---|---|---|
| **Low load conditions** | Wear rate $mm^3/Nm$ | **1.31E-04** | 2.8E-05 |
| | Dynamic friction coeff | 0.14 | 0.11 |
| **High load conditions** | Wear rate $mm^3/Nm$ | 5.45E-05 | **9.79E-05** |
| | Dynamic friction coeff | 0.36 | 0.86 |

Ordinarily, the higher the surface hardness of a metal, the better its anti-wear performance. Nevertheless, the materials with high hardness, low strength and strong brittleness are easily develop the surface fatigue and abrasive wear in the process of heavy friction sliding (Zhang et al., 2024).

Following the discussion of the pin-on-disk results, a further characterization was carried out using scanning electron microscopy to examinate the worm surfaces in detail and identify the underlying mechanisms responsible for the observed differences in wear behaviour. This analysis aims to clarify the origin of the transition whereby Stellite21 exhibits higher wear under low load testing conditions, while the Ferro55 suffer higher wear at high load conditions.

The first SEM Figure 73 of Ferro55 shows a smooth surface without any ploughing. At higher magnification there are some irregularities that after analysis the conclusion is that they are ferrous oxides.

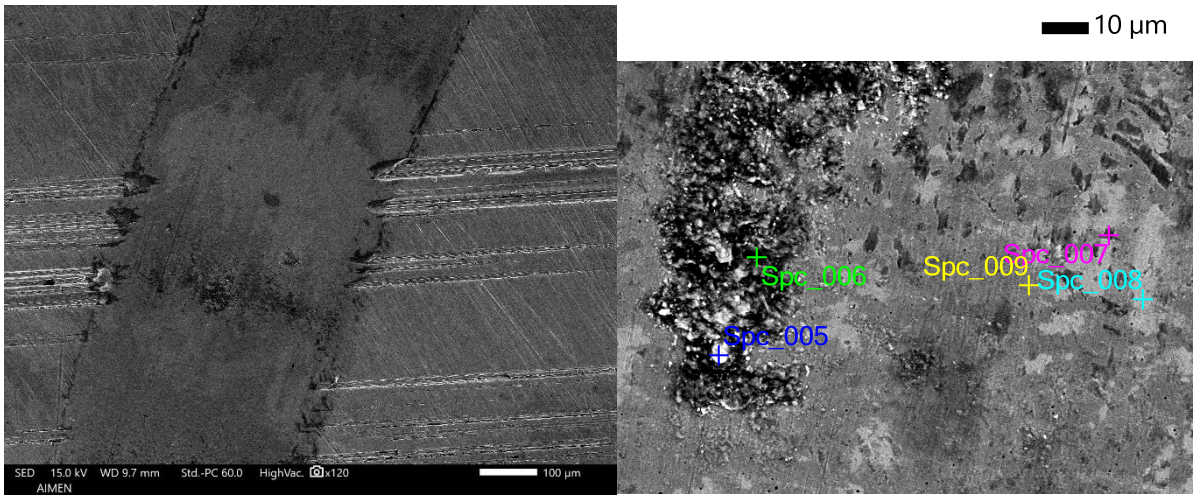



*Figure 73: SEM micrography´s Ferro55- 5N(Left)100x (Right) 1000x.*

The EDS results show the presence of ferrous oxides in the surface in the not-smooth areas.

*Table 21: EDS analysis for high magnificence image. Atom/Mol%.*

| Name | C | O | Si | K | Cr | Mn | Fe | Mo |
|---|---|---|---|---|---|---|---|---|
| **Spc_005** | 15.60 | 36.64 | 0.20 | 0.37 | 3.67 | 0.42 | 41.73 | 1.38 |
| **Spc_006** | 22.85 | 20.74 | 0.20 | 0.31 | 4.31 | 0.67 | 49.24 | 1.68 |
| **Spc_007** | 13.99 | 15.34 | 0.21 | 0.21 | 5.21 | 0.50 | 62.87 | 1.67 |
| **Spc_008** | 16.28 | 2.05 | 0.27 | | 6.02 | 0.67 | 72.64 | 2.07 |
| **Spc_009** | 16.48 | 4.48 | 0.26 | | 7.60 | 1.01 | 66.16 | 4.00 |
| **Standard** | 3.03 | 12.46 | 0.03 | 0.06 | 1.37 | 0.20 | 11.35 | 0.95 |

Regarding the high load condition (Figure 74), the surface appear to be more damage due to abrasive wear with the appearance of ploughing marks. The asperities of hard materials are pressed into the soft surface with plastic flow of the soft surface. The hard material will slide and remove the soft material by plowing. In the opposite side it seems the presence of some adhesive wear with material transferred.

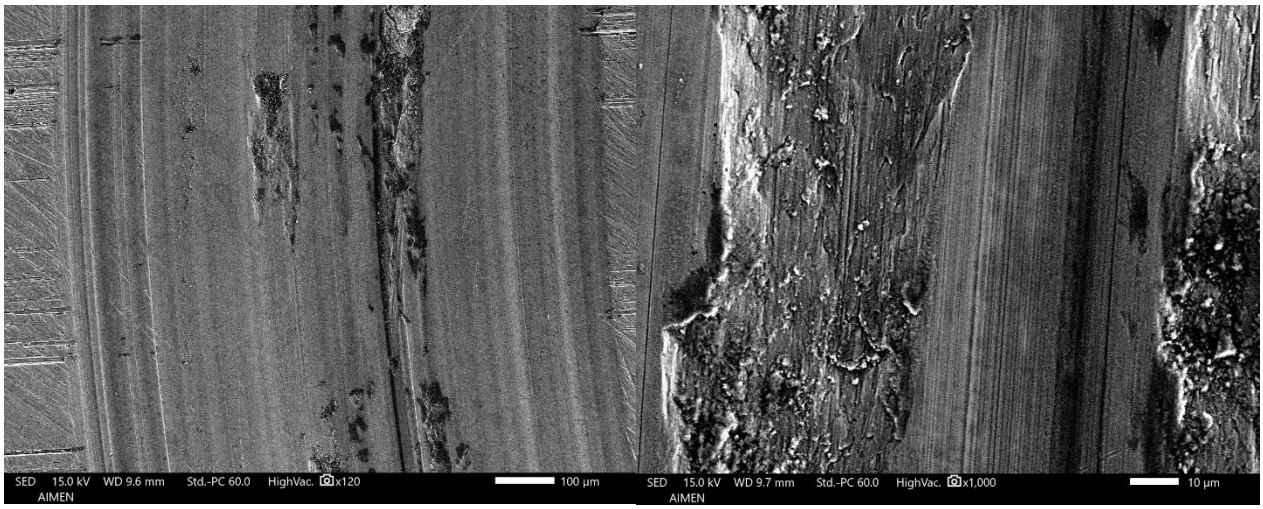



*Figure 74: SEM micrography's Ferro55- 30N(Left)100x (Right) 1000x.*

Moving to Stellite 21 under low-load conditions (Figure 75), the SEM analysis revealed that the material undergoes similar wear mechanisms to those observed in Ferro 55. The worn surface exhibits clear ploughing marks indicating abrasive wear, as well as evidence of adhesive wear. During continuous sliding, the adhesive marks are progressively deformed and smeared along the sliding direction.




*Figure 75: SEM micrography´s Stellite 21- 5N(Left)100x (Right) 1000x.*

The EDS analysis (Table 22) shows the presence of oxides in the transferred material. Probably caused by temperature accumulation due to high friction.

*Table 22: EDS analysis for high magnificence image. Atom/Mol%.*

| Name | C | O | Al | Si | K | Cr | Mn | Fe | Co | Mo |
|---|---|---|---|---|---|---|---|---|---|---|
| **Spc_006** | 2.91 | | | 0.84 | | 27.51 | 0.58 | 1.93 | 59.46 | 6.77 |
| **Spc_007** | 6.27 | 21.32 | 0.37 | 0.56 | 0.40 | 21.67 | | | 44.49 | 4.92 |
| **Standard Deviation** | 1.68 | | | 0.14 | | 2.92 | | | 7.49 | 0.93 |

Under high-load conditions (30N), the response of the material surface differs markedly from that observed at low load. The worn surface, in Figure 76, no longer exhibits prominent ploughing marks, suggesting a reduction in abrasive wear mechanisms or a transition to a different wear regime. Furthermore, no clear evidence of adhesive wear is observed, in contrast to the low-load condition where material transfer and smearing were evident. This change in surface morphology may indicate that the contact conditions promote a more severe deformation-driven mechanism, such as subsurface plastic deformation or oxidative wear, which can obscure the typical features of abrasive or adhesive wear. The absence of distinct ploughing and adhesive traces suggests a shift in the dominant wear process as the normal load increases.

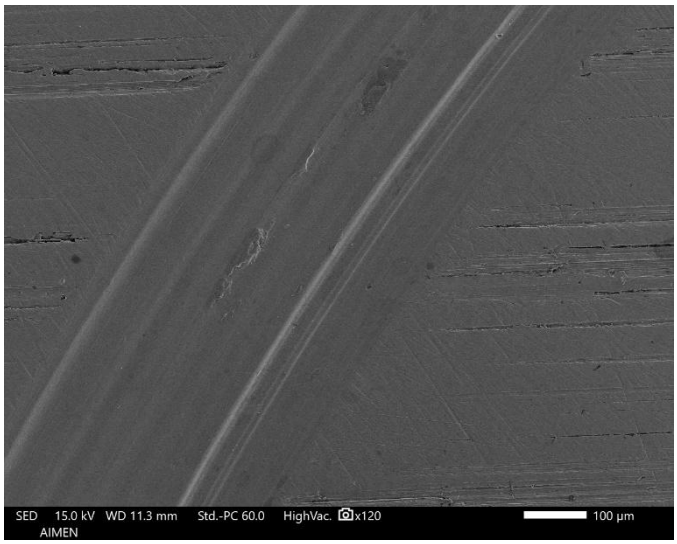



*Figure 76: Stellite 21 (30N) 100x.*

### 3.4.2 Mock-up tests with Ferro 55

After evaluating the wear properties of both materials, a mock-up was cladded using the proposed material Ferro 55. Two different sequences are studied to analyse the effect in the resulting shape in the cladded material and the presence of defects as pores, cracks or lack of fusions.

- Sequence 1: Cylinders + whole surface
- Sequence 2: Whole surface + Cylinders

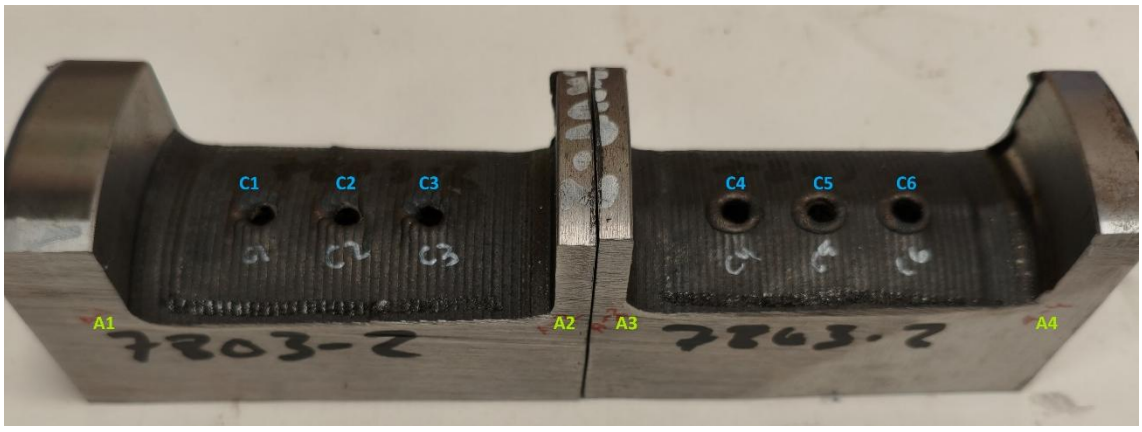



*Figure 77: Image of the Mock-up 2 cladded with Ferro 55 (Left) Sequence 1. (Right) Sequence 2.*

The parameters used for the test are listed below.

*Table 23: Process parameters for Mock-up 2.*

| | Power (W) | Powderflow (g/min) | Speed (mm/s) | Fillet speed (mm/s) | Laser head angle (°) | Stepover (mm) |
|---|---|---|---|---|---|---|
| **Sequence 1** | 1800 | 11 | 15 | **20** | 18.5 | **1.43** |
| **Sequence 2** | 1800 | 11 | 15 | **15** | 18.5 | **1.59** |

### Sequence 1

The macrographs for the first sequence show good quality with low ratios of dilution and a small area for the HAZ. Around the holes the clad continuity is enough to guarantee the material after the machining.

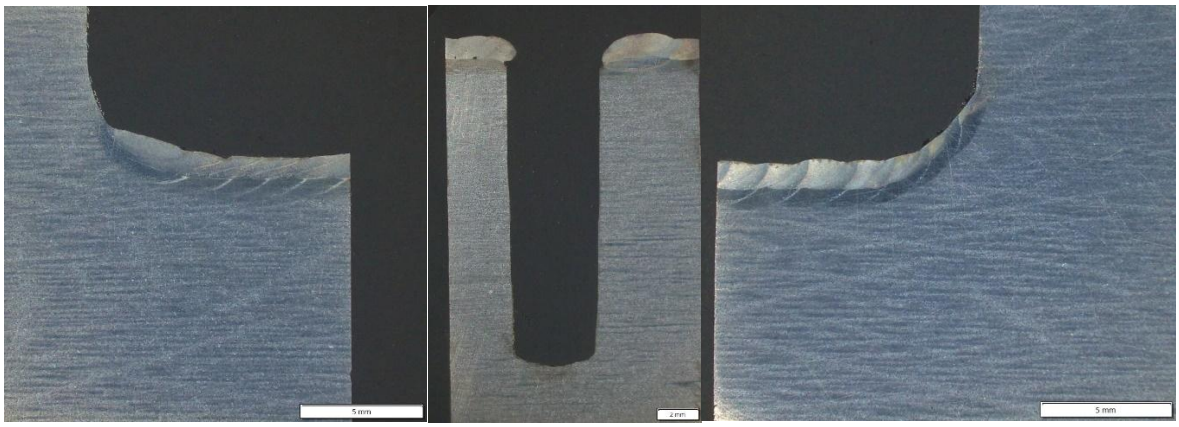


*Figure 78: Sequence 1 macrographs (A2, C2 and A1 from left to right).*

### Sequence 2

The sequence 2 show lack of fusion between tracks, this can be produced by low input energy that is not able to fuse the material around.

In addition to this, the sequence of clad the whole surface and then clad the holes present some discontinuities in the cladded material. Indicating that is not the best option to follow.

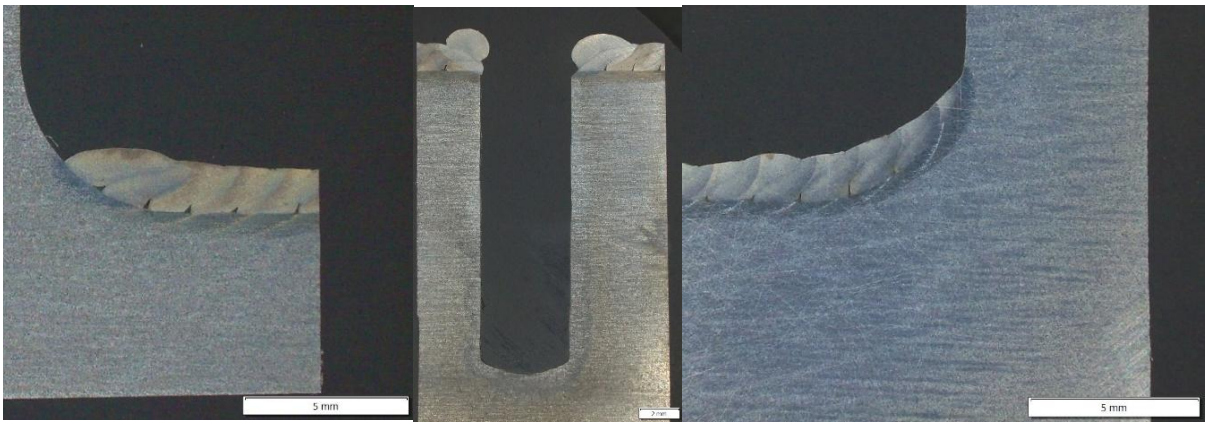



*Figure 79: Sequence 2 macrographs (A4, C5 and A3 from left to right).*

After the macroscopic analysis, a set of indentations were made to evaluate the hardness in different areas.

*Table 24. Hardness measurements.*

| Hardness Area (HV) | Sequence 1 | Sequence 2 |
|---|---|---|
| **Bead** | 643 | 744 |
| **HAZ** | 502 | 412 |
| **Base material** | 218 | 226 |

The results indicate a decrease in the hardness for the condition with a higher stepover, by contrast this sequence present some defects (lack of fusion) between the beads.

# 4 Conclusions

## 4.1 Relevance to Made in Europe

The below tables summarize the contributions towards the Made in Europe strategy[2] stemming from the work reported in this deliverable.

*Table 25: Contributions towards specific objectives of Made in Europe.*

| Objectives | Our contribution |
|---|---|
| Specific Objective 1: Efficient, responsive and smart factories and supply chains | |
| • R&I Objective 1.2: Scalable, reconfigurable and flexible first-time right manufacturing | The digital protocol developed within the framework of the project allow repair any kind of crankshaft independent of the size and features with high quality. |
| • R&I Objective 1.5: Advanced manufacturing processes for smart and complex products | The digital protocol allows automate the remanufacturing of a crankshaft. |
| Specific Objective 2: Circular products & Climate-neutral manufacturing | |
| • R&I Objective 2.2: De-manufacturing, re-manufacturing and recycling technologies for circular economy | The digital protocol allows remanufacturing instead to manufacture new ones with new raw material. |
| • R&I Objective 2.3: Manufacturing with new and substitute materials | Our proposal changes the standard material Cobalt based by another less contaminant based in a Ferrous alloy. |

*Table 26: Contributions towards key technologies and enablers of Made in Europe.*

| Key technologies and enablers | Our contribution |
|---|---|
| Advanced smart material and product processing technologies, and process chains (additive manufacturing, joining, shaping, structuring, surface tailoring, etc.) | Our contribution lies in a surface process treatment, enabling better performance and extend the life cycle. |
| Smart mechatronic systems, devices and components | Our contribution is aligned with this, as new sensors have been enabled and integrated into a robotic system, allowing for a high-tech solution on low-cost device and facilitating wide adoption by industry. |

[2] See https://effra.eu/wp-content/uploads/2023/12/made_in_europe-sria.pdf.

## 4.2 Concluding Remarks

This deliverable presents a comprehensive methodology for generating robust robot path planning strategies for the remanufacturing of large-scale crankshafts. The key contributions of this deliverable include:

- **Operational impact despite calibration requirements**. Although the workflow requires hand-eye (robot-camera) calibration expertise, automatically generating a robot-referenced CAD/mesh significantly reduces manual programming and shop-floor hours in crankshaft repairs.
- **Global, frame-to-model fusion is preferable**. Registering each view against the accumulated global model (frame-to-model) yields more stable, drift-free reconstructions than pairwise alignment. At the cost of longer runtimes and a larger memory footprint.
- **Direct handover with protected functional features**. Providing a robot-referenced STL allows the deposition planner to enforce forbidden zones around lubrication holes, reducing blockage risk and simplifying integration.
- **Physical trials are essential to close the digital–physical gap**. The mock-up trials highlighted the importance of validating digitally generated robot programs under real industrial conditions, revealing effects related to signal timing, calibration tolerances, and accumulated geometric deviations that are not fully captured in simulation. These observations informed refinements in software logic and parameter handling, reinforcing the need for iterative physical validation.
- **Continuous deposition strategies are expected to improve process stability**. The under-deposition observed with discontinuous circular toolpaths motivated the development of continuous spiral deposition strategies, which are theoretically expected to improve material continuity and thermal stability. Experimental validation of these spiral paths is planned in upcoming trials to confirm their impact under real process conditions.
- **The Design of Experiments was successfully executed, enabling a comprehensive mapping of the relationship between process parameters and response variables**. The statistical analysis not only validated the primary influences on cladding quality but also identified specific anomalies in initial hypothesis, providing a more nuanced understanding of the laser-material interaction for large-scale components.
- Thermomechanical simulations evaluating various **deposition strategies revealed that different scanning strategies do not have a significant impact on residual stresses or final deformations**. This is primarily attributed to the massive geometry of the crankshaft, which acts as a highly efficient heat sink, stabilizing the thermal gradients regardless of the robot´s path.

- **The integration of thermal analysis with experimental data derived from the DOE serves as a robust framework for the qualitative prediction of microstructure and the integrity of the HAZ.** These findings open a new via for materials properties prediction without phase simulation models.
- **The research confirmed the feasibility of substituting traditional Cobalt-base filler materials with more sustainable Iron-based alternatives**. The transition to a material with lower environmental footprint was achieved without compromising the structural requirements of the application, aligning the repair process with European "Green Deal" manufacturing objectives.

# 5 References

Alexa, M. B.-O. (2003). Computing and rendering point set surfaces. *IEEE Transactions on Visualization and Computer Graphics*, 9(1), 3–15.

Bernardini, F. a. (1999). The Ball-Pivoting Algorithm for Surface Reconstruction. *IEEE Transactions on Visualization and Computer Graphics*, 349-359.

Besl, P. J. (1992). Method for registration of 3-D shapes. . *Sensor fusion IV: control paradigms and data structures* , Vol. 1611, pp. 586-606).

Carr, J. C. (2001). Reconstruction and representation of 3D objects with radial basis functions. *Proceedings of the 28th annual conference on Computer graphics and interactive techniques*, 67-76.

*Handyscan*. (2025, 12 17). Retrieved from Creaform: https://www.creaform3d.com/es/products/portable-3d-scanners/portable-3d-scanner-handyscan-3d

Kazhdan, M. B. (2006). Poisson surface reconstruction. . *Proceedings of the fourth Eurographics symposium on Geometry processing*, Vol. 7, No. 4.

Newcombe, R. A. (2011). KinectFusion: Real-Time Dense Surface . *10th IEEE International Symposium on Mixed and Augmented*, 127-136.

Park, F. C. (1994). Robot sensor calibration: solving AX= XB on the Euclidean group. *IEEE Transactions on Robotics and Automation*, 10(5), 717-721.

*Photoneo*. (2025, 16 12). Retrieved from Photoneo: https://www.photoneo.com/motioncam-3d/

*Robodk*. (2025, 12 17). Retrieved from Robodk: https://robodk.com/

Taubin, G. (1995). A signal processing approach to fair surface design. 351-358.

Zoltan Csaba Marton, R. B. (2009). On Fast Surface Reconstruction Methods for Large and Noisy Datasets. *Proceedings of the IEEE International Conference on Robotics and Automation (ICRA)*.

Nosonovsky, M., Kailas, S. V, & Editors, M. R. L. (2013). Tribology for Scientists and Engineers. In Tribology for Scientists and Engineers. https://doi.org/10.1007/978-1-4614-1945-7

Zhang, G., Tang, J., Yang, K., Wang, R., Chen, Y., Xiong, Y., Wu, C., Li, Z., Wang, Y., & Lin, H. (2024). Important contributions of metal interfaces on their tribological performances: From influencing factors to wear mechanisms. Composite Structures, 337(March). https://doi.org/10.1016/j.compstruct.2024.118027